UNIVERSITÀ DI PARMA

DEPARTMENT OF CHEMISTRY, LIFE SCIENCES AND ENVIRONMENTAL SUSTAINABILITY

Doctoral Programme in Chemical Sciences
XXIX Cycle

DYES AND NANOPARTICLES FOR 2PA APPLICATIONS: MODELS AND COMPUTATIONS

PhD Student:
Somananda Sanyal

Supervisors:
Prof. Anna Painelli
Prof. Swapan K. Pati

Coordinator:
Prof. Roberto Corradini

2014-2017

Dedicated to

My Family

List of Abbreviations

BFC	BF_2 complex of Curcumin
CT	Charge Transfer
CNT	Carbon Nanotubes
D/A	Electron Donor / Acceptor
DANS	p,$p^{'}$-dimethylamino-nitrostilbene
DFT	Density Functional Theory
DMRG	Density Matrix Renormalization Group Theory
eV	electron-volt unit
ESM	Essential State Model
ESP	Electrostatic Potential
FMO	Frontier Molecular Orbital
GM	Göppert-Mayer units (1GM $\equiv 10^{-50}$ cm ^{4} s photon^{-1})
HOMO	Highest Occupied Molecular Orbital
HRS	Hyper Rayleigh Scattering
LUMO	Lowest Unoccupied Molecular Orbital
MO	Molecular Orbital
OPA	One Photon Absorption
PCM	Polarizable Continuum Model
PPP	Pariser-Parr-Pople
TPA	Two Photon Absorption
ZINDO	Zerner's Intermediate Neglect of Differential Overlap

Acknowledgements

It's time to say Thank You to many people who have either actively or silently been supporting me in successfully completing the PhD thesis! These three years of my PhD tenure in Parma, Italy has been an eye opener for me, as I slowly learnt to adapt as a girl in a new city. I have been extremely fortunate to meet some people whose influence has been profound and worth cherishing, and I want to grab this opportunity to Thank them All!

My parents have been my biggest support system throughout my life and from them I have learnt the first lessons of morality and humanity. Their "never-to-give-up" spirit has inspired me not to lose hope in any situation. I owe my learnings to them, my first and best teachers... thank you *Maa* and *Baba*!

I want to acknowledge the guidance of my PhD supervisor Prof. Anna Painelli, with whom the scientific discussions have been really encouraging and helping me to develop research ideas and learn new things. I also want to thank Prof. Francesca Terenziani, with whom discussions were always enriching. I thank Dr. Cristina Sissa for her guidance and cooperation in all the works during my PhD tenure. My regards to Prof. Alberto Girlando and Dr. Matteo Masino.

I have been really fortunate enough to get the opportunity to work with Prof. Swapan K. Pati, my co-supervisor in PhD, whose continuous encouragements, support, guidance and his love for science always filled me with the zeal to work better. Words fall short for *Anusooya Ma'am* and Sohan, whose love and affection, since my Bangalore days, and work supports made me cope up with many situation and

a happier person. Thank You!!!

I want to thank Dr. Arun Manna who taught me how to deal with different exciting research projects and various basic things to be taken into account when dealing with a scientific study. His constant encouragement and vision to look at things from various perspectives always inpired me. I specially want to thank Dr. Prakash Parida, Dr. Pralok K. Samanta, Dr. Dibyajyoti Ghosh, Dr. Bradraj Pandey, Dr. Chaitanya Sharma, Dr. Swastika Banerjee, Arkamita from JNCASR Bangalore for making the lab life always an enriching experience. A big thank you to all my friends and lab mates in JNCASR.

Staying abroad and adapting oneself to a city new and culture is always an experience and some people make the experience better and cherishable. I cannot thank enough my friends Domna and Siarhei for always being a support and a family away from home. We spent some lovely and cherishable days together. I wholeheartedly thank Francesco for being the beautiful person he is and helping me with any situation I faced and worried. I thank Dr. Francesca Delchiaro, Nicola and Brunella for being such good lab mates!

Being a part of *Nano2Fun* network meant a lot more scope for scientific discussions and exchange of opinions, in the various project meetings with the researchers part of this network. These were of immense help in developing my skills in scientific presentations. I want to thank this initiative and all members of this network for being so active in discussions and sharing their knowledge with us.

Talking about adjusting in a new city, I need to thank Mr. Miltos Zannas for helping me in more ways than one throughout.

I want to thank my friends back home in India and my school science teachers for instilling in me the first love for Chemistry and Maths, my Sirs Dr. Shekhar Pal and Mr. Sanjay Banerjee. I want to thank Prof. Ayan Datta for giving the first opportunity to a student of organic chemistry to try her hand in Computational Chemistry and making me love the field of work. He has been a constant source of inspiration and support all these years, thank you Sir!

My deepest thanks to *Arpan* whose unending belief in me and continuous encouragement while dealing with a PhD life always seem to work wonders for me.

Thanks to Dott.ssa Paola Rossi for the administrative works in UNIPR and to Nano2Fun Marie Curie ITN project for giving me the opportunity as a PhD

student. The research leading to the the results presented in this thesis has received funding from the People Programme (Marie Curie Actions) of the European Unions Seventh Framework Programme FP7/20072013 under REA grant agreement no. 607721 (Nano2Fun). I want to thank CCMS JNCASR Bangalore and CINECA for the HPC IsC35_MMMOptic and IscrC_MMM-CT projects for the computational facilities.

List of Figures

List of Tables

Contents

Preface

Study of molecular functional materials is an active field of research, investigating for several applications as lightweight and environment-friendly materials with highly customizable properties. Of particular interest for the works presented in this thesis are materials for non-linear optical applications, and more specifically for two-photon absorption. These works have been performed in the framework of a collaborative project *Nanochemistry of molecular materials for 2-photon functional application (Nano2Fun)*, funded by the EU Commission. The main aim of Nano2Fun is to develop optimized materials and methods for specific applications of two-photon absorption towards bioimaging and nanofabrication. Within this framework, the contribution of this thesis is to help the experimentalists rationalize linear and non-linear spectral properties of organic dyes and of their aggregates, offering a sound theoretical analysis.

Dyes for NLO applications have been investigated for a very long time and fairly reliable structure-property relationships are available for several families of dyes. However, the dyes of interest for NLO applications are structurally characterized by large polarizability and hyperpolarizabilities, making them extremely sensitive to perturbations from the environment. Understanding the behaviour of molecular materials therefore becomes challenging and calls for the development of reliable relationships that relate the supramolecular structure of the molecular material and its NLO properties.

Dye aggregates are the most ambitious target of this work, as systems that

have been the subject of intensive theoretical and experimental research in the past decades. The most appealing specialities of dye aggregates are their emerging new functionalities, *i.e.* functionalities that are not obvious in the individual molecule but makes a prominent mark upon aggregation due to *intermolecular electrostatic interactions*. Understanding of the structural and functional properties of dye aggregates, and thereby their important applications in the areas of photonics, molecular engineering and biomedical studies became popular after the serendipitous discovery of J-aggregates of cyanine dyes in the beginning of 1930s.

Systems formed by π linkage between electron donor (D) and acceptor (A) functional groups make up the basic backbone of dyes for innovative applications. In this regard, dipolar (D-π-A) molecules, and further elongations with either donor or acceptor groups forming quadrupolar (D-π-A-π-D), and octupolar dyes have prominent applications as non-linear optical materials. In this thesis, we have studied a few of these dipolar and quadrupolar dyes (or chromophores) to understand and rationalize their linear and non-linear spectroscopic behaviour, their aggregates and organic nanoparticles. To achieve this aim we have combined parametric Hamiltonians (Essential State Models, ESM), with first principle calculations, mainly Density Functional Theory (DFT) and Time-Dependent DFT (TDDFT), and Density Matrix Renormalization Group (DMRG) theory.

Chapter 1 is an introductory chapter were we discuss the different types of chromophores, their properties and applications, and present the fundamentals of linear and non-linear optical spectroscopy. Then we introduce models and methods we have exploited in our works, discussing in detail the ESMs for dipolar and quadrupolar dyes (Two State and Three State Models, respectively) and give a flavour of Density Functional Theory and Density Matrix Renormalization Group theory, explaining the working strategy.

Chapter 2 presents an extensive study of aggregates of quadrupolar dyes. We have combined the DFT and TDDFT calculations to validate ESMs on dimers of curcumin-based dyes. Considering the fact that DFT calculations suffer from the limitation of handling a large number atom system, and having validated the ESM for quadrupolar dyes against a theoretical approach having a wider acceptance in the scientific community, we have studied bigger aggregates of curcumin dyes, to approach the limit of organic nanoparticles, thereby successfully explaining

the experimental results. The most interesting results are obtained however for the aggregates of squaraine dyes, a family of molecules with large TPA responses and a highly polarizable structure. Several puzzling experimental results for squaraine aggregates, that include large aggregation effects on 2PA spectra and the observation of *non-fluorescent J-aggregates* are quantitatively understood within our approach towards aggregates that exploits essential state models, and are rationalized in terms of the large and non-linear response of the squaraine molecules to intermolecular electrostatic interactions.

In **Chapter 3**, taking inspiration from a paper recently published work on the Hyper-Rayleigh Scattering of dipolar chromophores encapsulated inside carbon nanotubes, we propose a model to rationalize and quantitatively estimate the cooperative effect dominating hyperpolarizabilities. We made use of DFT for finding the optimized geometries and the particular electric field strength required to transform the molecule from a neutral to zwitterionic state. This has been further used for calculation of intermolecular interactions in the neutral and zwitterionic state. Using this information as input for ESM, we reached the impressive result of a superlinear amplification of the first hypopolarizability of the dimension of the linear aggregate. This result is used to reinterpret experimental data and sheds light on the importance of developing specific models for aggregates of polarizable dyes, where the approximations of the exciton model are bound to fail.

Chapter 4, written in tight collaboration with experimentalists, deals with a biphenyl based CT dye. An extensive analysis of linear and pump and probe spectra of the dye in different solvents lead to quite puzzling results that were rationalized based on semi-empirical ZINDO calculations running up to high energy excited states, in order to identify families of charge transfer and local-excited states that are disjoined as for their spectral properties.

In **Chapter 5** we have focused on squaraine dyes. For this family of dyes, failure of TDDFT has been extensively discussed in the literature, mainly due to the biradicaloid nature of the squaraine ground states. To analyze this problem we exploited finite size symmetrized DMRG calculations to solve the corresponding Pariser-Parr-Pople Hamiltonian. Preliminary results fully support the biradicaloid character of the squaraine ground state and will be extended to model linear and non-linear optical spectra of the very interesting family of squaraine dyes.

Chapter 1

Chromophores and Spectroscopy

1.1 Introduction

A chromophore usually defines a group of atoms or possibly a whole molecule, which is responsible for imparting colour. In this thesis, we will use the word chromophore frequently, referring to a molecule, often also called a dye. Organic dyes are characterized by an extended delocalized π-electron system possibly connecting electron donor (D) and/or acceptor (A) group. In these systems, electronic excitation are at low energy ranging from the visible to the near-infrared region [1]. Organic chromophores not only are interesting for basic applications as dyes for e.g. textiles and food, but also they find important usage as fluorescent markers in biomedicine [2], they are used as active media in CD-ROMs [3], etc. In recent years, much effort has been put on studying organic dyes for non-linear optical (NLO) applications exploiting the large non-linearity of the response of π-conjugated systems to applied electric fields. Dyes for NLO can be used for second-harmonic generation, all-optical switching, two-photon absorption (TPA) applications in bioimaging [4, 5], nanofabrication [6–8] or photodynamic therapy [9–11], to name just a few examples. In this chapter we will briefly describe linear and non-linear optical properties of molecular materials, then we will address the theoretical models and

methods to study different dyes, which will be exploited in next chapters. Two families of dyes will be addressed in this thesis, dipolar D-π-A dyes and quadrupolar D-π-A-π-D or A-π-D-π-A.

We have shown some typical NLO molecules in Fig. 1.1.

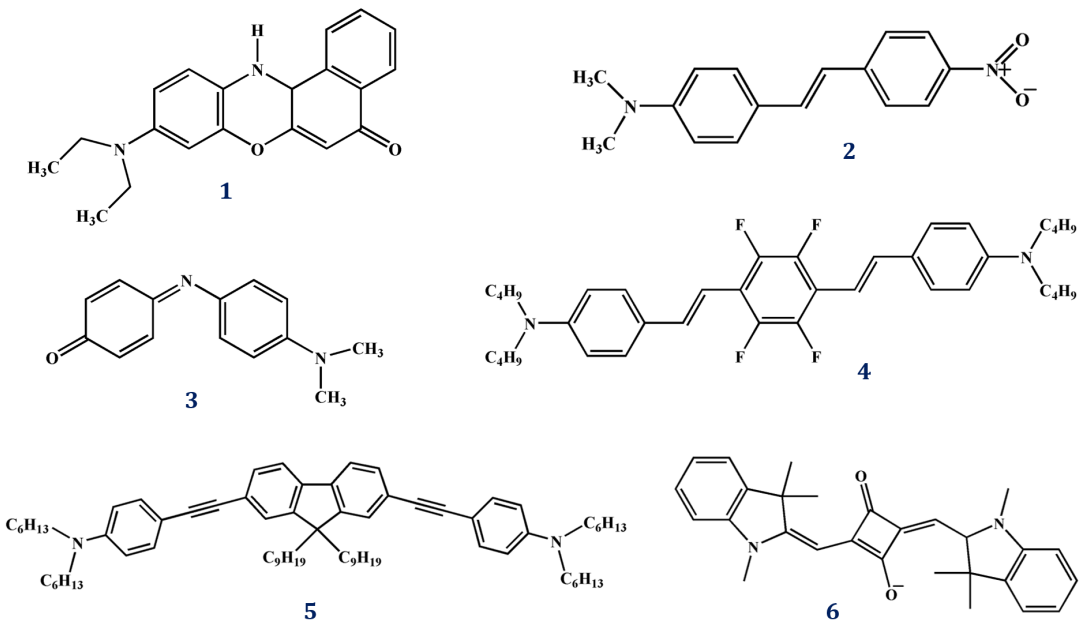

Figure 1.1: Chemical structures of NLO chromophores: (1) Nile Red, (2) p,p-dimethylaminonitro-stilbene (DANS), (3) Phenol Blue, (4) Distyrylbenzene derivative [12], (5) Fluorene derivative [13], and (6) Squaraine derivative [13]. Molecules 1-3 are dipolar chromophores and molecules 4-6 are quadrupolar chromophores.

Dipolar dyes are extensively studied as solvation probes, exploiting the large solvatochromism, characteristic of these molecules, to extract information on the complex phenomenon of solvation using simple spectrometric data. Highly fluorescent dipolar dyes are used as laser dyes and recently they are also used as active molecules in tunable organic light-emitting diodes [14–16]. These molecules are also the molecules of choice for second-order non-linear optics (NLO) [17–20] and the first class of rectifiers belong to this group [21, 22]. Over the last 50 years, several donor and acceptor chromophores have been examined in the context of their propensity to form charge transfer (CT) complexes and intramolecular CT taking place between the electron-rich D moiety and the electron-poor A moiety,

linked with the π-bridge, has paved the way to investigate the electron-transfer process, in supramolecular networks and aqueous solutions *etc.* [23–25] In dipolar chromophores consisting of heteroaromatic rings (which are either electron-rich or poor, like pyrrole, furan, pyridine *etc.*), even partial charge delocalization converts the aromatic nature of the whole system into quinonoid one, with some loss in aromatization energy. This loss is much higher for benzenoid systems than heteroaromatics, which are known for possessing aromatic stabilization energy lower than benzenoids. Thus, heteroaromatic dipolar dyes will have considerably lower energy cost of charge delocalization, making the delocalized structures more favoured. Hence, these zwitterions with heteroaromatic groups as charge bearing units show considerable promise in the field of linear and nonlinear optics.

Besides, the tunable polarization of the π-scaffolds by donor and acceptor end groups proved to be important for providing suitable electronic structures for second or third harmonic generation NLO [9, 26], as well as for the effective designing of photorefractive materials, for example, heterocyclic thiazolidenemalononitrile acceptor unit, combined with the proper electron donor unit and effective conjugation length [27, 28]. Thus, obtaining electro-optic organic materials with high second-order susceptibility, $\chi^{(2)}$, is an on-going dynamic area of research [29–32].

Quadrupolar dyes or dyes having D-A-D or A-D-A structure, have been introduced as particularly interesting for TPA applications [33–36]. Indeed the TPA cross section increases, as a rule of thumb, by an order of magnitude when going from dipolar to quadrupolar dyes. Dyes with large TPA cross sections are in demand for two-photon excited fluorescence (TPEF) microscopy [37–42], two-photon induced biological caging studies [43], optical data storage [44–46], optical limiting [47, 48] *etc.* Quadrupolar dyes were designed specifically as two-photon absorber systems [36, 49–52] and lots of work has already been done in this field. Since these molecules are symmetric in nature, they have no permanent dipole and the vertically excited states are non-dipolar in nature [13]. Experimental data, for many of these systems, suggest the presence of polar excited states showing strong fluorescence solvatochromism [12, 53–56]. The quadrupolar chromophore family is made up of some of the most exciting chromophores like squaraines [13, 57–61], the distyrylbenzene family [12, 62, 63], curcuminoid dyes [64, 65], triphenylamine based dyes [66], *etc.*

Due to their large (hyper)polarizability, organic dyes for NLO applications are extremely sensitive to perturbation from the environment. As for solvated dyes, a quite impressive solvatochromism of polar and of some quadrupolar dyes are well known and fairly well understood [13, 60, 67, 68]. More subtle is the role of intermolecular interactions in aggregates, crystals, films or nanoparticles made of dyes. The exciton model is the reference picture to deal for intermolecular interactions in these materials [69, 70], but, as it stands, it only applies to linear spectral properties. The worse part is that the exciton model completely neglects the molecular polarizabity and as such it does not apply to aggregates of dyes for NLO applications [71, 72]. Since important effects from intermolecular interactions are expected in NLO properties of aggregates, a deeper understanding of the relationship between the supramolecular structure in aggregates and the NLO responses is important. This also acts as a guide for the synthesis of optimized materials for specific applications. Validating models for molecular aggregates, as applied to NLO properties, is one of the main goals of this work.

1.2 Linear and Non-Linear Optical Spectroscopy

When light interacts with matter, several phenomena may occur depending on the light intensity and, of course, on the nature of the investigated sample. For weak light intensity, matter responds linearly to the applied electric field and three phenomena can be observed: (a) the absorption of a photon, (b) the emission of a photon, and (c) the photon dispersion. The first two phenomena are active processes, where energy is exchanged between light and matter, while the third phenomenon, that describes the deflection of a light beam inside a material, is a passive process, where light and matter do not exchange energy [73].

With the advent of laser sources, the interaction of matter with intense light fields [74] became a very active field of research, both in terms of spectroscopic studies as well as for innovative applications. It is useful to classify the phenomena to different order in the applied field [75, 76]. As stated above, at the linear order, only absorption of a single photon and the photon dispersion are possible (emission of a photon is also possible, provided one starts from an excited, non-equilibrium state). At the second order only passive processes are allowed, i.e. processes where

there is no exchange of energy between matter and the electromagnetic field. The possible processes are therefore sum frequency generation, where two photons are combined in the material to generate a new photon whose frequency is the sum (or the difference) of the frequency of the two incoming photons. Particularly interesting for our work is the "special case" when the two incoming photons are equal, so that one observes a frequency-doubling effect, also called second harmonic generation (SHG). Quite interestingly, second-order phenomena (as all even-order phenomena) are only allowed in asymmetric material media, or more precisely in media without an inversion center.

The third order processes [75, 76] include a variety of phenomena encompassing both active and passive processes. Among passive processes, four-wave mixing phenomena can be mentioned, where three incoming photons mix to give rise to a fourth photon. Of course, in the case of three equivalent photons as input, the process reduces to third harmonic generation (THG). Among active processes, we can enlist inelastic scattering (Raman) and, of particular relevance for our work, the TPA, that describes the simultaneous absorption of two photons by the material.

1.2.1 Linear Processes: Absorption and Fluorescence

Linear absorption implies an exponential decrease of the light intensity inside the material, and is usually measured in terms of the absorbance [77]:

$$A = -\log \frac{I}{I_0} = \epsilon d C \tag{1.1}$$

where I_0 is the light intensity before crossing the sample, I is the light intensity after an optical path d inside a sample is traversed, with a dye concentration C. Finally ϵ is the molar extinction coefficient.

The extinction coefficient (ϵ in M^{-1} cm^{-1}) can be calculated as the imaginary part of the linear response, according to:

$$\epsilon(\tilde{\nu}) = \frac{10\pi N_A \tilde{\nu}}{3ln10\hbar c\epsilon_0} \frac{1}{\sqrt{2\pi}\sigma} \sum_n \mu_{gn}^2 exp\left[-\frac{1}{2}\left(\frac{\tilde{\nu}_{gn} - \tilde{\nu}}{\sigma}\right)\right] \tag{1.2}$$

The emission intensity (in arbitrary units) is calculated from the fluorescent

state as:

$$I(\tilde{\nu}) \propto \tilde{\nu}^3 \frac{1}{\sqrt{2\pi}\sigma} \sum_n \mu_{fn}^2 exp\left[-\frac{1}{2}\left(\frac{\tilde{\nu}_{fn} - \tilde{\nu}}{\sigma}\right)\right] \tag{1.3}$$

In Eqn. 1.2, N_A denotes the Avogadro constant, c is the speed of light, ϵ_0 stands for vacuum permittivity, $\tilde{\nu}_{gn}$ and μ_{gn} are the transition wavenumber and dipole moment for $g \rightarrow n$ transition, respectively, from ground state (g) to generic excited state (n), while the summation runs over all vibronic excited states. In case of fluorescence, Eqn. 1.3 combines the terms $\tilde{\nu}_{fn}$ and μ_{gn} for the transition wavenumber and dipole moment (for $f \rightarrow n$ transition) where f is the fluorescent state. The summation here runs over all states having lower energy with respect to f state.

1.2.2 Measuring Second Order NLO responses in solution and Hyper Rayleigh Scattering

As stated above, second order NLO responses, usually referred to as β-responses, are only observable in non-centrosymmetric media, so that, irrespective of the dye symmetry, direct measurements of β are impossible in solution. However it is possible to get information about the β response of non-centrosymmetric dyes in solution, exploiting the Hyper Rayleigh scattering (HRS) technique that measures the incoherent second-harmonic light scattering in solution, as related to fluctuations locally breaking the symmetry of the system [78, 79]. In HRS measurement a focused laser beam is shone on a solution and the intensity of the second-harmonic generated frequency is recorded as a function of the frequency of the incoming light. The calibrated HRS signal S^{HRS}, per dye molecule, is obtained with reference to the response of the pure solvent as [80]:

$$S^{HRS} = \frac{N_{solvent}}{N_{molecule}} \left(\frac{S^{HRS}_{composite} - S^{HRS}_{solvent}}{S^{HRS}_{solvent}}\right) \beta^2_{solvent} \tag{1.4}$$

Here, N is the number density, $S^{HRS}_{composite}$ is the calibrated β-response of the solute-solvent-associated system.

The calibrated S signal is an intensive quantity (much as the molar extinction

coefficient defined above), that is related to the β tensor, or better to the orientational average of its square. Since we will only discuss β responses for linear molecules, where a single component of the β tensor survives, we only give the explicit expression relating S^{HRS} to β for this specific case, as follows [81]:

$$S^{HRS} = |\beta_{xxx}^2| \tag{1.5}$$

where,

$$\begin{aligned}\beta_{xxx}(-2\omega;\omega,\omega) = \frac{1}{3\hbar^2}\sum_{m,n}\Bigg[&\frac{\langle g|\mu_x|m\rangle\langle m|\bar{\mu}_x|n\rangle\langle n|\mu_x|g\rangle}{(\Omega_{mg}-2\omega)(\Omega_{ng}-\omega)} + \\ &\frac{\langle g|\mu_x|m\rangle\langle m|\bar{\mu}_x|n\rangle\langle n|\mu_x|g\rangle}{(\Omega_{mg}^*+\omega)(\Omega_{ng}-\omega)} + \\ &\frac{\langle g|\mu_x|m\rangle\langle m|\bar{\mu}_x|n\rangle\langle n|\mu_x|g\rangle}{(\Omega_{mg}^*+\omega)(\Omega_{ng}^*+2\omega)}\Bigg]\end{aligned} \tag{1.6}$$

In Eqn. 1.6, ω denotes the laser frequency and $\Omega_{mg} = \omega_{mg} - i\gamma_{mg}$, where ω_{mg} denotes the excitation energy of state m and g is the ground state. γ_{mg} stands for the inverse lifetime of each state. The m and n indices run over all the excited states, such that the summation includes not only non-degenerate ($m \neq n$), but also degenerate ($m = n$) level terms. The relative weight of the individual terms is ascertained by the transition dipole moments (μ_x is the dipole moment operator along molecular x axis) between the different levels. Also, $\langle m|\bar{\mu}|n\rangle = \langle m|\mu|n\rangle - \langle g|\mu|g\rangle\delta_{mn}$.

1.2.3 Third Order NLO Response - Two Photon Absorption

The theory of simultaneous absorption of two photons by the same molecule was first studied by Nobel Laureate Maria Göppert-Mayer in her PhD thesis in the 1930s [82, 83]. The unit of TPA, GM, is named after her. In 1961, after about 30 years, the experimental evidence could be achieved after the advent of laser [84]. TPA studies became much easier in the '90s as the availability of sub-picosecond laser came widely, particularly the Ti:sapphire laser. Subsequently, the invention of two-photon fluorescence microscopy by Denk *et al.* and its rapid acceptance by confocal microscope manufacturers, led to a splurge in the researches in the field of

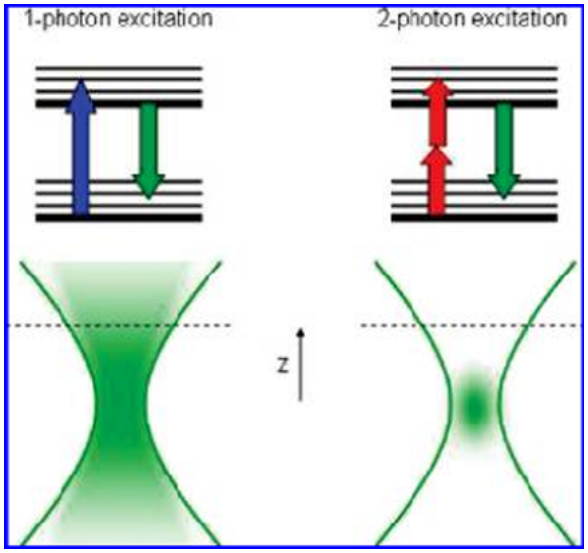

Figure 1.2: OPA (blue) and TPA (red) transitions between molecular energy levels. Appreciably excited regions are shown in green. TPA-related processes are more localized in space, into a volume called voxel, where the intensity is highest. Reprinted with permission from Ref. [87]. Copyright (2009) American Chemical Society.

multiphoton spectroscopy [11, 37, 38, 85, 86].

TPA involves simultaneous interaction of the molecule with two-photons, hence the probability of TPA increases with the square of the light intensity (I^2). This accounts for the fact that TPA process is observed only in intense light beams (focussed pulsed lasers) which produces very high instantaneous photon density, offering intrinsic 3D resolution to TPA-initiated processes with enormous implications in the field of microscopy [37–40], two-photon induced biological caging studies [43], optical data storage [44–46], optical limiting [47, 48] *etc.*

In a sample where light is only absorbed by two photons, the decrease of the light intensity I inside the medium is proportional to the square of the intensity as:

$$\partial I/\partial z = -N\sigma I^2/\hbar\omega \tag{1.7}$$

In Eqn. 1.7, z is the optical path inside the medium, N is the number of molecules per unit volume and ω is the frequency of the light. σ denotes the TPA cross section, usually reported in GM units (1GM $\equiv 10^{-50}$ cm^4 s photon^{-1} molecule^{-1}).

The TPA cross-section is obtained from the imaginary part of the third order

non-linear response γ, accounting for solution samples of orientational averages, as follows:

$$\sigma_2(\omega) = 10^{58}\frac{\hbar\omega^2}{4\epsilon_0^2 c^2} Im\langle\gamma_{ijkl}(-\omega;\omega,\omega,-\omega)\rangle_{IJKL} \tag{1.8}$$

where c is the speed of light, $\langle\gamma\rangle$ the orientationally averaged second hyperpolarizability, $IJKL$ run over the laboratory axis, while $ijkl$ run on the molecular reference frame axis.

Tensor elements $\gamma_{ijkl}(-\omega;\omega,\omega,-\omega)$ are given by the following sum-over-states (SOS) expressions [88, 89]:

$$\begin{aligned}\gamma_{ijkl}(-\omega;\omega,\omega,-\omega) = \frac{1}{\hbar^3}\sum_{lmn}\Bigg(&\frac{\langle g|\mu_i|l\rangle\langle l|\bar{\mu}_j|m\rangle\langle m|\bar{\mu}_k|n\rangle\langle n|\mu_l|g\rangle}{(\Omega_{lg}-\omega)(\Omega_{mg}-2\omega)(\Omega_{ng}-\omega)} + \\ &\frac{\langle g|\mu_j|l\rangle\langle l|\bar{\mu}_i|m\rangle\langle m|\bar{\mu}_k|n\rangle\langle n|\mu_l|g\rangle}{(\Omega^*_{lg}-\omega)(\Omega_{mg}-2\omega)(\Omega_{ng}-\omega)} + \\ &\frac{\langle g|\mu_i|l\rangle\langle l|\bar{\mu}_j|m\rangle\langle m|\bar{\mu}_l|n\rangle\langle n|\mu_k|g\rangle}{(\Omega_{lg}-\omega)(\Omega_{mg}-2\omega)(\Omega_{ng}-\omega)} + \\ &\frac{\langle g|\mu_j|l\rangle\langle l|\bar{\mu}_i|m\rangle\langle m|\bar{\mu}_l|n\rangle\langle n|\mu_k|g\rangle}{(\Omega^*_{lg}-\omega)(\Omega_{mg}-2\omega)(\Omega_{ng}-\omega)}\Bigg)\end{aligned} \tag{1.9}$$

where only two-photon resonant terms are retained. g is the ground state and summations run over all excited states; $\Omega_{lg} = \omega_{lg} - i\gamma_{lg}$ ($\gamma_{lg} = \gamma$ is set according to the width of the Gaussian bandshape defined above, for all transitions) and all other symbols have the same meaning as in Eqn. 1.6.

1.3 Theoretical Models and Methods

From the above brief description of NLO responses, it is obvious that all properties of interest may be calculated if a detailed knowledge of the system eigenstates and eigenvalues is available. In the following section, we will briefly address the three main theoretical approaches adopted in this thesis to describe NLO properties of dyes in solution and their aggregates.

1.3.1 Essential State Models

Essential State Models (ESMs) are semi-empirical approaches, developed in the host laboratory in the past two decades. The concept is to describe simply but effectively the electronic structure of the dyes, where a limited diabatic basis set is considered, consisting of a few *essential states* defined by the main resonating structures needed to describe the dye. The model also accounts for molecular vibrations, and for the coupling to polar solvation coordinates or, in aggregates, for electrostatic interchromophore interactions.

ESMs offer clear and simplified views of quite complex phenomena, thereby allowing to unravel the fundamental low-energy physics lying underneath. The models make use of a handful of parameters extracted mostly from experimental data. The resonance hybrids of the chromophores are considered as the basis states and thereby the Two-State, Three-State and Four-State models were developed for dipolar, quadrupolar, octupolar and cyanine family of dyes. In this thesis, works have been carried out on dipolar and quadrupolar dyes, hence, we will concentrate on the first two models.

1.3.1.1 Two State Model for Dipolar Chromophores

The ESM for DA dyes shares the main concept, or at least the description of the electronic structure, with well known models, including the Oudar and Chemla model [90] or the Mulliken-Hush model [91]. The electronic structure is described in terms of two orthogonal basis states, namely a neutral $|N\rangle$ or $|DA\rangle$ state and zwitterionic $|Z\rangle$ or $|D^+A^-\rangle$ state, with the gap between the states set to $2z$, and the mixing element as -τ [92, 93] (Fig. 1.3).

The electronic Hamiltonian and the eigenstates are thus written as:

$$\mathcal{H} = 2z\hat{\rho} - \tau\hat{\sigma} = \begin{pmatrix} 0 & -\tau \\ -\tau & 2z \end{pmatrix} \tag{1.10}$$

$$\begin{aligned} |g\rangle &= \sqrt{1-\rho}|DA\rangle + \sqrt{\rho}|D^+A^-\rangle \\ |e\rangle &= \sqrt{\rho}|DA\rangle - \sqrt{1-\rho}|D^+A^-\rangle \end{aligned} \tag{1.11}$$

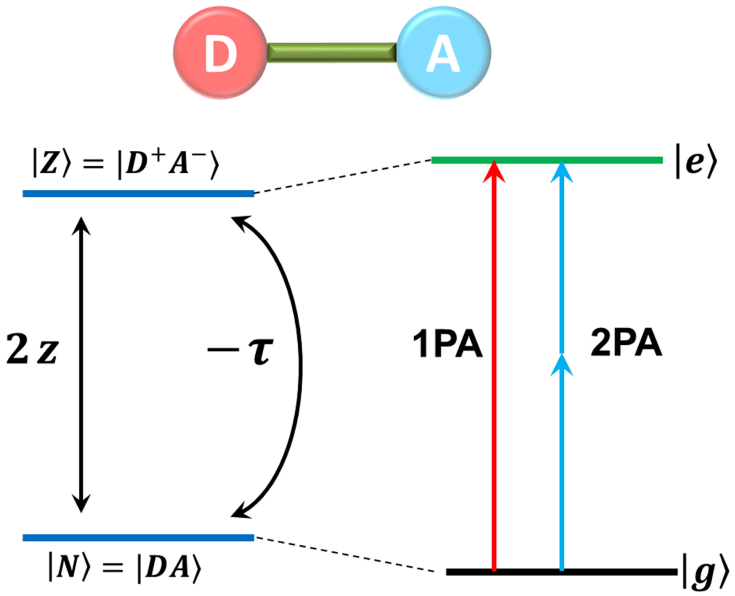

Figure 1.3: Schematic diagram showing the two-state model and energy levels of transition from ground $|g\rangle$ to excited state $|e\rangle$

where the $\hat{\sigma}$ and $\hat{\rho}$ operators are:

$$\hat{\sigma} = \begin{pmatrix} 0 & 1 \\ 1 & 0 \end{pmatrix} \tag{1.12a}$$

$$\hat{\rho} = \begin{pmatrix} 0 & 0 \\ 0 & 1 \end{pmatrix} \tag{1.12b}$$

$\hat{\rho}$ is called ionicity operator and its expectation value in the ground state (ρ) is a measure of the degree of charge transferred from D to A (hence ionicity). It depends only on z/τ ratio as:

$$\rho = \frac{1}{2}\left(1 - \frac{z}{\sqrt{z^2+\tau^2}}\right) \tag{1.13}$$

If $\rho < 0.5$, the molecule is neutral, if $\rho > 0.5$ it is zwitterionic and when $\rho = 0.5$ both the neutral and zwitterionic basis states exhibit degeneracy, called the "Cyanine-limit" [94, 95]. As it has been explained above, following Mulliken model, we neglect all matrix elements of the dipole moment operator except the dipole moment of the zwitterionic state. Accordingly, the dipole moment operator is $\hat{\mu} =$

$\mu_0\hat{\rho}$ (μ_0 being dipole moment of $|D^+A^-\rangle$ state). We can now express the transition dipole moment, transition energy and the dipole moment of the states, important for a CT transition, as:

$$\hbar\omega_{ge} = \frac{\tau}{\sqrt{\rho\,(1-\rho)}} \qquad \mu_{ge} = \mu_0\sqrt{\rho\,(1-\rho)} \tag{1.14}$$

$$\begin{aligned} \mu_g &= \mu_0\rho \\ \mu_e &= \mu_0\,(1-\rho) \end{aligned} \tag{1.15}$$

In Eqn. 1.14, μ_{ge} and $\hbar\omega_{ge}$ are the transition dipole moment and transition energy for transition from $|g\rangle$ to $|e\rangle$ state, and in Eqn. 1.15 μ_g and μ_e are the permanent dipole moments of the two eigenstates, respectively.

The coupling between electronic and vibrational degrees of freedom is quite important to reproduce spectral bandshapes and the model must be extended in this direction. Accordingly, we introduce an effective vibrational coordinate q, that accounts for the different equilibrium geometry associated with the two electronic basis states. The coupled Hamiltonian is written as [93, 96, 97]:

$$\mathcal{H}_{vib} = -\sqrt{2\omega_v}g\hat{q}\hat{\rho} + \frac{1}{2}\left(\omega_v{}^2\hat{q^2} + \hat{p^2}\right) \tag{1.16}$$

Here $g = \sqrt{\omega_v\epsilon_v}$ is the electron-phonon coupling constant, ω_v is the vibrational frequency and ϵ_v is the vibrational relaxation energy corresponding to small polaron binding energy according to Holstein Model. $\hat{q}$ and $\hat{p}$ are the position and momentum operator of the harmonic oscillator.

The coupled electronic and vibrational problem is then solved in a truly non-adiabatic approach. In short, the Hamiltonian matrix is written on the basis obtained as the direct product of the electronic states *times* the eigenstates of the harmonic oscillator described by the last term in Eqn. 1.16, and then diagonalized to get numerically exact non-adiabatic eigenstates. Of course the infinite basis of the harmonic oscillator is truncated to the first M state, with M being large enough to reach convergence. The non-adiabatic eigenstates are then inserted into the expressions for linear and non-linear spectral properties are as described above.

Another important aspect to be taken into account are the effects of solvents on the DA molecules and to account for it reaction-field approach is employed. Polar

solute molecules polarize the surrounding medium and thus feel a reaction field F. The electronic component (F_{el}) of the reaction field, related to the distortion of the electronic charge distribution in the surrounding environment made of solvent molecules, corresponds to a fast motion with respect to the relevant degrees of freedom of the solute. This effect is taken inside the model with a renormalization of model parameters that acquire a dependence on the solvent refractive index [93, 96]. In view of the marginal variability of the refractive index of common organic solvents, we usually assume that model parameters are solvent independent.

On the other hand, the orientational component (F_{or}) of the reaction field accounts for the re-orientation of polar solvent molecules around the DA molecules and the dynamics is slow compared to the electronic or vibrational counterparts. F_{or} is linearly proportional to the dipole moment of the solute as $F_{or} = r_{or}\langle\mu\rangle$, where r_{or} is dependent on both refractive index of the solvent and static dielectric constant, and vanishes for non-polar solvents. Assuming that the solvent behaves as an elastic medium, the Hamiltonian for the polar solvation can be written as [93, 96, 98]:

$$\mathcal{H}_{or} = -F_{or}\hat{\mu} + \frac{\mu_0^2 F_{or}^2}{4\epsilon_{or}} \tag{1.17}$$

Here, polar solvent medium plays the same role as vibrational coordinate which is treated adiabatically because its dynamics is slower than the vibrational one (neglecting the kinetic energy aspect). The solvent relaxation energy $\epsilon_{or} = r_{or}\mu_0^2/2$ has the same meaning as ϵ_{rel} for vibrations and is fixed to reproduce solvatochromism (considering it increases with solvent polarity). A positive solvatochromic behaviour is shown by the DA molecule with a neutral ground state ($\rho < 0.5$) both in absorption and fluorescence. On the opposite, a negative solvatochromism is expected both in absorption and fluorescence for zwitterionic molecules ($\rho > 0.5$).

1.3.1.2 Three State Model for Quadrupolar Chromophores

To model a DAD (or equivalently an ADA) dye three orthogonal electronic basis states are considered, based on the resonating structures of the quadrupolar dye, namely $|DAD\rangle$, $|DA^-D^+\rangle$ and $|D^+A^-D\rangle$. We will consider here only symmetric dyes, extensions of the model to asymmetric DAD' or ADA' dyes having been

discussed in Ref. [60]. For symmetric dyes, $|DA^-D^+\rangle$ and $|D^+A^-D\rangle$ states are degenerate. The energy gap is set between the neutral and these zwitterionic states to $2z$, while $-\sqrt{2}\tau$ is the mixing element between them. $|DA^-D^+\rangle$ and $|D^+A^-D\rangle$ states can be combined in a symmetric (gerade) and an anti-symmetric (ungerade) state as follows [13]:

$$|N\rangle = |DAD\rangle \tag{1.18a}$$

$$|Z_+\rangle = \frac{1}{\sqrt{2}} \left(|D^+A^-D\rangle + |DA^-D^+\rangle\right) \tag{1.18b}$$

$$|Z_-\rangle = \frac{1}{\sqrt{2}} \left(|D^+A^-D\rangle - |DA^-D^+\rangle\right) \tag{1.18c}$$

Further, three operators are defined, $\hat{\rho}$, $\hat{\sigma}$ and $\hat{\delta}$, where $\hat{\rho}$ and $\hat{\delta}$ stands for the charge distribution of the molecule. $\hat{\rho}$ $(=\hat{\rho_1} + \hat{\rho_2})$ is the average charge on the central A moiety, and $\hat{\delta}$ $(=\hat{\rho_1} - \hat{\rho_2})$ stands for the unbalanced charge on the external D moieties (for DAD system). $\hat{\sigma}$ denotes the mixing operator between the gerade states. These three operators are written in matrix notation on the symmetrized basis as:

$$\hat{\rho} = \begin{pmatrix} 0 & 0 & 0 \\ 0 & 1 & 0 \\ 0 & 0 & 1 \end{pmatrix} \tag{1.19a}$$

$$\hat{\sigma} = \begin{pmatrix} 0 & 1 & 0 \\ 1 & 0 & 0 \\ 0 & 0 & 0 \end{pmatrix} \tag{1.19b}$$

$$\hat{\delta} = \begin{pmatrix} 0 & 0 & 0 \\ 0 & 0 & 1 \\ 0 & 1 & 0 \end{pmatrix} \tag{1.19c}$$

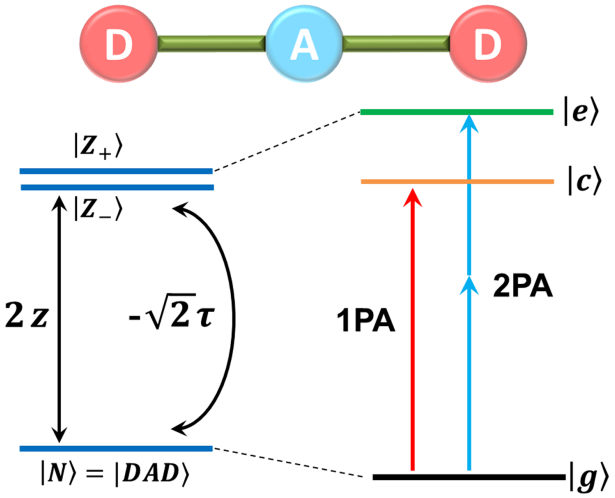

Figure 1.4: Schematic diagram showing the three-state model and energy levels of transition from ground $|g\rangle$ to excited state $|e\rangle$, with the virtual state $|c\rangle$ in between.

Therefore, the electronic Hamiltonian on the symmetrized basis is:

$$\mathcal{H} = 2z\hat{\rho} - \sqrt{2}\tau\hat{\sigma} = \begin{pmatrix} 0 & -\sqrt{2}\tau & 0 \\ -\sqrt{2}\tau & 2z & 0 \\ 0 & 0 & 2z \end{pmatrix} \tag{1.20}$$

Moving along the same lines as the two-state model, the eigen states $|g\rangle$, $|c\rangle$ and $|e\rangle$ are given as:

$$\begin{aligned} |g\rangle &= \sqrt{1-\rho}|N\rangle + \sqrt{\rho}|Z_+\rangle \\ |c\rangle &= |Z_-\rangle \\ |e\rangle &= \sqrt{\rho}|N\rangle - \sqrt{1-\rho}|Z_+\rangle \end{aligned} \tag{1.21}$$

where the expectation value of $\hat{\rho}$, which measures the amount of charge separation in the ground state, and thereby the quadrupolar moment of the molecule, is a function of $z/\sqrt{2}\tau$:

$$\rho = \frac{1}{2}\left(1 - \frac{z}{\sqrt{z^2 + 2\tau^2}}\right) \tag{1.22}$$

In Eqn. 1.21, we can see that $|Z_-\rangle$ remains unmixed with the other basis states owing to its different parity. Here we also assume that the only non-negligible contribution to the dipole moment comes from $|DA^-D^+\rangle$ and $|D^+A^-D\rangle$ states, having

same dipole moment μ_0 aligned along the molecular axis (in opposite directions).

Finally, the relevant terms for spectral calculations, namely, transition frequencies and transition dipole moments, for a linear molecule become:

$$\begin{aligned} \hbar\omega_{gc} &= 2t\sqrt{\frac{1-\rho}{\rho}} & \mu_{gc} &= \mu_0\sqrt{\rho} \\ \hbar\omega_{ge} &= 2t\sqrt{\frac{1}{\rho\,(1-\rho)}} & \mu_{ge} &= 0 \\ \hbar\omega_{ce} &= 2t\sqrt{\frac{\rho}{1-\rho}} & \mu_{ce} &= -\mu_0\sqrt{1-\rho} \end{aligned} \tag{1.23}$$

For linear quadrupolar dyes, the $|c\rangle$ state is OPA allowed and $|e\rangle$ state having $\mu_{ge} = 0$, is dark and TPA allowed. For large values of z, the ground state is mostly neutral ($\rho \to 0$) making both OPA and TPA transitions degenerate. For $z = 0$ and $\rho = 0.5$, the TPA allowed $|g\rangle \to |e\rangle$ transition is exactly twice the energy of $|g\rangle \to |c\rangle$ transition, while when $\rho \to 1$, $|g\rangle$ and $|c\rangle$ states become degenerate. The intensity of OPA transition increases linearly with ρ and the TPA transition diverges when $\rho \sim 0.5$, due to pre-resonance with OPA state.

We have not considered molecular vibrations and solvation effects for DAD molecules, using three-state model, in the works pertaining to this thesis and hence not discussed here.

1.3.2 Study of Interacting Chromophores

Self-aggregation of dyes in solution or at the solid-liquid interface is a frequently observed phenomenon in the chemistry of chromophores due to the presence of strong intermolecular interactions. The aggregates exhibit noticeable changes in the absorption band in solution, compared to monomeric species. Depending on the spectral shifts, various aggregation patterns in different media have been suggested. According to the Exciton Theory [69], a dye molecule is visualized as a point dipole and, as exemplified in Fig. 1.5 for a dimer, the excitonic level of the dye aggregate divides into two states and the gap (J) between the splitted states is a result of the electrostatic interaction of the transition dipole moments (Fig. 1.5).

When the absorption spectra is red-shifted (bathochromic shift) with respect to the monomer, the aggregate is named as *J-band* (J stands for the name of

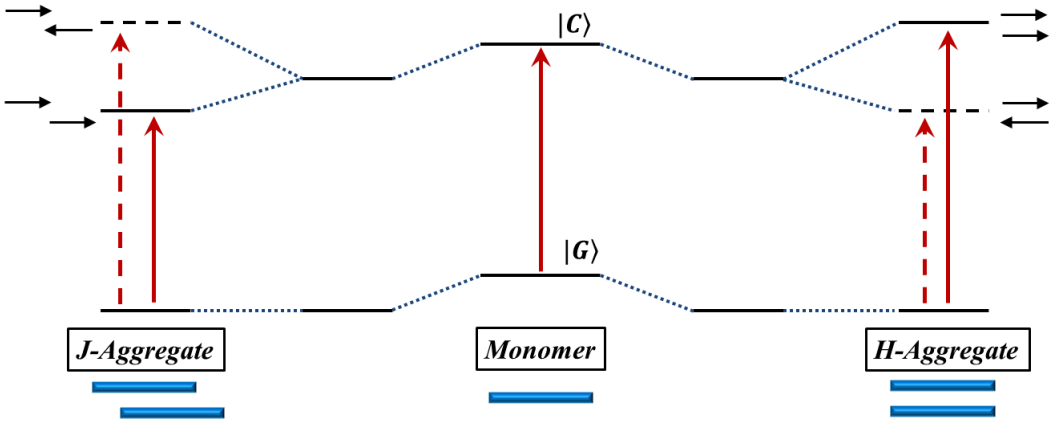

Figure 1.5: The excitonic model transitions for a monomer dye and its dimer, in J- and H-aggregates. Red arrows indicate the transitions and black arrows indicate the orientation of the transition dipoles.

E.E. Jelley who discovered the phenomenon in 1936) [99], while if it is blue-shifted (hypsochromic shift) compared to the monomer, it is called *H-band* (*H* comes from Hypsochromic). Since the lowest excited state is optically allowed in *J-aggregates*, while it is forbidden in *H-aggregates*, the two families of aggregates have different properties with respect to fluorescence; *J-aggregates* are usually fluorescent, while fluorescence is suppressed in *H-aggregates*.

As have been discussed in Refs. [72] and [71], the exciton model fails for aggregates of polarizable molecules, like DA or DAD dyes, and ESM offers a powerful alternative approach to rationalize optical spectra of interacting dyes. In this thesis, Chapter 2 will be devoted to develop and validate models for aggregated quadrupolar dyes, while in Chapter 3 we will discuss aggregates of dipolar dyes.

1.3.3 Density Functional Theory (DFT)

Density functional theory (DFT) furnishes a powerful tool for computations of the quantum state of atoms, molecules and solids, and also for *ab-initio* molecular dynamics. The approximation was first conceived by Thomas [100] and Fermi [101] immediately after the foundation of quantum mechanics, in 1927. Around mid sixties, Hohenberg, Kohn and Sham established a rigorous DFT for ground state properties of a quantum system and introduced an approximate explicit theory for

the density, called the local-density approximation (LDA). LDA proved to be superior to both Thomas-Fermi and Hartree-Fock theories for the computation of the quantum ground state of many-particle systems. Since then, DFT has grown vastly in terms of popularity and applicability, and a flood gate has opened in the field of computational studies in molecular and solid state physics - from molecules to bulk systems, from insulators to metals, from diamagnetic to ferromagnetic materials. Motivated by its success, there lied always a tendency to widen the scope of application of DFT, and in these developments, some points which were left somewhat cryptic in the fundamental theory has come up from time to time.

DFT treats electronic degrees of freedom and it is rooted in the adiabatic or Born-Oppenheimer (BO) approximation which takes care of the number of degrees of freedom needed to be reduced.

1.3.3.1 Born-Oppenheimer (BO) Approximation

We may write the non-relativistic Hamiltonian for a molecule as a sum of five terms:

$$\hat{H} = \hat{T}_N(\mathbf{R}) + \hat{T}_e(\mathbf{r}) + \hat{V}_{eN}(\mathbf{r}, \mathbf{R}) + \hat{V}_{NN}(\mathbf{R}) + \hat{V}_{ee}(\mathbf{r}) \tag{1.24}$$

where $\mathbf{R}$ is the set of nuclear coordinates and $\mathbf{r}$ is the set of electronic coordinates. $\hat{T}_{N/e}$ is the kinetic energy of nuclei/electrons, $\hat{V}_{NN}$ and $\hat{V}_{ee}$ are the potentials for the repulsion among nuclei and electrons, respectively, and $\hat{V}_{eN}$ is the attraction between electrons and nuclei. This last term prevents from separating $\hat{H}$ into nuclear and electronic components, to write the molecular wavefunction as product of nuclear and electronic terms. The BO approximation is based on the fact that the nuclei are much more massive than the electrons, which allows us to say that the position of nuclei are nearly fixed with respect to electron motion. Thus when solving the electronic problem $\mathbf{R}$, the nuclear configuration, is maintained constant and the electronic wavefunction $\Psi(\mathbf{r}; \mathbf{R})$, acquires a parametric dependence on $\mathbf{R}$. Since $\hat{V}_{NN}(\mathbf{R})$ is a constant, and shifts the eigenvalues only by some constant amount, it is neglected and the electronic Hamiltonian simplifies into:

$$\hat{H}_e = \hat{T}_e(\mathbf{r}) + \hat{V}_{eN}(\mathbf{r}; \mathbf{R}) + \hat{V}_{ee}(\mathbf{r}) \tag{1.25}$$

and the corresponding electronic Schrödinger equation becomes:

$$\hat{H}_e \Psi(\mathbf{r}, \mathbf{R}) = E_e(R) \Psi_e(\mathbf{r}, \mathbf{R}) \tag{1.26}$$

In DFT, the energy as well as other ground state properties, are expressed as functionals (function of a function) of the electron-density, which, in turn, is a function of space and time. It is the most fundamental property, at variance with the Hartree-Fock model, which explicitly deals with the electronic wavefunction. Using the electron density significantly speeds up the calculation. Whereas the electronic wavefunction is a function of 3N variables (the coordinates of all N electrons in the system), the electron density is only a function of the spatial x, y, and z coordinates. For sure, simply doing any calculation just fast is not good enough, we also need to be sure that we are able to derive something significant from the results. It was in 1964 that Hohenburg and Kohn [102] stated two theorems, which tell us that the ground state electron density $\rho_0(r)$ is very useful and can be produced by *at most one* external one-body potential, and determines all ground-state properties of the system.

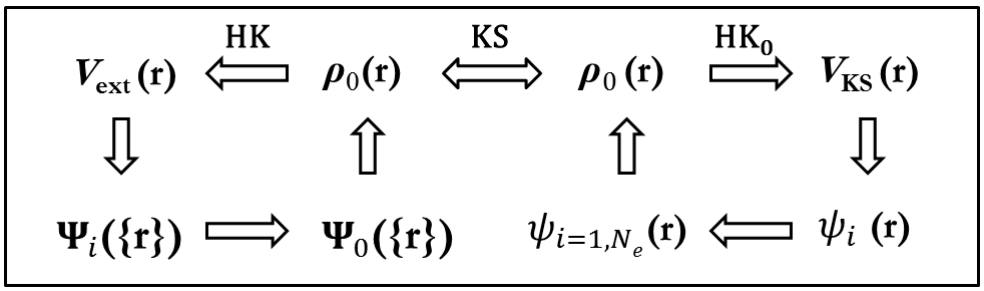

Figure 1.6: Dependence of the ground state wavefunction on $\rho_0(r)$ from Hohenberg-Kohn (HK) theorems and Kohn-Sham (KS) equation perspective

To utilize the power of DFT, without sacrificing accuracy (*i.e.*, inclusion of exchange and correlation effects), the Kohn-Sham equations [103] came to the rescue in 1965. The equations map the problem of the system of interacting electrons onto a fictitious system of non-interacting "electrons". Following from BO approximation, the Coulomb potential arising from the nuclei is treated as a static external potential $V_{ext}(r)$. Thus the variational problem of Hohenberg-Kohn density-functional is written introducing a Lagrange multiplier μ to constrain the number of electrons

to N, as:

$$\delta[F[\rho] + \int dr V_{ext}(r)\rho(r) - \mu(\int dr\rho(r) - N)] = 0 \tag{1.27}$$

Kohn and Sham separated $F[\rho]$ (universal functional which is independent of the external potential) into three parts:

$$F[\rho] = T_s[\rho] + \frac{1}{2} \int dr dr' \frac{\rho(r)\rho(r')}{\mid r - r' \mid} + E_{xc}[\rho] \tag{1.28}$$

In Eqn. 1.28, $T_{\rm s}[\rho]$ is defined as the kinetic energy of a non-interacting gas with density $\rho(\mathbf{r})$, the second term stands for the classical electrostatic (Hartree) energy and the last term is an implicit definition of the exchange-correlation energy that includes the non-classical electrostatic interaction energy and the difference between the kinetic energies of the interacting and non-interacting systems. This separation was aimed for the fact that the first two terms can be dealt with easily and the last term is a small fraction of the total energy and can be approximated appreciably well. Thus, using Eqn. 1.28, Eqn. 1.27 is written as:

$$\frac{\delta T_{\rm s}[\rho]}{\delta\rho(r)} + V_{{\rm K}S}(r) = \mu \tag{1.29}$$

where $V_{{\rm K}S}(r)$ is given as:

$$V_{\rm KS}(r) = \int dr' \frac{\rho(r')}{\mid r - r' \mid} + V_{\rm xc}(r) + V_{ext}(r) \tag{1.30}$$

The exchange-correlation potential $V_{\rm xc}(r)$ used in the above equations, thus is:

$$V_{\rm xc}(r) = \frac{\delta E_{\rm xc}[\rho]}{\delta\rho(r)} \tag{1.31}$$

Hence, to find the ground state density $\rho_0(r)$, it is needed to solve the one-electron Schrödinger equations of a non-interacting system, which is:

$$\left[-\frac{1}{2}\nabla^2 + V_{{\rm K}S}(r)\right]\psi_i(r) = \epsilon_i\psi_i(r) \tag{1.32}$$

The density $\rho(r)$ can thus be constructed from,

$$\rho(r) = \sum_{i=1}^{N} f_i |\ \psi_i(r)\ |^2 \tag{1.33}$$

f_i being the occupation number of ith orbital. Since the Kohn-Sham potential $V_{\mathrm{KS}}(r)$ depends upon $\rho(r)$ it is crucial to solve these equations "self-consistently" *i.e.* having made a guess about the form of ρ, the Schrödinger equation is solved to obtain a set of orbitals $\psi_i(r)$ and a new density is constructed. The process repeated until the input and output densities are the same, this being popularly known as the "self-consistency cycle" or SCF. In effect there is no problem converging to the ground-state minimum because of the convex nature of the density-functional [104, 105]. Since V_{xc} is not known exactly and has to be approximated, following approximations are put to use:

1. **Local Density Approximation (LDA):**

   Local Density Approximation (LDA) [106] assumes that the electron density is a smooth function in space and is the first approximation to V_{xc}, defined as:

   $$V_{\mathrm{xc}}{}^{LDA} = \int d^3r \epsilon_{xc}(\rho(r)) \cdot \rho(r) \tag{1.34}$$

   $\epsilon_{xc}(\rho(r))$ stands for the exchange and correlation energy per electron of the homogeneous electron gas with density $\rho(r)$. Any region of space can then be locally seen as a homogeneous electron gas of density $\rho(r)$ and the total exchange-correlation energy is then obtained by summing sum over all electrons in every region of space of the local exchange-correlation energy. Over the years, this functional has become quite popular, by combining limiting information with accurate quantum Monte Carlo data for the uniform gas. However, pure LDA shows poor performance whenever there is an odd number of electrons, because it makes no distinction between polarized and unpolarized densities.

2. **Generalized Gradient Approximation (GGA):** As mentioned above, LDA fails in situations where the density undergoes rapid changes such as in molecules, so an improved version to LDA was made considering the gradient

of the electron density, called Generalized Gradient Approximation (GGA). These are formulas that use both the density and its gradient at each point and with this added information (and cost of computing it), these are typically more accurate than LDA. Most important point being they greatly reduce the bond dissociation energy error, and generally improve transition-state barriers [105]. It is written as:

$$V_{\mathrm{xc}}{}^{GGA} = V_{\mathrm{xc}}\left[\rho(r), \nabla\rho(r)\right] \tag{1.35}$$

Use of GGA has resulted in very good results for molecular geometries and ground-state energies [107]. There are three categories of GGA functionals, namely:

(i) Atom Based GGA functionals, for example Beckes GGA for exchange [108] and and Lee Yang and Parr (LYP) functional for correlation [109]
(ii) *Ab initio* GGA, for example PBE (Perdew-Burke-Ernzerhof) [110] or PW91 (Perdew-Wang 1991) [111, 112]
(iii) Empirical GGA, for example HCTH (Hamprecht-Cohen-Tozer-Handy) functionals [113, 114]

More accurate than the GGA functionals are the meta-GGA functionals, developed after the GGA. Meta-GGA DFT functional in its original form includes the second derivative of the electron density (the Laplacian) unlike GGA which includes only the density and its first derivative in the exchange-correlation potential. Examples of meta-GGA functionals are Minnesota functionals, developed by the group of Prof. Donald Truhlar at the University of Minnesota [115–117].

1.3.4 Time-Dependent Density Functional Theory (TDDFT)

Under certain general conditions, a one-to-one correspondence can be established between time-dependent densities [ρ(r,t)] and potentials $V_{ext}(r,t)$ for a given initial state. This implies, a given evolution of the density can be generated by at

most one time-dependent potential, the time-dependent analog of the Hohenberg-Kohn theorem, and is called the Runge-Gross theorem [118]. Then a fictitious system of non-interacting electrons moving in a Kohn-Sham potential can be defined, whose density is precisely that of the real system. The exchange-correlation potential thereby (defined in the usual way) is then a functional of the entire history of the density, $\rho(x)$, the initial interacting wavefunction Ψ_0, and the initial Kohn-Sham wavefunction, ψ_0. This functional is a very complex one, more than the ground-state case and the knowledge of it implies solution of all time-dependent Coulomb-interacting problems. A simple approximation is the adiabatic LDA (ALDA), sometimes called time-dependent LDA, where the ground-state potential of the uniform gas is used with that of instantaneous and local density, i.e., $V_{\rm xc}[\rho](x)$ equivalent to $V_{\rm xc}^{uniform}[\rho(x)]$. This provides a working Kohn-Sham scheme, similar to the ground state. This DFT methodology can be applied to all problems of time-dependent electrons and the applications fall into three general categories: (i) non-perturbative regimes, (ii) linear (and higher-order) response, and (iii) ground-state applications. Previously, only one and two electron systems could be tackled computationally, since the full time-dependent wavefunction calculations are pretty demanding. Thus, crude and unreliable approximations had to be made to tackle larger systems. But with the advent of TDDFT, which has become very popular in the community of chemists and physicists alike, much larger systems with more electrons can now be dealt with.

If the perturbing field is weak, in case of normal spectroscopic experiments, perturbation theory is applicable. Then, instead of needing knowledge of $V_{\rm xc}$ for densities that are changing significantly with time, only the knowledge of this potential in the vicinity of the initial state, taken to be a non-degenerate ground-state, are sufficient. These changes are described by a new functional, the exchange-correlation kernel. While still a more complex beast than the ground-state exchange-correlation potential, the exchange-correlation kernel can be more easily handled than the full time-dependent exchange-correlation potential, because it is a functional of the ρ_0 only. Linear response analysis shows that it is generally dominated by the response of the ground-state Kohn-Sham system, but is corrected by TDDFT via matrix elements of the exchange-correlation kernel. However, in the absence of Hartree-exchange-correlation effects, the allowed transitions are exactly those of

the ground-state KS potential, while presence of the kernel shifts the transition frequencies away from the KS values to the actual ones.

Physicists and chemists have adopted separate techniques for extracting excitations from TDDFT for atoms, molecules, and clusters. The chemists' approach is efficiently converting the search for poles of response functions into a large eigenvalue problem, in a space of the single-excitations of the system. The eigenvalues give transition frequencies while the eigenvectors yield oscillator strengths (designated generally as f). This concedes the use of many existing fast algorithms to extract a few of the lowest energy transitions. TDDFT has thus been programmed into large number of quantum chemical (QM) packages, which are used today amongst the scientific community, where after a molecule's structure has been determined, extracting its low-lying spectrum isn't much expensive. TDDFT response calculations are being used enormously nowadays for transition frequencies with fairly good accuracy, but there are existing problems for the application of TDDFT to solids, because the present generation of approximate functionals (local and semi-local) lose important effects in the thermodynamic limit.

1.3.5 ZINDO Model

The semi-empirical approach of intermediate neglect of differential overlap for spectroscopy (INDO/S) was developed nearly 50 years ago, in order to treat excited state properties of π-conjugated organic molecular systems, particularly with H, C, N and O atoms [119, 120]. In recent times, the method is widely used for calculating UVvis spectra, ionization potentials (IPs), polarizabilities, charge distribution, electron-transfer parameters, and various other properties of extended organic, inorganic, and biomolecules. Study of excited states are quite fascinating and also modern experimental technique gives the chance to study photophysical processes on a femtosecond time scale. However, despite enormous advancement in numerical methods and computational resources, the accurate description of electronically excited states is still a problem to tackle. This arises mostly due to molecular size which restricts till the calculations of the ground-state properties and various precise methods like MS-CASPT2, CAS-SCF, TDDFT are good till about 50 atoms containing molecules. On the other hand, QM semi-emperical approaches are much less computationally demanding than the high-level *ab initio* methods and these have

been proved to be very beneficial in modeling ground- and excited-state properties of molecular systems. Even though an accurate and robust family of semi-emperical approach was developed by Pople, called Neglect of Diatomic Differential Overlap (NDDO) [121, 122] is in use, the INDO/S method suggested by Zerner and Ridley (ZINDO) is still widely used to explore electronic transitions in large molecular systems.

The ZINDO method relies on the INDO approximation [123], and Zerner and Ridley suggested a set of semiempirical parameters to calculate electronic spectra of organic molecules [124]. The Fock matrix for a closed shell system is given by:

$$\begin{aligned} F_{\mu\mu} =& U_{\mu\mu} + \sum_{A\neq B} V_{\mu\mu,B} + \sum_{\nu\in A} P_{\mu\mu}\left(\gamma_{\mu\nu} - \frac{1}{2}\, h_{\mu\nu}\right) \\ & \sum_{B\neq A}\sum_{\lambda\in B} P_{\lambda\lambda}(\mu\mu|\lambda\lambda), (\mu,\nu\in A, \lambda\in B) \end{aligned} \tag{1.36a}$$

$$F_{\mu\nu} = \frac{1}{2}\, P_{\mu\nu}\left(3h_{\mu\nu} - \gamma_{\mu\nu}\right), (\mu,\nu\in A) \tag{1.36b}$$

$$F_{\mu\lambda} = \beta_{\mu\lambda} - \frac{1}{2}\, P_{\mu\lambda}(\mu\mu|\lambda\lambda), (\mu\in A, \lambda\in B) \tag{1.36c}$$

where, μ, ν stands for atomic orbitals (AOs) of an atom A, and λ refers to AOs of another atom B. The "one centre one electron" energy is $U_{\mu\mu}$ and $\gamma_{\mu\nu}$ and $h_{\mu\nu}$ are "1centre" Coulomb and exchange integrals, respectively. In Ridley and Zerner's modified INDO method, $\gamma_{\mu\nu}$'s are set to be equal for s and p orbitals, such that $\gamma_{ss} = \gamma_{sp} = \gamma_{pp} = \gamma_{AA}$ and γ_{AA} is estimated as the difference between the ionization potential (IP) and electron affinity (EA) of atom A. The exchange integrals h_{sp} and h_{pp} are written using SlaterCondon parameters, $h_{sp} = (1/3)G^1_{sp}$ and $h_{pp} = (3/25)F^2_{pp}$, derived from atomic spectral nature. The average energy of an atomic configuration $s^k p^m$ is thereby given as:

$$E(s^k p^m) = kU_{ss} + mU_{pp} + \frac{1}{2}\, k(k-1)\bar{\gamma}_{ss} + \frac{1}{2}\, m(m-1)\bar{\gamma}_{pp} + km\bar{\gamma}_{sp} \tag{1.37}$$

Since, energy difference of two atomic configurations and the experimental ionization energy I_μ gives $U_{\mu\mu}$, and $I_s = E(s^{k-1}p^m) - E(s^k p^m)$ and $I_p = E(s^k p^{m-1}) -$

$E(s^k p^m)$, U_{ss} and U_{pp} are thereby calculated. The relation between resonance integral ($\beta_{\mu\lambda}$) and overlap integral $S_{\mu\lambda}$ is therefore given as,

$$\beta_{\mu\lambda} = f_{\mu\lambda} \left(\beta_\mu + \beta_\mu\right) S_{\mu\lambda} \tag{1.38}$$

and, $f_{\mu\lambda}$ is taken as 1.267 and 0.585 for σ and π orbital overlaps, respectively. In ZINDO calculations of triplet excited states, recommended value of $f_{\pi\pi} = 0.680$ (instead of $f_{\pi\pi} = 0.585$) is considered.

In the beginning, the ZINDO scheme was parameterized for elements H, C, N, and O atoms and the original parameterization scheme considered I_p and β for O atom to be equal to 17.28 and 34 eV. Later on, the values were replaced by 15.88 and 54 eV, respectively. Owing to the fact that some of the integrals are neglected within the INDO scheme, the other integrals should be averaged in order to retain the rotational invariance of the method. Recent advancement in higher-level *ab initio* computations of excited state properties has opened the door for development of a modified method of higher predictive accuracy. ZINDO method is presently implemented in various quantum chemical software packages in order to calculate vertical excitation energies and properties of molecules having large number of atoms and cannot be applied to optimize molecular geometries or to search for transition-state structures, for which we need to rely on QM or molecular mechanics (MM) methods. The INDO/S scheme is not recommended for calculation of the ground-state energetics including heats of formation, relative energies of isomers and conformers, activation barriers, and intermolecular interactions and it is to be noted that like other semiempirical methods, INDO/S also suffers from occasional drawbacks, and therefore, it is necessary for preliminary test calculations to understand reliability for a particular system.

In this thesis, we have also presented works using ZINDO calculations to understand the manifold of excited states in a dipolar chromophore (Chapter 4).

1.3.6 Model Hamiltonians and Density Matrix Renormalization Group (DMRG) Theory

1.3.6.1 Second Quantization

Taking the clue from Eqn. 1.25, a model Hamiltonian can be constructed for the π-electrons only. In general terms it can be separated into a one-electron and a two-electron part, as below:

$$\hat{H}_{\pi} = \hat{H}_{1elec} + \hat{H}_{2elec} \tag{1.39}$$

The formalism of second quantization, also called canonical quantization, is used to describe and analyze quantum many-body systems. The idea, first introduced by Dirac and developed later by Fock and Jordan, deals with fields (typically as the wave functions of matter) which are thought of as field operators, in a manner similar to how the physical quantities (position, momentum, etc.) are thought of as operators in first quantization. This introduces the concept of creation and annihilation operators to construct and handle Fock states. In Eqn. 1.39, the "1elec" part is assumed such that the π electrons move in an effective field of nuclear attraction and the electron repulsion of all σ electrons. The "2elec" part denotes the e-e repulsion felt by the π electrons due to the other π electrons. If the "1elec" part is represented by the Hamiltonian matrix $h_{\mu\nu}$ and the "2elec" part includes all possible repulsion integrals [125], the total Hamiltonian becomes:

$$\hat{H}_{\pi} = \sum_{\mu\nu} h_{\mu\nu}\hat{E}_{\mu\nu} + \frac{1}{2}\sum_{\mu\nu\mu'\nu'} [\mu\nu|\mu'\nu'](\hat{E}_{\mu\nu}\hat{E}_{\mu'\nu'} - \delta_{\nu\mu'}\hat{E}_{\mu\nu'}) \tag{1.40a}$$

$$\hat{E}_{\mu\nu} = \sum_{\sigma} \hat{a}^{\dagger}_{\mu,\sigma}\hat{a}_{\nu,\sigma} \tag{1.40b}$$

In Eqn. 1.40b $\hat{a}^{\dagger}_{\mu,\sigma}$ is the creation operator (the basic object of second quantization) and $\hat{a}_{\mu,\sigma}$ is the annihilation operator, of an electron with spin σ in the μth π orbital, while, $[\mu\nu|\mu'\nu']$ is the "2elec" integral given in cloud charge notation.

1.3.6.2 Zero Differential Overlap (ZDO) to Hubbard Model

The Hubbard Model, though can be derived from Eqn. 1.40a, was put on paper independently by Kanamori [126], Gutzwiller [127] and Hubbard [128, 129] in the 1960s, on a different context of ferromagnetism in metals. The ZDO approximation [130] curbs the non-zero electron repulsion integrals to those of the form $[\mu\mu|\nu\nu]$, which means that the "2elec" integrals are non-zero only when charge density of one electron is present fully in an orbital μ and for the other electron in ν. Since the Hubbard Model too restricts the non-vanishing "2elec" integrals to the type $[\mu\mu|\mu\mu]$, it is thus written as:

$$\hat{H}_{Hubbard} = \sum_{\mu\sigma} \alpha_\mu \hat{a}^\dagger_{\mu\sigma}\hat{a}_{\mu\sigma} + \sum_{\langle\mu\nu\rangle\sigma} t_{\mu\nu}\left(\hat{E}_{\mu\nu} + h.c.\right) + \frac{U}{2}\sum_{\mu}\hat{n}_\mu\left(\hat{n}_\mu - 1\right) \qquad (1.41)$$

The Hubbard Hamiltonian therefore includes α_μ which is the orbital or site energy at site μ, $t_{\mu\nu}$ which is the resonance or transfer integral between the bonded sites, $h.c.$ which is the Hermitian conjugate, $\hat{n}_\mu$ which is the number operator at site μ. It also includes the on-site repulsion integral (U), which is taken to be the absolute difference of the ionization potential (IP) and electron affinity (EA) of the atom. The first two terms of Eqn. 1.41 makes up the Hückel Hamiltonian where the "2elec" integrals are completely neglected and the Hamiltonian matrix of the "1elec" part is considered to have non zero elements along the diagonal and for the pair of π orbitals μ, ν, located on atoms connected by a σ-bond. The Hückel Hamiltonian has been widely used earlier for its simplicity and the physical interpretation it provides [131, 132].

In its simplest form the Hubbard model is a one-parameter model involving U for the fact that all the energies can be scaled in units of t. It is the simplest model that incorporates the essence of electron correlations and has been widely studied over decades.

1.3.6.3 Pariser-Parr-Pople (PPP) Model

Almost a decade earlier than Hubbard model was derived, Pariser and Parr [133], and Pople [134] independently derived another Hamiltonian from Eqn. 1.40a, using

ZDO approximation. This model has been since used for the study of electronic states of conjugated systems and here a site chemical potential is used in the intersite interaction part so that all the Carbon sites remain electrically neutral when they are singly occupied. This can be possible when z_μ is considered equal to 1 in Eqn. 1.42 as given by:

$$\hat{H}_{PPP} = \hat{H}_{Hubbard} + \sum_{\mu>\nu} V_{\mu\nu} \left(\hat{n}_\mu - z_\mu\right) \left(\hat{n}_\nu - z_\nu\right) \tag{1.42}$$

Here, the off-site electron repulsion integrals $V_{\mu\nu}$ are interpolated smoothly between U for zero intersite separation and e^2/r_{12} for intersite separation leading to infinity, thereby by-passing explicit calculation of repulsion integrals. In the Ohno interpolation scheme, developed by Ohno [135] and Klopman [136], $V_{\mu\nu}$ is expressed as:

$$V_{\mu\nu} = 14.397 \left(\frac{28.794}{\left(U_\mu + U_\nu\right)^2} + r_{\mu\nu}^2 \right)^{-0.5} \tag{1.43}$$

where, $r_{\mu\nu}$ is the distance between μ and ν sites and is in Å unit, while, U and V are in eV.

The PPP model hasn't been solved analytically, unlike Hubbard model in 1D and the numerical exact solutions are restricted to systems with about 16 orbitals at half-filling. The model has been successful for studying low-energy excitation spectrum of many conjugated systems of interest and the parameters for C and N atoms are fairly well standardized. The results obtained with PPP model are in good agreement with the experimental results.

1.3.6.4 Density Matrix Renormalization Group

Density matrix renormalization group (DMRG) [137, 138] is a numerical algorithm for the efficient truncation of the Hilbert-space of low-dimensional strongly correlated quantum systems, based on a general decimation rule. This has been accepted as having unprecedented precision in describing 1-dimensional quantum systems. It relies on the concept of reduced density matrix and was introduced by Steven R. White in 1992. DMRG is used for a variety of problems; for example, to treat very large systems with hundreds of spins, to provide accurate results for

ground state energies and gaps for low-dimensional system, *etc.*

- **Infinite System DMRG**

  In the infinite system DMRG, one starts with a small number of sites, which is called Superblock (see Fig. 1.7(a)). Using ED, one creates the Hamiltonian of the superblock, then by diagonalization of this Hamiltonian matrix we can get the wavefunction $|\psi\rangle = \sum_{LR} C_{LR}|L\rangle|R\rangle$. This helps to obtain the reduced density matrix ($\rho_{LL'}$) of the left block: $\rho_{LL'} = \sum_R C^*_{LR} C^*_{LR}$.

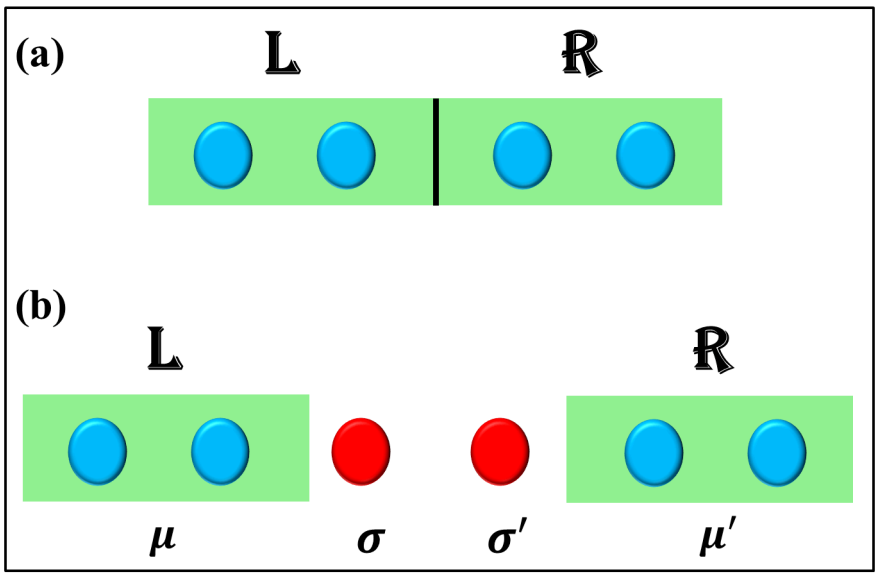

Figure 1.7: (a) Schematic diagram for superblock showing left (L) and right (R) blocks, (b) Superblock structure with left and right block in the density matrix basis $(\mu, \mu^{'})$ and two new sites in site basis $(\sigma, \sigma^{'})$

.

Diagonalization of $\rho_{LL'}$ gives a set of eigenvalues and eigenvectors, from which m eigenvalues corresponding to m largest eigenvectors are kept. Then a transformation matrix $O_{n,m}$ is formed, where n is the actual dimension while m is the cutoff dimension. Using $O_{n,m}$ the Hamiltonian is renormalized, along with the required operators of the left and right blocks into density matrix eigenvectors (DMEV) basis, such that: $\hat{A}_{m\times m} = O^{\dagger}_{m\times n} A_{n\times m} O_{n\times m}$. Now, adding two sites in the middle (see Fig. 1.7(b)) the Hamiltonian matrix of the superblock is constructed in the basis $|\mu, \sigma, \sigma^{'}, \mu^{'}\rangle$, after which the Hamiltonian

matrix is diagonalized to get the ground state wave function $\psi(\mu, \sigma, \sigma^{'}, \mu^{'})$. This process is repeated again by forming half block reduced density matrix, transformation matrix, half block Hamiltonian operators and the other operators. Further, two new sites are added and the same methodology is repeated till thermodynamic limit is achieved or the energy converges. If the finite DMRG is of one's interest, the infinite DMRG scheme is adopted till that particular system size is achieved and then one proceeds for finite-DMRG method.

- **Finite System DMRG**

To improve the accuracy achieved using Infinite size DMRG method, Finite size DMRG is done. Once the desired system size (say, N) is reached, the L and R block operators are stored, and the length of the L block is increased by adding one site from the R block, keeping N fixed (see Fig. 1.8). Thus the superblock structure now has $L+1$ on left and $R-1$ on right, with two sites in between. The superblock Hamiltonian is then diagonalized following the same routine as the Infinite size, till one reaches $N-3$ sites on L block and R block has one remaining site. Then the size of the L block starts decreasing, with increase in R block size, such that at the end there are $\frac{N}{2} - 1$ sites on both L and R blocks. This marks the completion of one interation or one full sweep, called *finite size sweeping*. Similar to the case of Infinite size again, here too one obtains now the ground state wave-function $\psi(\mu, \sigma, \sigma^{'}, \mu^{'})$ and the desired properties are calculated, like bondorder, charge density, correlation, spin density, *etc.*

If the L and R block operators are denoted by O_i^L and O_j^R, respectively, the basis sets for L block is $|\alpha\rangle = |\mu\sigma\rangle$ or $\langle\alpha^{'}| = \langle\nu\tau|$, and for the R block is $|\beta\rangle = |\mu^{'}\sigma^{'}\rangle$ or $\langle\beta^{'}| = \langle\nu^{'}\tau^{'}|$. Thus the ground state wave-function in the DMRG basis is:

$$|\psi\rangle = \sum_{\alpha\beta} C_{\alpha\beta}|\alpha\beta\rangle \tag{1.44}$$

Hence, the expectation value of any operator O_i^L, like spin density or charge

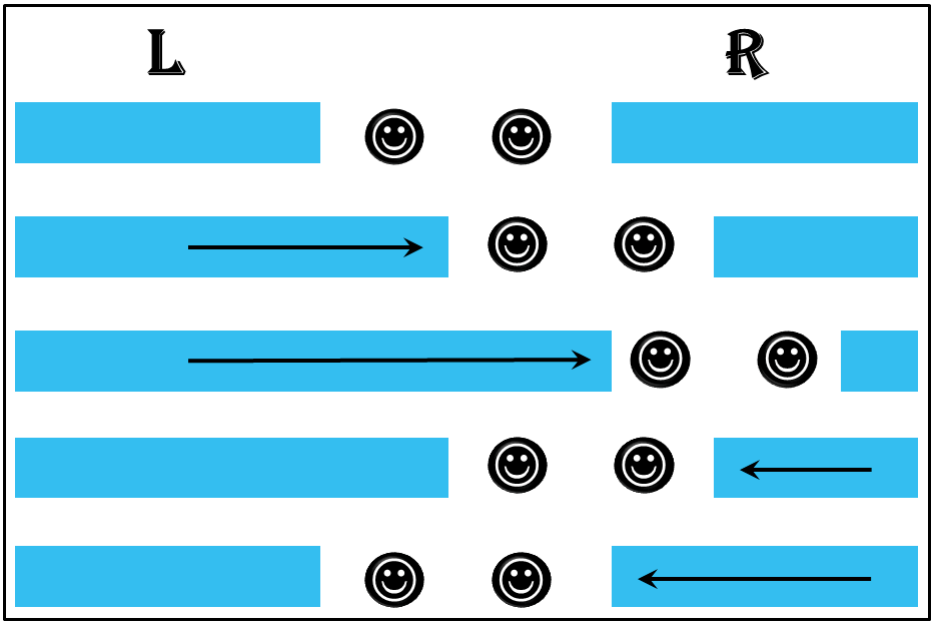

Figure 1.8: One *finite size sweeping* of Finite System Size DMRG, for system size N

.

density, is given as:

$$\langle\psi|O_i^L|\psi\rangle = \sum_{\alpha\beta,\alpha'} C^*_{\alpha'\beta} C_{\alpha\beta} \langle\alpha|O_i^L|\alpha'\rangle \tag{1.45}$$

And, the corresponding correlation functions of L and R block is thus written as:

$$\langle\psi|O_i^L O_j^R|\psi\rangle = \sum_{\alpha\beta,\alpha'\beta'} C^*_{\alpha'\beta'} C_{\alpha\beta} \langle\alpha|O_i^L|\alpha'\rangle\langle\beta|O_j^R|\beta'\rangle \tag{1.46}$$

To find four-point correlation function, or correlation function from same block corresponding product operators renormalized in every infinite and finite DMRG steps are required to be kept.

Bibliography

[1] L. Beverina and G. A. Pagani, Acc. Chem. Res. **47**, 319 (2014).

[2] G. Drummen, Molecules **17**, 1406714090 (2012).

[3] P. G. Ranky and M. F. Ranky, "Cd-roms, dvd-roms, and computer systems," in *Wiley Encyclopedia of Electrical and Electronics Engineering* (John Wiley & Sons, Inc., 2001).

[4] V. Parthasarathy, S. Fery-Forgues, E. Campioli, G. Recher, F. Terenziani, and M. Blanchard-Desce, Small **7**, 3219 (2011).

[5] O. S. Wolfbeis, Chem. Soc. Rev. **44**, 4743 (2015).

[6] S. Kawata, H.-B. Sun, T. Tanaka, and K. Takada, Nature **412**, 697 (2001).

[7] A. Ovsianikov, A. Ostendorf, and B. Chichkov, Appl. Surf. Sci. **253**, 6599 (2007), proceedings of the Fifth International Conference on Photo-Excited Processes and Applications(5-ICPEPA).

[8] M. Farsari and B. N. Chichkov, Nat. Photon. **3**, 450 (2009).

[9] S. R. Marder, L.-T. Cheng, B. G. Tiemann, A. C. Friedli, M. Blanchard-Desce, J. W. Perry, and J. Skindhøj, Science **263**, 511 (1994).

[10] S. R. Marder, C. B. Gorman, B. G. Tiemann, and L. T. Cheng, J. Am. Chem. Soc. **115**, 3006 (1993).

[11] S. R. Marder, Chem. Commun. , 131 (2006).

[12] B. Strehmel, A. M. Sarker, and H. Detert, ChemPhysChem **4**, 249 (2003).

[13] F. Terenziani, A. Painelli, C. Katan, M. Charlot, and M. Blanchard-Desce, J. Am. Chem. Soc. **128**, 15742 (2006).

[14] V. Bulović, A. Shoustikov, M. Baldo, E. Bose, V. Kozlov, M. Thompson, and S. Forrest, Chem. Phys. Lett. **287**, 455 (1998).

[15] V. Bulović, R. Deshpande, M. Thompson, and S. Forrest, Chem. Phys. Lett. **308**, 317 (1999).

[16] D. Chen, K. Liu, L. Gan, M. Liu, K. Gao, G. Xie, Y. Ma, Y. Cao, and S.-J. Su, Adv. Mat. **28**, 6758 (2016).

[17] S. Di Bella, M. A. Ratner, and T. J. Marks, J. Am. Chem. Soc. **114**, 5842 (1992).

[18] C. Dehu, F. Meyers, E. Hendrickx, K. Clays, A. Persoons, S. R. Marder, and J. L. Brédas, J. Am. Chem. Soc. **117**, 10127 (1995).

[19] X. Liu, Z. Yang, D. Wang, and H. Cao, Crystals **6**, 158 (2016).

[20] A. Abbotto, L. Beverina, N. Manfredi, G. Pagani, G. Archetti, H.-G. Kuball, C. Wittenburg, J. Heck, and J. Holtmann, Chem. Eur. J. **15**, 6175 (2009).

[21] R. M. Metzger, B. Chen, U. Höpfner, M. V. Lakshmikantham, D. Vuillaume, T. Kawai, X. Wu, H. Tachibana, T. V. Hughes, H. Sakurai, J. W. Baldwin, C. Hosch, M. P. Cava, L. Brehmer, and G. J. Ashwell, J. Am. Chem. Soc. **119**, 10455 (1997).

[22] D. R. Kanis, M. A. Ratner, and T. J. Marks, Chem. Rev. **94**, 195 (1994).

[23] A. Das and S. Ghosh, Angew. Chem. Int. Ed. **53**, 2038 (2014).

[24] A. M. Sanders, T. J. Magnanelli, A. E. Bragg, and J. D. Tovar, J. Am. Chem. Soc. **138**, 3362 (2016).

[25] J. W. Leon and D. G. Whitten, J. Am. Chem. Soc. **115**, 8038 (1993).

[26] T. Kogej, D. Beljonne, F. Meyers, J. Perry, S. Marder, and J. Brédas, Chem. Phys. Lett. **298**, 1 (1998).

[27] F. Würthner and S. Yao, Angew. Chem. Int. Ed. **39**, 1978 (2000).

[28] S. Beckmann, K.-H. Etzbach, P. Krämer, K. Lukaszuk, R. Matschiner, A. J. Schmidt, P. Schuhmacher, R. Sens, G. Seybold, R. Wortmann, and F. Würthner, Adv. Mater. **11**, 536 (1999).

[29] L. R. Dalton, P. A. Sullivan, and D. H. Bale, Chem. Rev. **110**, 25 (2010).

[30] P. D. Cunningham, N. N. Valdes, F. A. Vallejo, L. M. Hayden, B. Polishak, X.-H. Zhou, J. Luo, A. K.-Y. Jen, J. C. Williams, and R. J. Twieg, J. Appl. Phys. **109**, 043505 (2011).

[31] M. Lee, H. E. Katz, C. Erben, D. M. Gill, P. Gopalan, J. D. Heber, and D. J. McGee, Science **298**, 1401 (2002).

[32] V. Parthasarathy, R. Pandey, F. Terenziani, P. K. Das, and M. Blanchard-Desce, Phys. Chem. Chem. Phys. **16**, 9096 (2014).

[33] S. Mukhopadhyay, C. Risko, S. R. Marder, and J.-L. Brédas, Chem. Sci. **3**, 3103 (2012).

[34] J. M. Hales, D. J. Hagan, E. W. V. Stryland, K. J. Schafer, A. R. Morales, K. D. Belfield, P. Pacher, O. Kwon, E. Zojer, and J. L. Brédas, J. Chem. Phys. **121**, 3152 (2004).

[35] J. L. Brédas, C. Adant, P. Tackx, A. Persoons, and B. M. Pierce, Chem. Rev. **94**, 243 (1994).

[36] D. Beljonne, W. Wenseleers, E. Zojer, Z. Shuai, H. Vogel, S. J. Pond, J. W. Perry, S. R. Marder, and J.-L. Brédas, Adv. Func. Mat. **12**, 631 (2002).

[37] W. Denk, J. Strickler, and W. Webb, Science **248**, 73 (1990).

[38] R. M. Williams, D. W. Piston, and W. W. Webb, The FASEB Journal **8**, 804 (1994).

[39] P. T. C. So, C. Y. Dong, B. R. Masters, and K. M. Berland, Annual Review of Biomedical Engineering **2**, 399 (2000).

[40] M. A. Albota, C. Xu, and W. W. Webb, Appl. Opt. **37**, 7352 (1998).

[41] M. Albota, D. Beljonne, J.-L. Brédas, J. E. Ehrlich, J.-Y. Fu, A. A. Heikal, S. E. Hess, T. Kogej, M. D. Levin, S. R. Marder, D. McCord-Maughon, J. W. Perry, H. Röckel, M. Rumi, G. Subramaniam, W. W. Webb, X.-L. Wu, and C. Xu, Science **281**, 1653 (1998).

[42] M. Pawlicki, H. Collins, R. Denning, and H. Anderson, Angew. Chem. Int. Ed. **48**, 3244 (2009).

[43] H. W. Lee, C. H. Heo, D. Sen, H.-O. Byun, I. H. Kwak, G. Yoon, and H. M. Kim, Anal. Chem. **86**, 10001 (2014).

[44] J. H. Strickler and W. W. Webb, Opt. Lett. **16**, 1780 (1991).

[45] C. Corredor, Z.-L. Huang, and K. Belfield, Adv. Mater. **18**, 2910 (2006).

[46] B. H. Cumpston, S. P. Ananthavel, S. Barlow, D. L. Dyer, J. E. Ehrlich, L. L. Erskine, A. A. Heikal, S. M. Kuebler, I. Y. S. Lee, D. McCord-Maughon, J. Qin, H. Rockel, M. Rumi, X.-L. Wu, S. R. Marder, and J. W. Perry, Nature **398**, 51 (1999).

[47] C. W. Spangler, J. Mater. Chem. **9**, 2013 (1999).

[48] S. Oliveira, D. Corra, L. Misoguti, C. Constantino, R. Aroca, S. Zilio, and C. Mendona, Adv. Mat. **17**, 1890 (2005).

[49] H. K. Turley, Z. Hu, D. W. Silverstein, D. A. Cooper, L. Jensen, and J. P. Camden, J. Phys. Chem. C **120**, 20936 (2016).

[50] O. Mongin, L. Porrs, M. Charlot, C. Katan, and M. Blanchard-Desce, Chem. Eur. J. **13**, 1481 (2007).

[51] L. Ventelon, L. Moreaux, J. Mertz, and M. Blanchard-Desce, Synth. Met. **127**, 17 (2002).

[52] W. Wenseleers, F. Stellacci, T. Meyer-Friedrichsen, T. Mangel, C. A. Bauer, S. J. K. Pond, S. R. Marder, and J. W. Perry, J. Phys. Chem. B **106**, 6853 (2002).

[53] K. Susumu, J. A. N. Fisher, J. Zheng, D. N. Beratan, A. G. Yodh, and M. J. Therien, J. Phys. Chem. A **115**, 5525 (2011).

[54] S. Amthor, C. Lambert, S. Dmmler, I. Fischer, and J. Schelter, J. Phys. Chem. A **110**, 5204 (2006).

[55] S. B. Noh, R. H. Kim, W. J. Kim, S. Kim, K.-S. Lee, N. S. Cho, H.-K. Shim, H. E. Pudavar, and P. N. Prasad, J. Mater. Chem. **20**, 7422 (2010).

[56] V. Schmitt, J. Fischer, and H. Detert, ISRN Org. Chem. **2011**, 589012 (2011).

[57] O. V. Przhonska, S. Webster, L. A. Padilha, H. Hu, A. D. Kachkovski, D. J. Hagan, and E. W. Van Stryland, "Two-photon absorption in near-ir conjugated molecules: Design strategy and structure–property relations," in *Advanced Fluorescence Reporters in Chemistry and Biology I: Fundamentals and Molecular Design*, edited by A. P. Demchenko (Springer Berlin Heidelberg, Berlin, Heidelberg, 2010) pp. 105–147.

[58] J. Fu, L. A. Padilha, D. J. Hagan, E. W. V. Stryland, O. V. Przhonska, M. V. Bondar, Y. L. Slominsky, and A. D. Kachkovski, J. Opt. Soc. Am. B **24**, 67 (2007).

[59] Y. Zhang, B. Kim, S. Yao, M. V. Bondar, and K. D. Belfield, Langmuir **29**, 11005 (2013).

[60] K. M. Shafeekh, S. Das, C. Sissa, and A. Painelli, J. Phys. Chem. B **117**, 8536 (2013).

[61] S. Ohira, I. Rudra, K. Schmidt, S. Barlow, S.-J. Chung, Q. Zhang, J. Matichak, S. Marder, and J.-L. Brédas, Chem. Eur. J. **14**, 11082 (2008).

[62] H. Y. Woo, B. Liu, B. Kohler, D. Korystov, A. Mikhailovsky, and G. C. Bazan, J. Am. Chem. Soc. **127**, 14721 (2005).

[63] S. J. Pond, M. Rumi, M. D. Levin, T. C. Parker, D. Beljonne, M. W. Day, J.-L. Brédas, S. R. Marder, and J. W. Perry, J. Phys. Chem. A **106**, 11470 (2002).

[64] A. Felouat, A. D'Aleo, and F. Fages, J. Org. Chem. **78**, 4446 (2013).

[65] A. D'Aléo, A. Felouat, V. Heresanu, A. Ranguis, D. Chaudanson, A. Karapetyan, M. Giorgi, and F. Fages, J. Mater. Chem. C **2**, 5208 (2014).

[66] H. Zhou, Z. Zheng, G. Xu, Z. Yu, X. Yang, L. Cheng, X. Tian, L. Kong, J. Wu, and Y. Tian, Dyes and Pigments **94**, 570 (2012).

[67] F. Terenziani, O. V. Przhonska, S. Webster, L. A. Padilha, Y. L. Slominsky, I. G. Davydenko, A. O. Gerasov, Y. P. Kovtun, M. P. Shandura, A. D. Kachkovski, D. J. Hagan, E. W. Van Stryland, and A. Painelli, J. Phys. Chem. Lett. **1**, 1800 (2010).

[68] H. Hu, O. V. Przhonska, F. Terenziani, A. Painelli, D. Fishman, T. R. Ensley, M. Reichert, S. Webster, J. L. Bricks, A. D. Kachkovski, D. J. Hagan, and E. W. Van Stryland, Phys. Chem. Chem. Phys. **15**, 7666 (2013).

[69] F. C. Spano, Annu. Rev. Phys. Chem. **57**, 217 (2006).

[70] F. C. Spano and C. Silva, Annu. Rev. Phys. Chem. **65**, 477 (2014).

[71] F. Terenziani and A. Painelli, Phys. Rev. B **68**, 165405 (2003).

[72] A. Painelli and F. Terenziani, J. Am. Chem. Soc. **125**, 5624 (2003).

[73] J. R. Lakowicz, "Principles of fluorescence spectroscopy," (Kluwer Academic/Plenum Publisher, 2006) Chap. Fluorescence Anisotropy, p. 291.

[74] D. H. Lee and A. C. Albrecht, in *Adv. Chem. Phys., LXXXIII*, edited by I. Prigogine and S. A. Rice (Wiley, New York, 1993, 1993) pp. 43–87.

[75] R. W. Boyd, in *Nonlinear Optics (Third Edition)*, edited by R. W. Boyd (Academic Press, Burlington, 2008) third edition ed., pp. 135 – 206.

[76] B. Dick, R. M. Hochstrasser, and H. P. Trommsdorff, "Nonlinear optical properties of organic molecules and crystals," (Academic Press, Orlando, FL).

[77] W. W. Parson, "Introduction," in *Modern Optical Spectroscopy* (Springer-Verlag Berlin Heidelberg, 2015) pp. XVI, 572.

[78] R. W. Terhune, P. D. Maker, and C. M. Savage, Phys. Rev. Lett. **14**, 681 (1965).

[79] K. Clays and A. Persoons, Phys. Rev. Lett. **66**, 2980 (1991).

[80] S. Cambré, J. Campo, C. Beirnaert, C. Verlackt, P. Cool, and W. Wenseleers, Nat. Nanotechnol. **10**, 248 (2015).

[81] J. Campo, A. Painelli, F. Terenziani, T. Van Regemorter, D. Beljonne, E. Goovaerts, and W. Wenseleers, J. Am. Chem. Soc. **132**, 16467 (2010).

[82] M. Göppert-Mayer, Annalen der Physik **401**, 273 (1931).

[83] M. Göppert-Mayer, Annalen der Physik **18**, 466 (2009).

[84] W. Kaiser and C. G. B. Garrett, Phys. Rev. Lett. **7**, 229 (1961).

[85] S. R. Marder, B. Kippelen, A. K. Y. Jen, and N. Peyghambarian, Nature **388**, 845 (1997).

[86] M. Pawlicki, H. Collins, R. Denning, and H. Anderson, Angew. Chem. Int. Ed. **48**, 3244 (2009).

[87] I. A. Mikhailov, K. D. Belfield, and A. E. Masunov, J. Phys. Chem. A **113**, 7080 (2009).

[88] B. Orr and J. Ward, Mol. Phys. **20**, 513 (1971).

[89] F. Terenziani, C. Katan, E. Badaeva, S. Tretiak, and M. Blanchard-Desce, Adv. Mater. **20**, 4641 (2008).

[90] J. L. Oudar and D. S. Chemla, J. Chem. Phys. **66**, 2664 (1977).

[91] R. S. Mulliken, J. Am. Chem. Soc. **74**, 811 (1952).

[92] A. Painelli, Chem. Phys. Lett. **285**, 352 (1998).

[93] A. Painelli, Chem. Phys. **245**, 185 (1999).

[94] S. R. Marder, L.-T. Cheng, B. G. Tiemann, A. C. Friedli, M. Blanchard-Desce, J. W. Perry, and J. Skindhøj, Science **263**, 511 (1994).

[95] M. Barzoukas and M. Blanchard-Desce, J. Chem. Phys. **113**, 3951 (2000).

[96] A. Painelli and F. Terenziani, J. Phys. Chem. A **104**, 11041 (2000).

[97] F. Terenziani, A. Painelli, and D. Comoretto, J. Phys. Chem. A **104**, 11049 (2000).

[98] A. Painelli and F. Terenziani, Chem. Phys. Lett. **312**, 211 (1999).

[99] E. E. Jelley, Nature **138**, 1009 (1936).

[100] L. H. Thomas, Proc Camb Philos Soc. **23**, 542 (1927).

[101] E. Fermi, Rend. Accad. Naz. Lincei **6**, 602 (1927).

[102] P. Hohenberg and W. Kohn, Phys. Rev. **136**, B864 (1964).

[103] W. Kohn and L. J. Sham, Phys. Rev. **140**, A1133 (1965).

[104] J. P. Perdew and M. Levy, Phys. Rev. B **31**, 6264 (1985).

[105] D. Rappoport, N. R. M. Crawford, F. Furche, and K. Burke, "Approximate density functionals: Which should i choose?" in *Encyclopedia of Inorganic Chemistry* (John Wiley & Sons, Ltd, 2006).

[106] D. M. Ceperley and B. J. Alder, Phys. Rev. Lett. **45**, 566 (1980).

[107] Y. Zhao and D. G. Truhlar, Acc. Chem. Res. **41**, 157 (2008).

[108] A. D. Becke, J. Chem. Phys. **98**, 5648 (1993).

[109] C. Lee, W. Yang, and R. G. Parr, Phys. Rev. B **37**, 785 (1988).

[110] J. P. Perdew, K. Burke, and M. Ernzerhof, Phys. Rev. Lett. **77**, 3865 (1996).

[111] J. P. Perdew and Y. Wang, Phys. Rev. B **46**, 12947 (1992).

[112] J. P. Perdew, J. A. Chevary, S. H. Vosko, K. A. Jackson, M. R. Pederson, D. J. Singh, and C. Fiolhais, Phys. Rev. B **46**, 6671 (1992).

[113] F. A. Hamprecht, A. J. Cohen, D. J. Tozer, and N. C. Handy, J. Chem. Phys. **109**, 6264 (1998).

[114] A. D. Boese, N. L. Doltsinis, N. C. Handy, and M. Sprik, J. Chem. Phys. **112**, 1670 (2000).

[115] Y. Zhao and D. G. Truhlar, J. Chem. Phys. **125**, 194101 (2006).

[116] Y. Zhao and D. G. Truhlar, Theor. Chem. Acc. **120**, 215 (2008).

[117] Y. Zhao and D. G. Truhlar, J. Phys. Chem. A **110**, 13126 (2006).

[118] E. Runge and E. K. U. Gross, Phys. Rev. Lett. **52**, 997 (1984).

[119] J. Ridley and M. Zerner, Theor. Chim. Acta **32**, 111 (1973).

[120] J. Ridley and M. C. Zerner, Theor. Chim. Acta **42**, 223236 (1973).

[121] A. A. Voityuk, M. C. Zerner, and N. Rsch, J. Phys. Chem. A **103**, 4553 (1999).

[122] M. R. Silva-Junior and W. Thiel, J. Chem. Theor. Comput. **6**, 1546 (2010).

[123] B. D. Pople J, "Approximate molecular orbital theory," (McGraw-Hill, NY, 1970).

[124] A. A. Voityuk, Wiley Interdisciplinary Reviews: Computational Molecular Science **3**, 515 (2013).

[125] S. Ramasesha, S. K. Pati, Z. Shuai, and J. Brédas, in *Advances in Quantum Chemistry*, Vol. 38 (Academic Press, 2000) pp. 121 – 215.

[126] J. Kanamori, Prog. Theor. Phys. **30**, 275 (1963).

[127] M. C. Gutzwiller, Phys. Rev. Lett. **10**, 159 (1963).

[128] J. Hubbard, Proc. R. Soc. Lond. A **277**, 237 (1964).

[129] J. Hubbard, Proc. R. Soc. Lond. A **276**, 238 (1963).

[130] R. G. Parr, J. Chem. Phys. **20**, 1499 (1952).

[131] E. Hückel, Z. Physik **70**, 204 (1931).

[132] E. Hückel, Z. Physik **72**, 310 (1932).

[133] R. Pariser and R. Parr, J. Chem. Phys. **21**, 466 (1953).

[134] J. A. Pople, J. Chem. Soc. Faraday Trans. **49**, 1375 (1953).

[135] K. Ohno, Theoret. Chim. Acta **2**, 219 (1964).

[136] G. Klopman, J. Am. Chem. Soc. **86**, 4550 (1964).

[137] S. R. White, Phys. Rev. Lett. **69**, 2863 (1992).

[138] S. R. White, Phys. Rev. B **48**, 10345 (1993).

Chapter 2

Study of Aggregates of Quadrupolar Chromophores[†]

2.1 Introduction

Energy transfer and energy delocalization are two very important phenomena in the definition of properties, and particularly of the spectral properties of molecular functional materials. Both these phenomena are driven by intermolecular electrostatic interactions. Energy transfer involves two different molecules, an energy-donor and an energy-acceptor. Upon excitation of the donor molecule, the energy can be transferred to a nearby acceptor, by an incoherent process [1–3]. Electrostatic interactions driven energy transfer are capable of going to quite large distances ($\sim$ 100 Å), but energy transfer requires an energy matching (resonance) between the de-excitation energy of donor from the relaxed to excited state and the absorption energy of the acceptor. On the other hand, energy delocalization occurs when electrostatic interactions are larger than the difference between the energies of nearby excited molecules, thereby giving rise to Frenkel excitons [4, 5]. Energy delocalization governs the spectral properties of molecular crystals and aggregates,

[†]Works reported in this chapter are published in: S. Sanyal, A. Painelli, S. K. Pati, F. Terenziani and C. Sissa, *Phys. Chem. Chem. Phys.*, 2016, **18**, 28198.

where intermolecular distances are comparable to or even smaller than the sum of van der Waals radii. The point dipole approximation is used as the simplest approach to model intermolecular electrostatic interaction in both energy transfer and delocalization and to explain their measurable effects. In this approximation, the probability of Förster resonance energy transfer (FRET) is proportional to the squared transition dipole moments of relevant transitions of the energy-donor and acceptor molecules, while the exciton splitting for a dimeric aggregate is proportional to the inner product of the transition dipole moments of nearby molecules [4–7]. Hence, in case of dipolar approximation, only *bright* states (i.e the optically allowed states, having a sizeable transition dipole moment from the ground state) are of relevance for both energy-transfer processes and exciton delocalization. However the dipolar approximation fails whenever intermolecular distances are comparable to or smaller than the molecular dimensions, a fairly common situation, in molecular aggregates and crystals. The involvement of *dark* (optically forbidden) states in energy transfer processes has also been widely studied [8–14].

Another usually adopted approximation amounts to neglect the molecular polarizability; assuming that the charge distribution of each molecule remains unaffected (in the ground or excited state) by the presence of other molecules nearby. Hence, it is a fairly poor approximation for largely polarizable molecules in molecular aggregates and crystals where intermolecular distances are considerably small [15, 16].

Aggregates of quadrupolar chromophores have been theoretically investigated in the host laboratory several years ago [14], suggesting quite impressive effects of the TPA spectra. In view of the large TPA cross section of quadrupolar dyes, their aggregates and more specifically their nanoparticles are worthy of a detailed study. In this work we will address two families of quadrupolar compounds, Boron-difluoride Curcumin (or BFC as we will call them hereafter) and squaraines (SQ), see Fig. 2.1. Curcumin-based materials are very interesting because of the large amount of data available for solvated dyes, crystals and organic nanoparticles (ONPs). These data allow us to do a detailed analysis, also supported by TDDFT calculations, in order to validate ESM models for aggregates of quadrupolar dyes. Squaraine dyes are extremely interesting for TPA applications in view of their huge TPA cross-section, and the study of their aggregates helps to illustrate the limitations of the standard exciton model for this class of highly polarizable dyes.

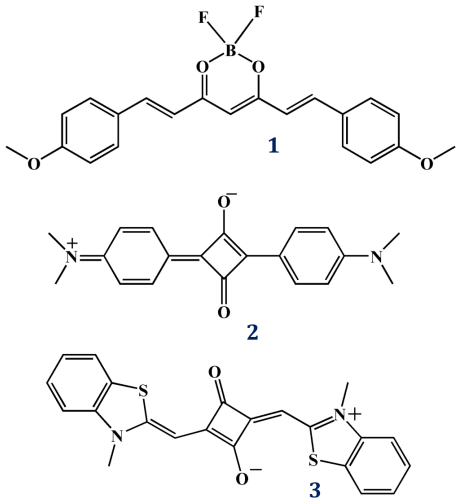

Figure 2.1: Investigated molecules (1) Boron-difluoride curcumin (BFC), (2) commercially available squaraine (SQ0) and (3) PySQ.

2.2 Computational Details

All quantum chemical calculations were carried out using Density Functional Theory (DFT), as implemented in Gaussian 09 [17] software package using the 6-31+g(d) basis set for all atoms. We confirmed the stability of the obtained geometries by ruling out the presence of any unstable vibrational modes. The ground-state geometry of the isolated BFC molecule (Fig. 2.1, molecule 1) was optimized in gas phase using B3LYP (Becke, three parameter, LeeYangParr) [18, 19] hybrid exchange and correlation energy functional, while the long-range dispersion corrected non-local energy functional, ωB97XD [20], was employed for the geometry optimizations of dimeric structures to account for dispersion corrections. The solvation effects for dichloromethane (DCM) were taken into account adopting the polarizable continuum model (PCM) [21].

Time Dependent Density Functional Theory (TDDFT) calculations were carried out using Long-Range Corrected (LRC) version of B3LYP, which is Coulomb Attenuated Method (CAM-B3LYP) [22] and 6-31+g(d) basis set for all atoms. The LRC functional was used to describe the CT states better. For BFC, TDDFT calculations were done for both gasphase and DCM solvent. We extracted two different geometries twisted (T) and planar (P) (see Fig. 2.2 and explained in Section 2.3.2)

of the dimeric structure of BFC from the crystal structure reported [23] and the spectral properties were investigated with increasing the intermolecular distance for both the geometries.

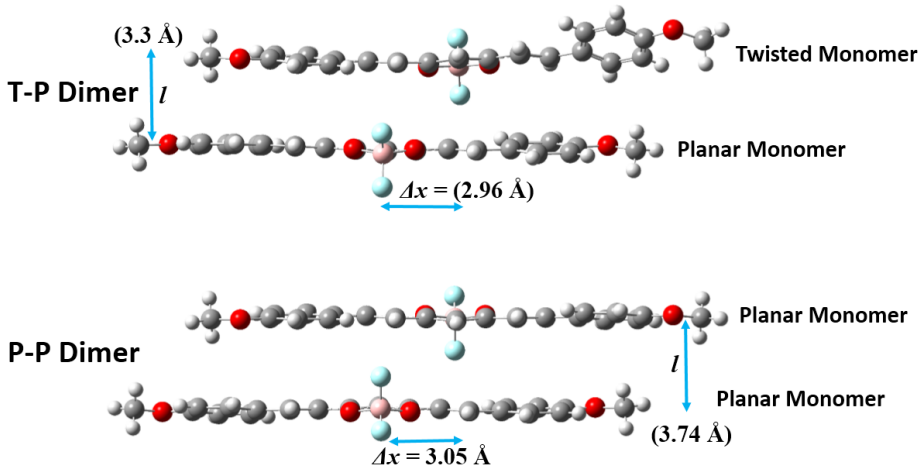

Figure 2.2: Two different dimer conformations BFC can be identified from X-ray data of crystal [Ref. [23]]: a twisted structure (T) and a planar (P) structure. In the crystal structure, a tetramer of the kind T-P-P-T can be singled out. [Grey=Carbon, White=Hydrogen, Cyan=Fluorine, Pink=Boron, Red=Oxygen]

For the linear or One-Photon Absorption (OPA), the transition intensity is expressed in terms of the oscillator strength, a dimensionless quantity, calculated for a $v \rightarrow v'$ transition as:

$$f_{osc} = \frac{2m}{e^2\hbar^2}\,(\epsilon_{v'} - \epsilon_v)|\mu_{vv'}|^2 \tag{2.1}$$

where, $\epsilon_{v'} - \epsilon_v$ is the excitation frequency from the $|0\rangle$th state v to the $|n\rangle$th state v' and $\mu_{vv'}$ denotes the electric dipole moment operator.

TPA cross-section calculations are done using the DALTON 2015 package [24] for BFC in gasphase for the monomer and dimer in gasphase, as well as for monomer in solvent. We have maintained the same level of theory as for OPA calculations within G09. The TPA intensity or δ_{TPA} for a linearly polarized monochromatic beam of light is expressed as [25–27] :

$$\delta_{TPA}(\omega) = \sum_{k,l} 2S_{kk}(\omega)S_{ll}(\omega) + 4S_{kl}(\omega)S_{kl}(\omega) \tag{2.2}$$

Here, $S(\omega)$ denotes the TPA tensor [24] and the TPA cross-section assumes a Lorentzian bandshape, and is expressed as:

$$\sigma_{TPA}(\omega) = \frac{4\pi^3 \alpha \omega^2 a_0^5}{15c\Gamma}\ \delta_{TPA}(\omega) \tag{2.3}$$

where, α, a_0 and c refer to the fine structure constant, Bohr radius and speed of light in vacuum, respectively, while Γ is the full-width half-maximum (FWHM) of the bandshape and is typically set to 0.1 eV.

2.2.1 ESM Study for Aggregates of Quadrupolar Dyes

As discussed in Ref. [14], ESMs for aggregates of CT dyes can be built easily starting from the few electronic essential states that describe a monomer (discussed in Section 1.3.1.2) and thereby constructing the basis for the aggregate as the direct product of the monomer basis states. For an aggregate of quadrupolar dyes, where 3 basis states are needed to describe a monomer, an N-molecule aggregate requires 3^N states, making it possible to do calculations on fairly large systems.

In bottom-up modeling strategy, the Hamiltonian for the aggregate is constructed as the sum of the molecular Hamiltonians. The only additional terms introduced are the electrostatic interactions among molecules (see Fig. 2.3). Along the same lines as the Mulliken approximation, only interactions among zwitterionic basis states are considered.

Here we estimate relevant interactions based on an extended dipole approximation, *i.e.*, putting a positive/negative poing charge at the location of the D^+ and A^- sites, respectively. In these conditions relevant interactions are fully defined by geometrical parameters, as described below for slipped and fan geometries (see also Figs. 2.4 and 2.5).

$$V_1 = \frac{e^2}{4\pi\epsilon_0}\ \Big(\frac{2}{\sqrt{d^2+r^2}}\ - \frac{1}{\sqrt{\Big(d+l\Big)^2+r^2}}\ - \frac{1}{\sqrt{\Big(l-d\Big)^2+r^2}}\ \Big) \tag{2.4}$$

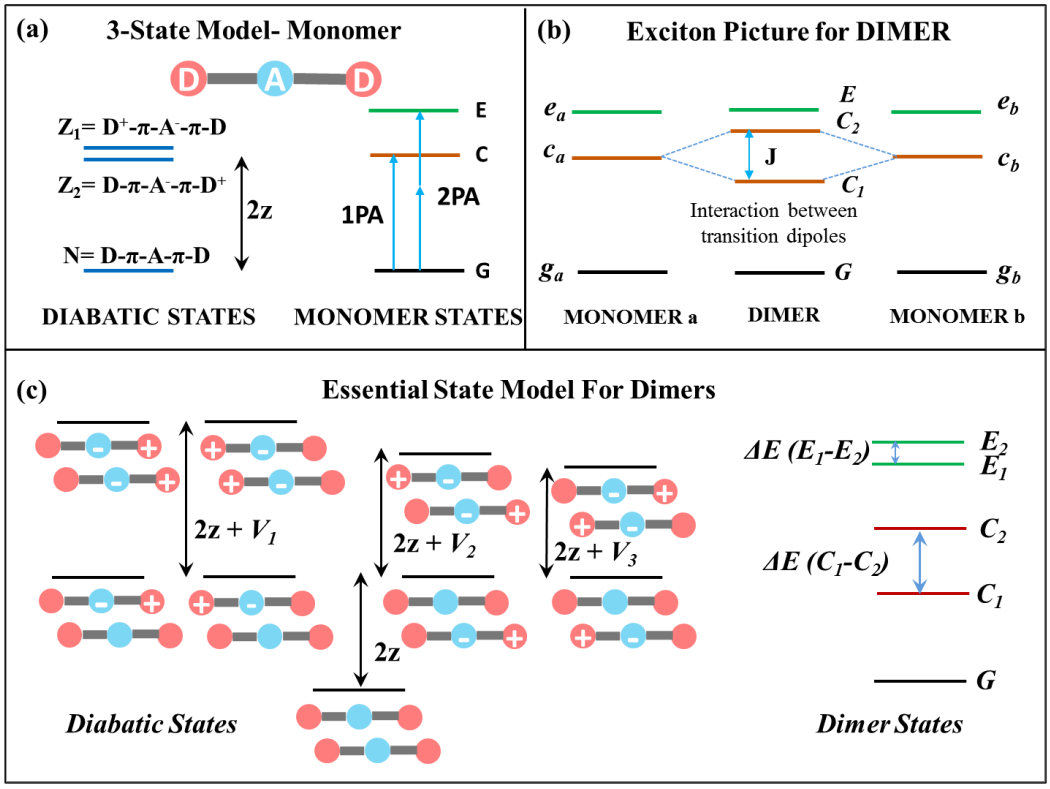

Figure 2.3: Panel (a): Sketch of Three state model for quadrupolar dye. Panel (b): Exciton picture for a dimer (made up of monomers a and b). Panel (c): ESM for a dimer. Interaction terms V_1, V_2 and V_3 for a linear dye are explained in Eqns. 2.4, 2.5 and 2.6.

$$V_2 = \frac{e^2}{4\pi\epsilon_0}\left(\frac{1}{\sqrt{d^2+r^2}} + \frac{1}{\sqrt{\left(-d+2l\right)^2+r^2}} - \frac{1}{\sqrt{\left(l-d\right)^2+r^2}}\right) \tag{2.5}$$

$$V_3 = \frac{e^2}{4\pi\epsilon_0}\left(\frac{1}{\sqrt{d^2+r^2}} + \frac{1}{\sqrt{\left(d+2l\right)^2+r^2}} - \frac{1}{\sqrt{\left(l+d\right)^2+r^2}}\right) \tag{2.6}$$

$$V_4 = V_1 \tag{2.7}$$

For the angled or "Japanese-fan type" geometry for the squaraines studied,

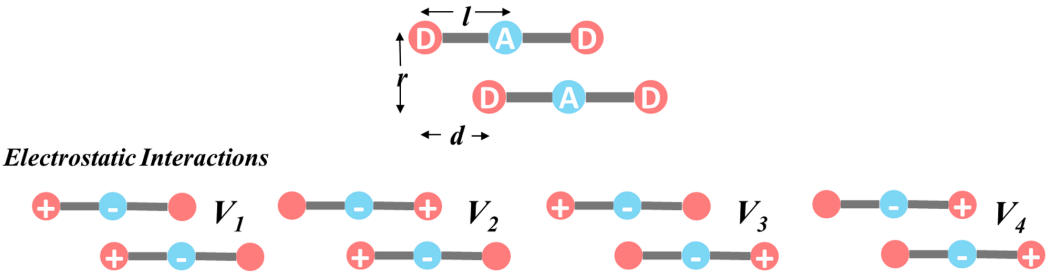

Figure 2.4: Point charge interactions in the dimer arranged in face-to-face of J-type geometry

another parameter is introduced based on the acute angle created while moving from an aligned J-type aggregation, (α) (see Fig. 2.5). The interactions are as follows:

$$V_{1fan} = \frac{e^2}{4\pi\epsilon_0}\left(\frac{1}{r} + \frac{1}{\left(r+2lcos\alpha\right)} - \frac{2}{\sqrt{\left(lsin\alpha\right)^2+\left(d+lcos\alpha\right)^2}}\right) \tag{2.8}$$

$$V_{2fan} = \frac{e^2}{4\pi\epsilon_0}\left(\frac{1}{r+2lcos\alpha} + \frac{1}{\left(r+4lcos\alpha\right)} - \frac{2}{\sqrt{\left(lsin\alpha\right)^2+\left(d+3lcos\alpha\right)^2}}\right) \tag{2.9}$$

$$\begin{aligned} V_{3fan} = \frac{e^2}{4\pi\epsilon_0}\Bigg(&\frac{1}{r+2lcos\alpha} + \frac{1}{\sqrt{\left(\left(2lsin\alpha\right)^2+\left(r+2lcos\alpha\right)^2\right)}} \\ &- \frac{1}{\sqrt{\left(\left(lsin\alpha\right)^2+\left(r+lcos\alpha\right)^2\right)}} \\ &- \frac{1}{\sqrt{\left(\left(lsin\alpha\right)^2+\left(r+3lcos\alpha\right)^2\right)}}\Bigg) \end{aligned} \tag{2.10}$$

$$V_{4fan} = V_{3fan} \tag{2.11}$$

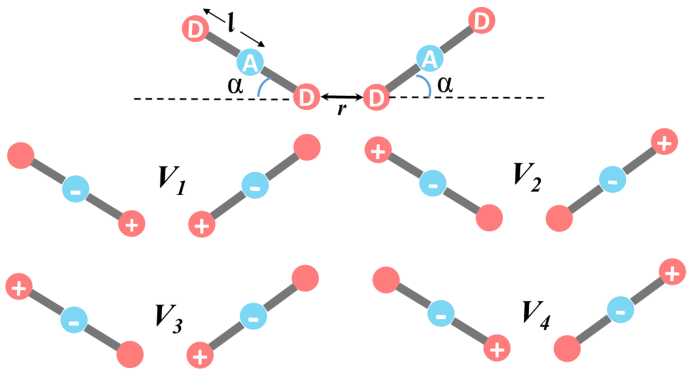

Figure 2.5: Point charge interactions in the "fan" geometry

Once the electronic Hamiltonian is set up for the aggregate, it can be diagonalized and relevant eigenstates are used to calculate spectral properties, using general expressions discussed in Chapter 1. The dipole moment operator of the aggregate is the vectorial sum of the dipole moment operators of each dye.

2.3 Curcumin Dyes and their Aggregates

Boron-difluoride curcumins (BFC) and their spectral properties have been studied by D'Aleo *et al.* [23] recently with interesting results. Curcuminoid dyes, in general, show marginal solvatochromic behaviour in absorption spectra and a marked solvatochromism in emission [28, 29], in line with the behaviour of Class I quadrupolar dyes [30]. BFC is from a family of π-conjugated chromophores containing a centrally located β-diketone unit. The presence of the central dioxaborine ring as a strong electron acceptor unit with the two electron donors as the terminal groups ends marks it as a strong TPA active chromophore [31–33]. Hence, they can be put into the category of Class I quadrupolar dyes [15] and the weak absorption solvatochromic behaviour can be attributed to the V-shaped nature of the complex [34, 35].

In case of ONPs based on BFC, OPA spectra shows a hypsochromic shift and is broadened in comparison to the spectra in solution, while in case of emission a considerable redshift is observed. Similar nature of emission spectra is also visible for crystals. There is a marginal effect on the spectral position of TPA band with a comparatively weaker enhancement in intensity for ONPs. This kind of spectral

behaviour of the aggregation for BFC dyes can be rationalized in line with the Exciton picture, also the strong suppression in fluorescence intensity is consistent with the definition of H-aggregation [23]. Furthermore, the marginal aggregation effects in TPA are consistent with the exciton picture too.

2.3.1 Modeling the isolated BFC

2.3.1.1 The ESM for BFC

As discussed in the Section 1.3.1.2, the three state electronic model for quadrupolar dyes is fully described in terms of two parameters, z and τ, which can be fixed against the experimental values for the frequency of the OPA and TPA transitions, ω_{gc} and ω_{ge}, respectively, based on expressions in Eqn. 1.23.

Experimental results in Ref. [28] has been fixed as $\hbar\omega_{gc} = 2.54$ eV and $\hbar\omega_{ge} = 3.22$ eV, leading to z=0.94 eV and τ=0.93 eV, corresponding to $\rho = 0.21$. In the following paragraphs we will not introduce any coupling with vibrational modes, so that the only additional parameters needed for the calculation of optical spectra are the dipole moment μ_0 associated with the charge-separated state (D-A^--D^+) and the intrinsic linewidth for optical transitions. These two numbers are fixed as μ_0= 20 D and $\Gamma = 0.28$ eV to reproduce the experimental intensity and linewidth of the linear absorption. A more extensive analysis also including electron-vibration coupling and polar solvation could allow us to describe in detail the solvatochromism of BFC. However, here we only use ESM as a basis to investigate aggregation effects, so we have not undertaken a complete modeling of BFCs. The exciton model leads to a reasonable picture for BFC aggregates, suggesting a moderate polarizability of the curcumin structure. However it is useful to investigate how ESM approach performs on these systems.

For future reference, we also undertook a detailed TDDFT study of BFC molecule in the gas phase and in solution. Tables 2.1 and 2.2 tabulate the main experimental and TDDFT results, respectively. In the visible range, two transitions are seen, the lowest-energy transition (at 2.54 eV in DCM) corresponds to the $|c\rangle$ state and is strongly allowed in OPA and has just a weak TPA intensity, while the second transition (3.22 eV in DCM) is assigned to the $|e\rangle$ state and is strongly TPA-allowed but with weak OPA intensity.

Table 2.1: Experimental Data from Ref. [23] for BFC in DCM.

Transitions	Transition wavelength(eV)	Molar extinction coefficient ($M^{-1}\ cm^{-1}$)	σ_{TPA} (GM)
g → c	488 nm (2.54 eV)	75480	< 10
g → e	385 nm (3.22 eV)	∼10000	155

Table 2.2: TDDFT Calculations for BFC at CAM-B3LYP/6-31+g(d)level of theory in for T and P monomer Gasphase and DCM.

System	Transitions	Transition wavelength nm (eV)	Oscillator Strength	Nature of Transitions	σ_{TPA} (GM)
Gasphase of P crystal geometry	g → c	378 nm (3.28 eV)	2.11	$h \rightarrow l$ (90%)	17
	g → e	304 nm (4.08 eV)	0.08	*h-1* $\rightarrow l$ (90%)	2030
Gasphase of T crystal geometry	g → c	372 nm (3.33 eV)	2.04	$h \rightarrow l$ (90%)	21.5
	g → e	302 nm (4.10 eV)	0.10	*h-1* $\rightarrow l$ (90%)	1950
Optimised in Gasphase	g → c	391 nm (3.17 eV)	2.15	$h \rightarrow l$ (91%)	15
	g → e	312 nm (3.98 eV)	0.07	*h-1* $\rightarrow l$ (89%)	2170
Optimised in DCM	g → c	437 nm (2.84 eV)	2.34	$h \rightarrow l$ (90%)	31.2
	g → e	335 nm (3.69 eV)	0.09	*h-1* $\rightarrow l$ (88%)	4930

Table 2.2 lists the spectral properties calculated in the gasphase for BFC dye in the two crystallographically inequivalent geometries T and P (Fig. 2.2) and its optimized geometry in gasphase and DCM solvent. In Figs. 2.6 and 2.7 the KS orbital plots and energy levels for the two inequivalent (twisted and planar) monomer units geometry, for the optimized geometry for the gasphase and solvent, the variations in the orbital structure being minimal. In all cases, in line with experimental results, the lowest transition (g → c) has a large oscillator strength, but a very weak TPA cross-section, while the second transition (g → e) is partially allowed in OPA and

shows a strong TPA activity. Note here, that the Dalton estimate of σ_{TPA} assumes a linewidth $\Gamma = 0.1$ eV as mentioned before. Hence, to account for the broader experimental linewidth the estimated σ_{TPA} value should be reduced by a factor of 3. When compared with the experiment, TDDFT transition energies are found to be over-estimated by ∼0.8 eV. As expected, TDDFT results in solvent agree better with experimental results than gas-phase results (see Table 2.2).

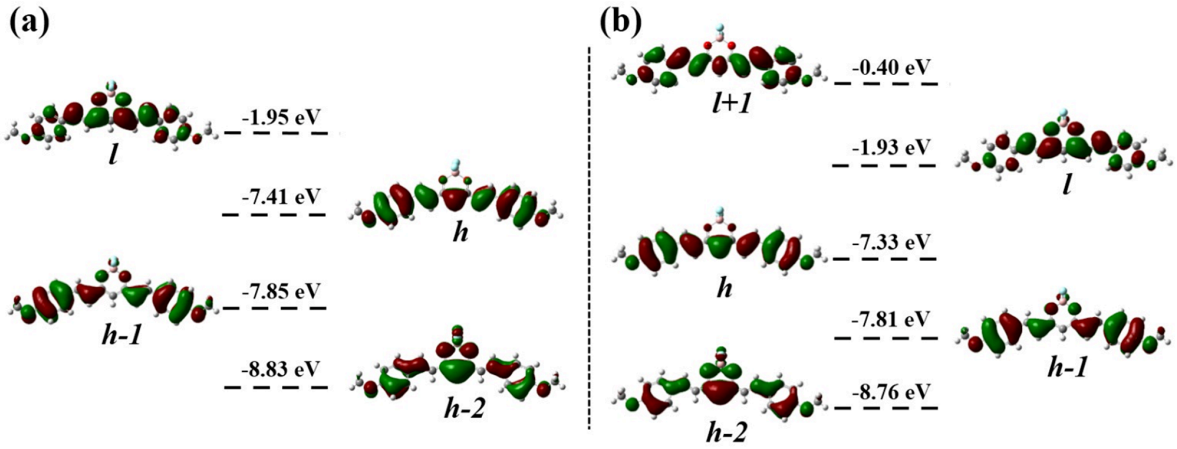

Figure 2.6: FMO plots for (a) the twisted and (b) the planar monomers (crystallographic geometry, gas phase).

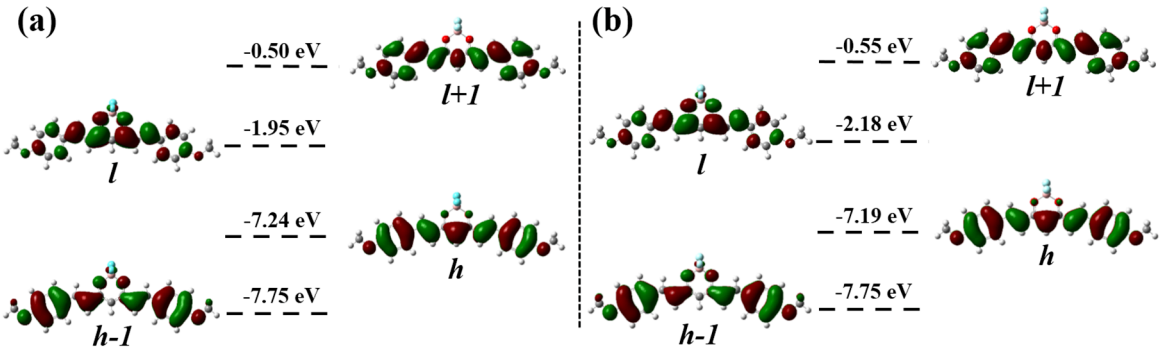

Figure 2.7: FMO plots for curcumin monomer for optimized geometry in (a) gas phase and (b) DCM solvent.

2.3.2 Modeling BFC Dimers

ESMs can be easily set up and diagonalized to describe fairly large aggregates of quadrupolar dyes, the relevant basis set increasing with 3^N, where N is the number of molecules in the aggregate. On the other hand, doing TDDFT calculations on large aggregates is has a limitation, thus to validate ESMs against TDDFT we compare in this chapter results obtained by the two methods for dimeric structures.

The reported crystal stucture of BFC in Ref. [23] highlights the existence of two monomer conformations (see Fig. 2.2), namely a planar (P) and twisted (T), and they form a tetrameric arrangement T-P-P-T (see Fig. 3.9). We performed TDDFT calculation for both T-P and P-P dimers. Further calculations were also done at some artificial geometries where the intermolecular distance (l) has been steadily increased in each step by 1 Å, upto 9 Å. In the Fig. 2.8 the relevant Kohn-Sham Frontier Molecular Orbitals (FMO) are shown for two intermolecular distances, the crystallographic geometry of 3.74 Å and an increased 6.74 Å. The transition energies for these distances are also tabulated in Table 2.3. Analogous results for the T-P dimer can be found in Appendix A.

For the sake of clarity, we have denoted the FMOs for monomer with lowercase letters h and l, referring to the HOMO and LUMO, respectively. Dimer orbitals are instead referred to with uppercase letters H or L. Here, each pair of equivalent MOs gives rise to two dimer orbitals and they are degenerate at large distances, while being weakly interactive at the crystal geometry (3.74 Å). The splitting calculated in this geometry is ∼0.2 eV. As shown in Fig. 2.8, the h→l or c transition of the monomer gives rise to four transitions in the dimer, corresponding to two local c transitions on each monomer (c_a and c_b in Fig. 2.8) and two intermolecular charge transfer or CT transitions. The two local transitions combine into the C_1 and C_2 dimer exciton states. Also, the h-1→l or e transition of each monomer gives rise to E_1 and E_2 dimer exciton states and the CT. We have mapped the main transitions for the dimers into the linear combinations of MO transitions to c_a, c_b and e_a, e_b transitions and of the CT transitions in Fig. 2.8 and Table 2.3.

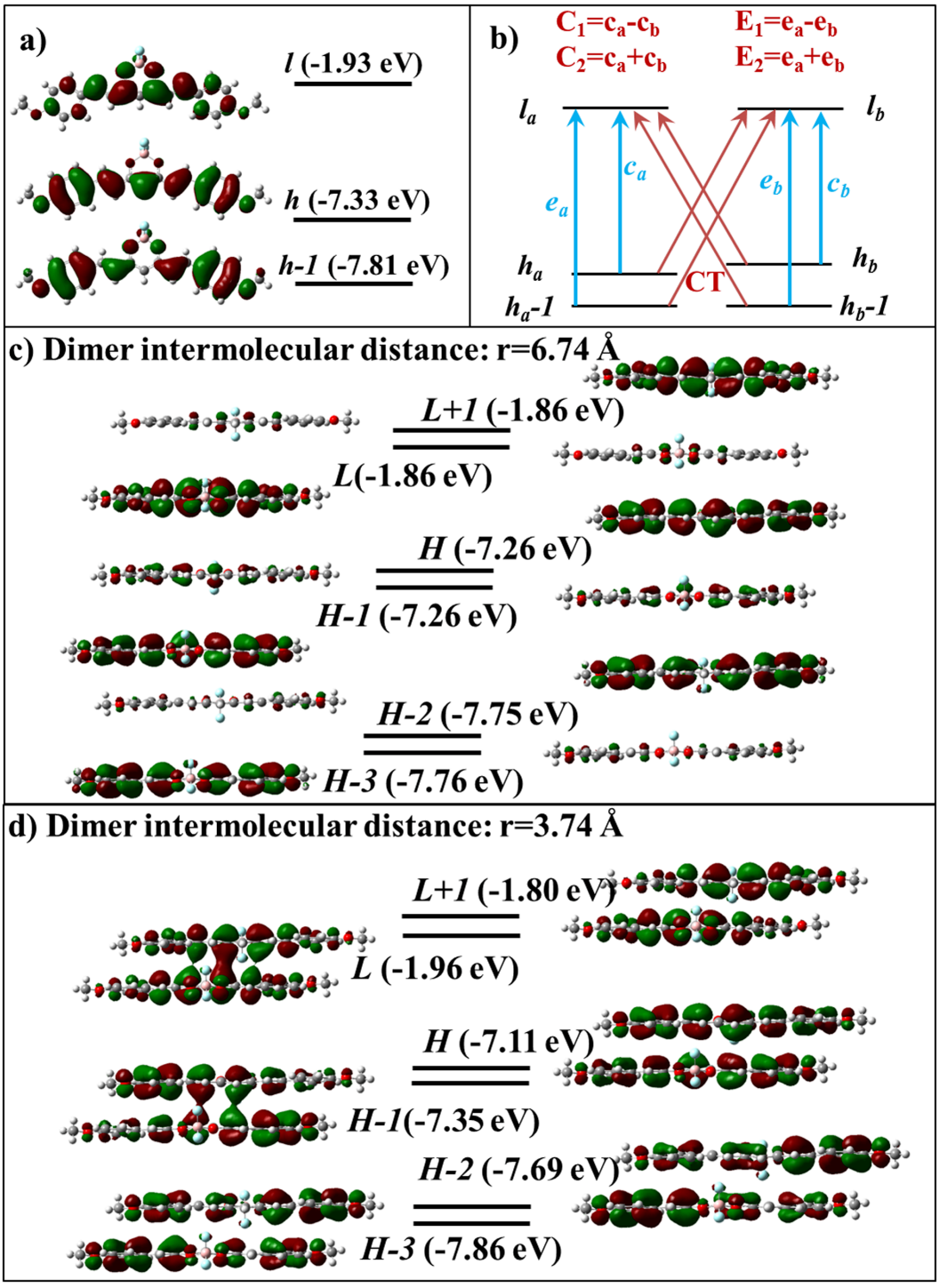

Figure 2.8: (a) FMO of BFC monomer, (b) sketch of the transitions expected for the dimer based on the monomer FMO, (c) FMO for the dimer at r = 6.74 Å, and (d) FMO of the dimer in the crystallographic geometry, at r = 3.74 Å.

Table 2.3: TDDFT Calculations for BFC P-P dimers at 3.74 and 6.74 Å in Gasphase.

Systems	Transitions	Transition Energy(eV)	Oscillator Strength	Nature of Transitions	δ_{TPA} (a.u.) (σ_{TPA}(GM))
P-P dimer at 3.74 Å	S0→S1 (C_1)	3.20 eV	0.00	H-1→L (29%) c_a H→L+1 (28%) c_b H-1→L+1 (16%) CT H→L (17%) CT	3883 (29)
	S0→S2 (C_2)	3.34 eV	4.05	H-1→L (44%) c_a H→L+1 (45%) c_b	0.41(-)
	S0→S3 (E_1)	4.04 eV	0.15	H-3→L (33%) e_a H-2→L+1 (31%) e_b	48.80(-)
	S0→S4 (E_2)	4.11 eV	0.00	H-3→L (44%) e_a H-2→L+1 (46%) e_b	2.5x10^5 (3090)
	S0→S5	4.27 eV	0.00	H→L (77%) CT	0.25 (-)
	S0→S6	4.28 eV	0.00	H-1→L+1 (78%) CT	0.24 (-)
P-P dimer at 6.74 Å	S0→S1 (C_1)	3.00 eV	0.00	H→L (72%),c_a-c_b, CT H-1→L (17%),c_a-c_b, CT	4907 (32)
	S0→S2 (C_2)	3.35 eV	3.62	H→L+1 (66%),c_a+c_b, CT H-1→L (18%),c_a+c_b, CT	0.53 (-)
	S0→S3	3.60 eV	0.34	H-1→L (74%),c_a+c_b, CT H→L+1 (18%),c_a+c_b, CT	4.69 (-)
	S0→S4	3.66 eV	0.00	H-1→L+1 (73%),c_a-c_b, CT H→L (19%),c_a-c_b, CT	1459.4 (14)
	S0→S5 (E_1)	3.94 eV	0.10	H-2→L (57%),e_a-e_b, CT H-3→L+1 (22%),e_a-e_b, CT	4.40 (-)
	S0→S6 (E_2)	4.11 eV	0.00	H-2→L+1 (52%),e_a+e_b, CT H-3→L (36%),e_a+e_b, CT	2.04x10^5 (2520)

For larger intermolecular distances, the CT contribution to low energy excitons is nominal and the first four excited states for the dimer can be safely mapped to the C_1, C_2, E_1 and E_2 states (refer to Table 2.3). At shorter distances, the energy of the CT states decrease and this makes the excitation spectrum pretty crowded. The two lowest energy states arising from the monomer c-excitations can be assigned to C_1 and C_2, while the one arising from monomer e-excitation can be assigned to E_1 and E_2. A similar analysis for varying intermolecular distances has been put in Appendix A , allowing to estimate the energies of the four excition states (see Fig. 2.9).

To compare with ESM, having already parametrized the 3-state model for the monomer in the previous section, we needed the geometrical parameters. The length of the molecular arm has been set to 6.5 Å and for the P-P dimer the lateral shift d has been fixed to 3.05 Å. The intermolecular distance (r) has been varied from 3.74 Å upto 7.74 Å, increasing by 1 Å in each step (as discussed earlier). The first four excited states of the dimer are relevant to spectroscopy, corresponding to the low and high-energy state of the exciton-splitted c-state and of the high-energy state of the exciton-splitted e-state. Relevant energies are reported in Table 2.4. Higher energy states correspond to the states where both molecules are excited and are irrelevant to spectroscopy.

The first two excited states arise from the exciton splitting of the molecular c states, the lowest energy state C_1 being dark, and the spectral intensity from the two molecules is shifted to the second excited state C_2, as happens in case of H-aggregates. The second pair of states E_1 and E_2 arise from the e molecular states. Beyond the dipolar approximation, the splitting arises due to excitonic effects, indeed both the states are dark in OPA. The TPA intensity from the molecular e state is found on E_2, while we cannot see E_1 in either OPA or TPA spectra. The C_2-C_1 and E_2-E_1 splittings both decrease with the increasing intermolecular distance (r) and the E_2-E_1 gap decreases faster than C_2-C_1. As expected, the dipolar approximation improves upon increasing r.

In Fig. 2.9 comparison has been drawn for the energies of the four exciton states as obtained from TDDFT and ESM. The absolute energy of course needs renormalization, but the r dependence of the energies and the energy gap or splittings corroborate well. Inspite of the fact that ESM is quite simple, it offers a reliable

Table 2.4: ESM results for BFC monomer and dimer. Essential-state parameters for BFC: $z = 0.94$ eV; $\tau = 0.93$ eV, $\mu_0 = 20$ D, $\Gamma = 0.28$ eV.

System	States	Transition wavelength (eV)	Oscillator Strength	δ_{TPA} (a.u.) (σ_{TPA} (GM))
Monomer	c	2.56	0.8	0
	e	3.23	0.0	4.4x10^5 (1100)
Dimer at r=3.74 Å	C_1	2.35	0.0	0
	C_2	2.79	1.6	0
	E_1	3.21	0.0	0
	E_2	3.34	0.0	2.9x10^5 (830)
Dimer at r=6.74 Å	C_1	2.48	0.0	0
	C_2	2.68	1.6	0
	E_1	3.22	0.0	0
	E_2	3.28	0.0	4.8x10^5 (1360)

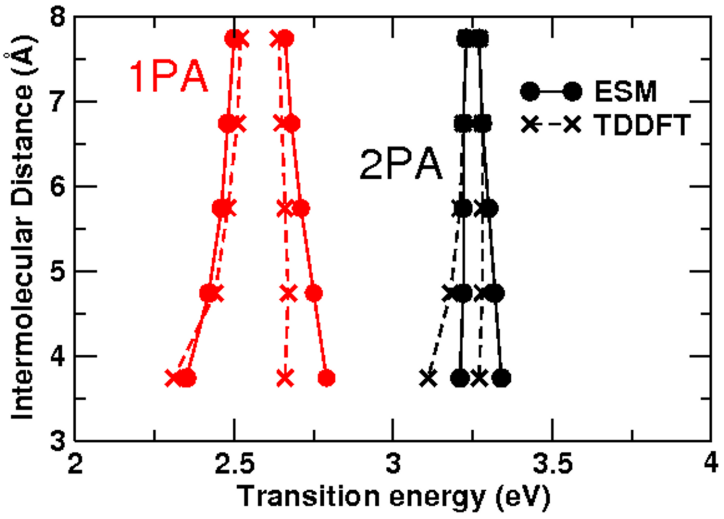

Figure 2.9: OPA (red) and TPA (black) transition energies calculated for the P-P curcumin dimer at variable intermolecular distance. ESM results (circles) are compared with TDDFT results (crosses). To facilitate the comparison, TDDFT results are rigidly downshifted by 0.83 eV for TPA and by 0.69 eV for OPA.

description of the spectroscopic effects of intermolecular interactions, both allowed as well as dark states. This suggests that though the CT states enter into play at quite close distances, their effect on the spectral properties can be neglected to a first approximation.

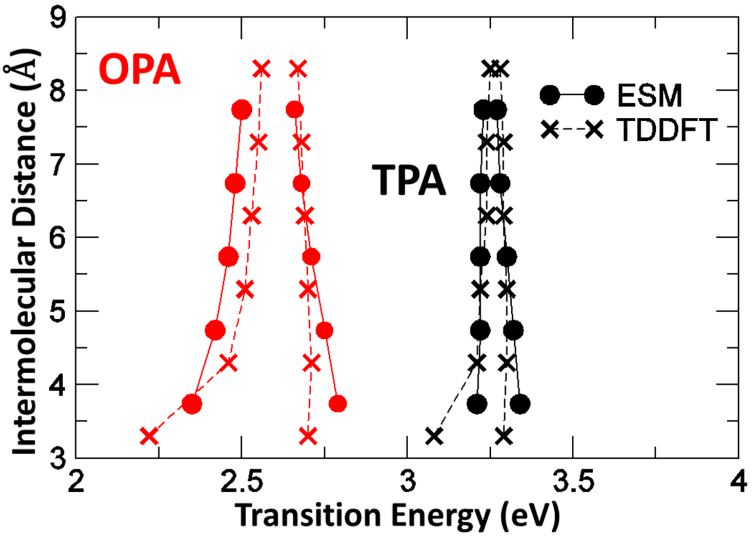

Figure 2.10: OPA (red) and TPA (black) transition energies calculated for the T-P curcumin dimer at variable intermolecular distance. ESM results (circles) are compared with TDDFT results (crosses).

On similar lines, results were obtained for the T-P dimer too (see Fig. 2.10). To facilitate the comparison in Fig. 2.10, TDDFT results are rigidly downshifted by 0.83 eV for TPA and by 0.69 eV for OPA.

2.3.3 Bigger Aggregates of BFC

After validating ESMs against TDDFT on the dimers of BFC, bigger aggregates were focussed on, which are otherwise difficult to handle with TDDFT due to the increasing number of atoms. In this section, one-dimensional arrays are considered, consisting of equivalent molecules. For the sake of simplicity, we have only accounted for nearest neighbour interactions (see Fig. 2.11). Though this presents an oversimplified view of the system, most part of the experimentally obtained results have been explained well. The experimental geometry has been modeled fixing the intermolecular distance $r = 4$ Å and the lateral shift $d = 3$ Å. The results in the

top panel of Fig. 2.11 show a marked blueshift in OPA spectra with respect to the monomer, as expected for H-aggregates. Furthermore, the presence of a dark state (marked by $\star$ in the figure) at low energy supports the suppressed fluorescence in the aggregate. In the lower panel, a comparison has been drawn for a different geometry, corresponding to a J-aggregate, and in this case the OPA spectra is redshifted with respect to the monomer, and being the lowest energy state supports the fluorescence properties for the J-aggregates.

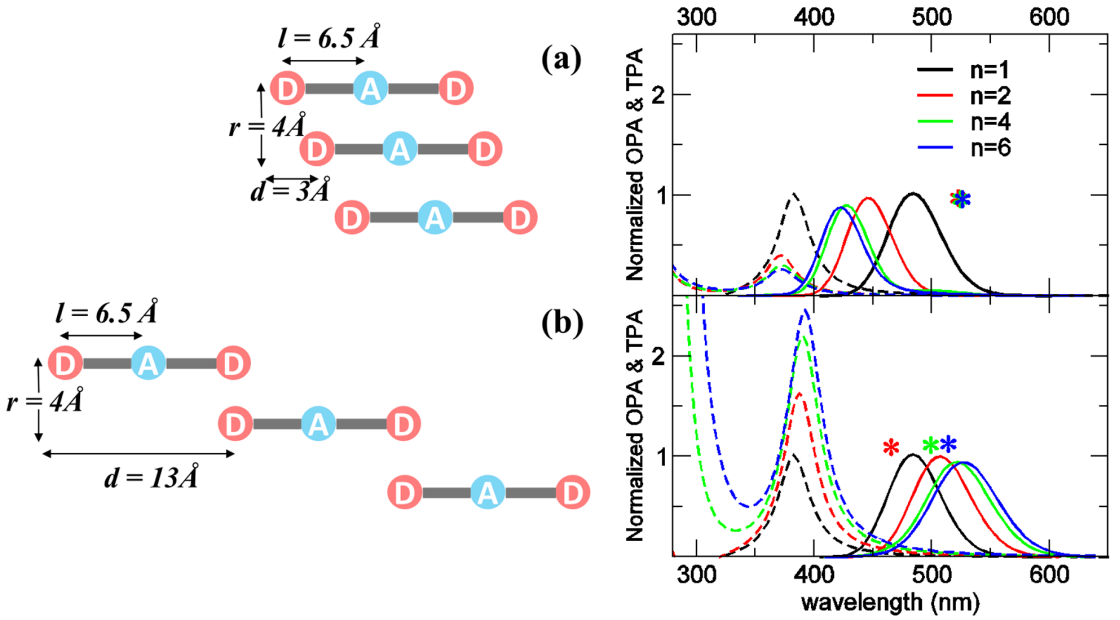

Figure 2.11: Left panel shows the sketch of geometrical arrangements of aggregates of curcumins and geometrical parameters. Right panel depicts the calculated spectra for selected geometries of BFC aggregation. n is the number of monomers. Continuous and dashed lines refer to OPA and TPA spectra, respectively. The star ($\star$) marks the position of the lowest energy dark state (C_1). In order to compare the results obtained for systems of different dimensions, OPA and TPA intensities were divided by the number of molecules.

The ESM results obtained in the top panel of Fig. 2.11 modeled on the basis of the crystallographic geometry (most probably similar geometry exists in the ONPs) predicts the H-aggregates and agrees with the experimental results too. In the experimental spectra the OPA of the ONPs are blueshifted with respect to the solvated dye and the fluorescence of both powders and nanoparticles is largely suppressed (the residual redshifted fluorescence observed in powders and nanoparticles

can be ascribed to the activation of dark state in the top panel of Fig. 2.11, due to molecular vibrations or to minor deviations from perfect alignment). The experimental TPA of ONPs is marginally affected by intermolecular interactions and the ESM predicts minor spectral shift in TPA bands, in agreement with the experiment.

2.4 Modeling Aggregates of Squaraine Dyes

Squaraines are quite popular in the field of non-linear optical applications for their large TPA cross-section [36–43]. These molecules are characterized by a large mixing of the N and Z^+ states (see Section 1.3.1.2), and they belong to the Class II quadrupolar chromophores due to their marginal solvatochromic nature both in absorption and emission spectra [30]. The OPA active state of squaraines is located at approximately half of the energy of the TPA active state, and this causes the large (pre)-amplification of the TPA intensity [40]. Due to the large mixing of the diabatic states in squaraines, they are highly polarizable and hence, large deviations from the Exciton Model is expected.

As discussed in the literature, TDDFT offers unreliable results for squaraines, mainly due to the biradicaloid character of the chromophore [44–46]. Symmetry Adapted Cluster/Configuration Interaction (SAC-CI) methods have been shown to be more reliable compared to TDDFT for this class of systems, mainly because of the fact that the charge depletion regions are localized on the central C4 or squaraic acid ring of squaraines. These studies have shown the biradicaloid character of these dyes and it has been found that the orbital interactions and the C-C-C angle in the central ring of squaraines play a dominant role in their near infrared (NIR) absorption rather than D-A-D phenomenon. Here, therefore, ESMs have been used, where though the model is oversimplified, does not suffer from the drawback of the biradicaloid nature of the central ring, unlike TDDFT. ESMs do not account for the localized excitations, including excitations involving oxyallyl ring [44], but captures the fundamentals of the low-energy transitions of this family of chromophores [30, 34, 47], thereby offering a simple strategy to account for the subtle role of molecular polarizability in aggregates.

2.4.1 *H*-Aggregates of SQ and ESM Study

In this section, we have analyzed the behaviour of squaraine dimers in controlled geometry, with reference to the experimental work in Ref. [48], carried out on squaraine dimers, in controlled geometry (see Fig. 2.12). Three different geometries have been explored, namely (a) rigid doubly bridged squaraine dimer in a face-to-face arrangement CSq_mX, (b) series of bissquaraines connected by simple polymethylene spacers SqM_nSq (n=2-10), and (c) restricted xylyl-bridged squaraines, SqX_xSq (x= o-, m-, p-).

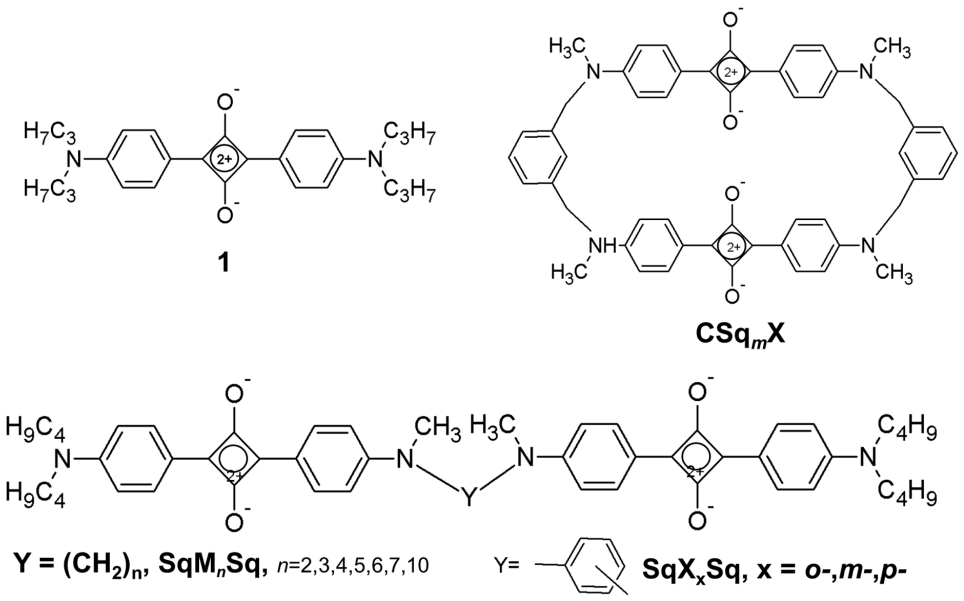

Figure 2.12: Squaraines studied as dimer aggregates in controlled geometry. [Reprinted (adapted) with permission from Liang *et al.* J. Am. Chem. Soc. 1997, 119, 830 [Ref. [48]]. Copyright (1997) American Chemical Society.]

CSq_mX shows a blueshifted band with respect to the monomer and is non-fluorescent, which is characteristic of H-aggregates. For the SqM_nSq series, two absorption bands have been observed, at the same energy as the monomer - a blueshifted band and an intense redshifted band with respect to the monomer. For n=10, however, a single band is observed as for the monomer, which shows negligible interchromophoric interactions. Also a redshift in fluorescence is observed, compared to the monomer, where the intensity gets strongly suppressed for smaller n values. Similar behaviour is also found in case of SqX_xSq.

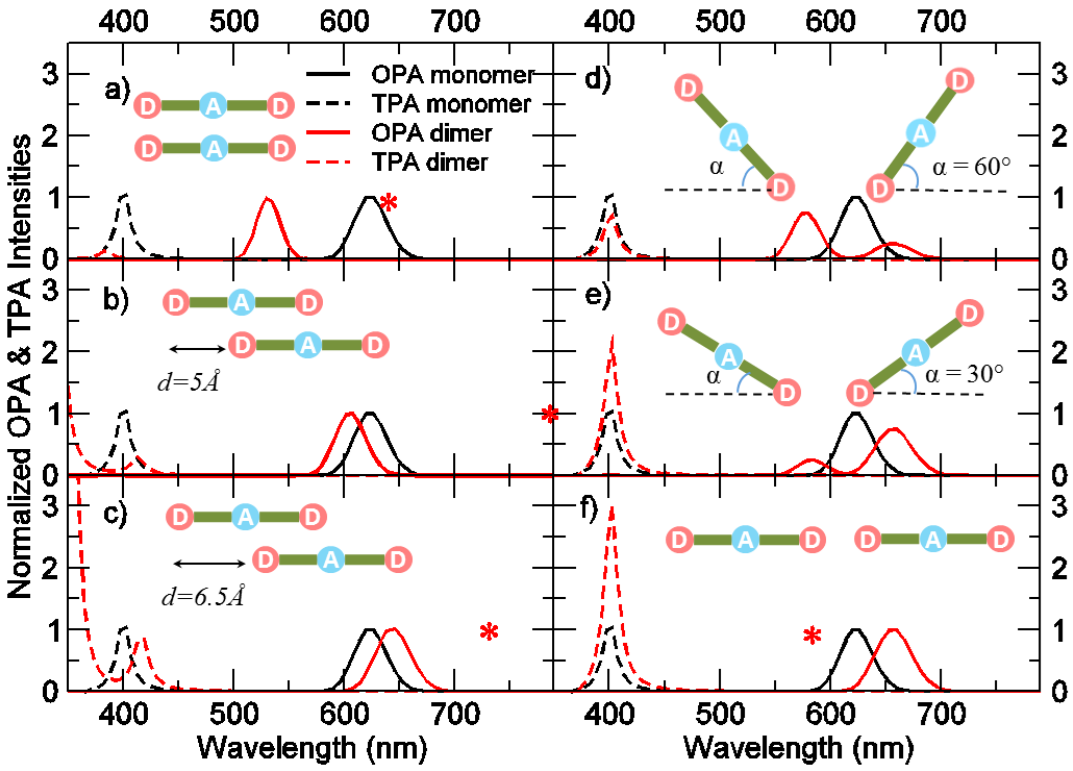

Figure 2.13: Calculated spectra for selected geometries of dimers of squaraine 1 [Ref. [48]]. The $\star$ indicates the spectral position of the lowest dark c state ($\star$ is not shown in panels d and e, since both c-states are bright). ESM parameters are: $z = 0.44$ eV and $\tau = 1.05$ eV. The length of the molecular arm is fixed to 5 Å. In left panels the distance between the two molecular axis is 5 Å. In right panels, the distance between the closest D groups is 5 Å.

This observation of an intense bathochromic shift in the OPA spectra and side by side a suppressed fluorescence for SqM_nSq as well as SqX_xSq, is difficult to rationalize from Exciton picture point of view. The Exciton model predicts a J-aggregation for bathochromic shift in the absorption spectra, with respect to the monomer, and also increased fluorescence properties. This result can be rationalized under the realm of ESMs, as shown in Figs. 2.13 and 2.14. The isolated chromophores is parameterized against experimental data, fixing $z = 0.44$ eV and $\tau = 1.05$ eV [47]. In the face to face geometry (see Fig. 2.13(a)), the OPA active state for monomer divides into a bright state to the blue and a dark to the red, explaining the complete suppression of fluorescence for CSq_mX observed in Ref. [48]. For SqM_nSq a "Japanese-fan" geometry (as was explained in the Computational

Details) has been assumed (see Fig. 2.13 (d) and (e)). In this case, both exciton states originate from *c*-state of the monomer and are OPA active, with relative intensities dependent on the angle. For $\alpha > 45°$ the blueshifted state gives rise to a more intense transition (suppression of fluorescence) and for $\alpha < 45°$ redshifted state is prominent in the OPA spectra. However, neither of these cases agree consistently with the experimental results. For a ladder type geometry (Fig. 2.13(c)), ESM anticipates an intense redshifted absorption band, simultaneously a suppression in fluorescence, with the dark state being present further to the red. Though the model does not infer the presence of a hypsochromically shifted absorption band, the experimental data has been rationalized suggesting the presence of the geometries shown in Fig. 2.13(c) and (e), and they coexist in solution.

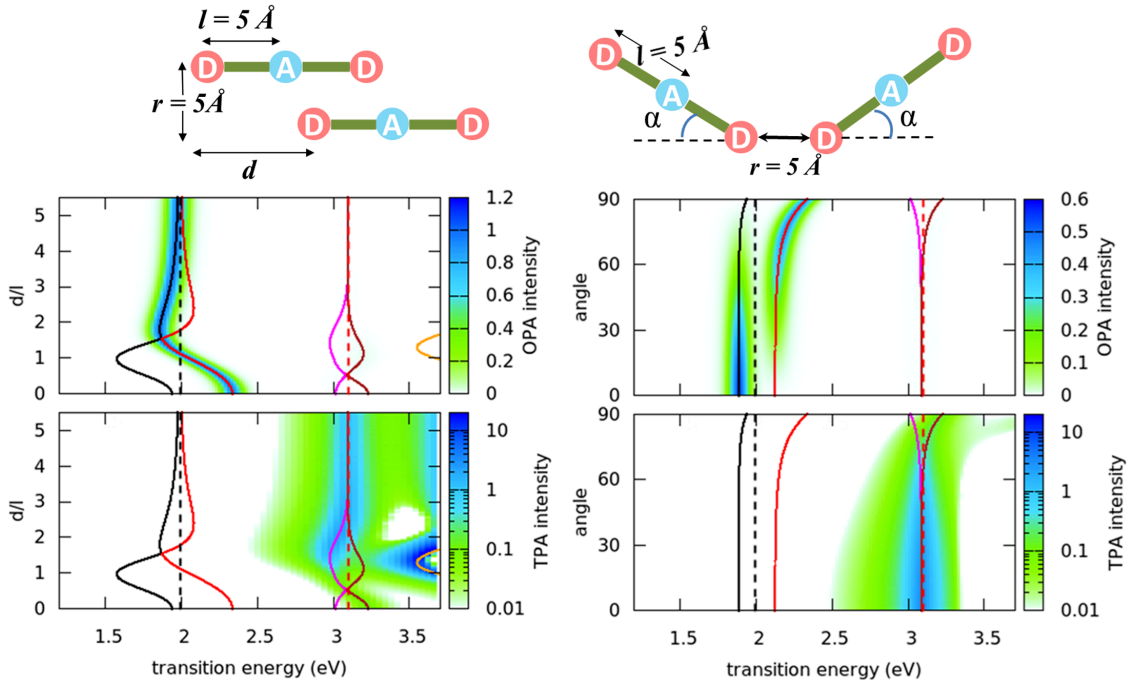

Figure 2.14: Top panel shows dimer geometries and definition of relevant parameters. Middle panels shows the color maps for OPA intensity of the dimer of dye in Ref. [48] (intensity shown per chromophore, normalized to the intensity of the monomer). Continuous lines report the transition energy of the first (black), second (red), third (magenta), *etc.* excited states. Dashed lines denote the transition energy of the first (black) and second (red) excited state of the monomer. Bottom panel shows the color maps for TPA intensity of the dimer (intensity shown per chromophore, normalized to the intensity of the monomer).

In case of the xylyl-bridged dimers of SqX_xSq, two OPA bands to the red and blue shifted regions, with respect to the monomer, are observed. They have similiar fluorescence quantum yield as the monomer. When $x = p-$, the fluorescence quantum yield is highest, and for $x = o-$ and $m-$ the factor decreases by 2.5 and 1.5, respectively. Based on the experimentally observed data, when $x = o-, m-$ and $p-$, *i.e.*, SqX_oSq, SqX_mSq and SqX_pSq geometries can be described as in Fig. 2.13(d), (e) and (f), respectively. For the *para* isomer second absorption band is dark in the calculated results, but it can gain some intensity if molecular vibrations are introduced, which has been negated here.

2.4.2 "Non-Fluorescent *J*-aggregates" Explained by ESM

Recently, Belfield and co-workers investigated another dye from the squaraine family and it's aggregates (see Fig. 2.1 molecule 3, PySQ) [38]. In the following sections we will call this dye PySQ. For the aggregates in water, a blue-shifted absorption band and strong quenching of fluorescence intensity, confirming the experimentally suggested *H*-aggregation. On the other hand, they reported the formation of *J*-aggregates of the water-soluble cationic squaraine dye (molecule 3, 4-(pyridinium-1-yl)butylbenzothiazolium squaraine), using poly(acrylic acid) sodium salt (PAA-Na) as a template. The addition of PAA-Na to the PySQ solution leads to strong redshifted absorption and fully quenched fluorescence, the phenomenon leading to "non-fluorescent *J*-aggregates".

However, from Fig. 2.15, we can see the TPA signal for the monomer and *H*-aggregate is negligible in 400-500nm region, while an intense TPA absorption ($\sim$460 GM) is observed in the presence of PAA-Na. Unfortunately, the full shape of TPA band is not experimentally accessible due to resonance effects. These two contrasting observations from Exciton picture point of view, *i.e.*, suppressed fluorescence and sizeable TPA effects, can be explained within the realm of ESM. A model for PySQ had been set up, fixing the model parameters as $z = 0.164$ eV and $\tau = 1.2$ eV. In Fig. 2.16, the OPA and TPA spectra for the ladder geometry has been shown, with a large lateral shift of 6.5 Å. As seen in Fig. 2.13(c), here too the dimer states originating from the OPA-active monomer states are red-shifted in wavelength, in comparison to the monomer, and the lowest energy state is a dark state. This anomalous behaviour is on account of the large polarizability of

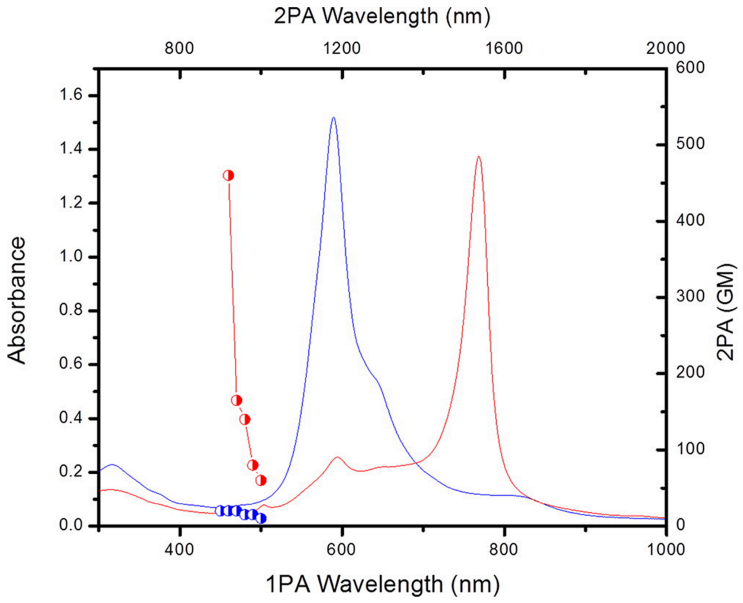

Figure 2.15: Experimental OPA spectra (in the figure as 1PA, lower x-axis and left y-axis) of PySQ, 10^{-3} M, in water (solid blue line), PAA-Na templated *J*-aggregate,10^{-4} M, (solid red line), and corresponding TPA (in the figure as 2PA) cross section (upper x-axis and right y-axis, half-filled symbols). Reprinted (adapted) with permission from Zhang *et al.* Langmuir 2013, 29, 11005. Copyright (2013) American Chemical Society.

squaraines, and due to this fact of electrostatic interactions with the neighbouring molecules, a squaraine molecule readjusts its charge distribution. This leads to the variation in transition frequency of each chromophore in the aggregate. Indeed, the aggregation system shown in Fig. 2.16 has also been studied with the mean-field approximation for a molecule experiencing the electric field generated by surrounding molecules (see Fig. 2.17) for the absorption spectrum, and a very large redshift of the absorption band with respect to the monomer, in gasphase, has been observed.

The exciton splitting with respect to mean-field absorption leads to a blue-shifted intense absorption and a red-shifted dark state, as in case of classical *H*-aggregates, even though, when compared to the isolated chromophore, both the transitions are red-shifted. In other words, the "non-Fluorescent *J*-aggregates" in Ref. 2.15 can be better explained as *H*-aggregates, with all states red-shifted due to molecular polarizability. With this model the experimental TPA data can also be explained. Indeed, from Fig. 2.16, the TPA cross-section is negligible in the 400-500 nm spectral window, for both monomer and dimer, while it increases for larger

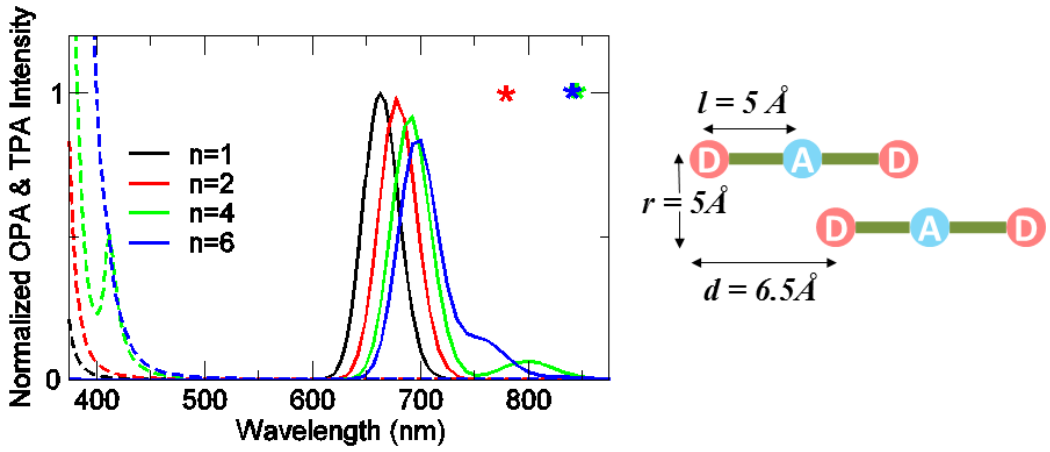

Figure 2.16: Left panel shows ESM calculation for aggregates of PySQ (parameters fixed at $z = 0.064$ eV and $\tau = 1.2$ eV). n is the number of monomers. Continuous and dashed lines refer to OPA and TPA spectra, respectively. The $\star$s refers to the lowest energy dark state. Right panel shows sketch of geometrical arrangements of aggregates and geometrical parameters

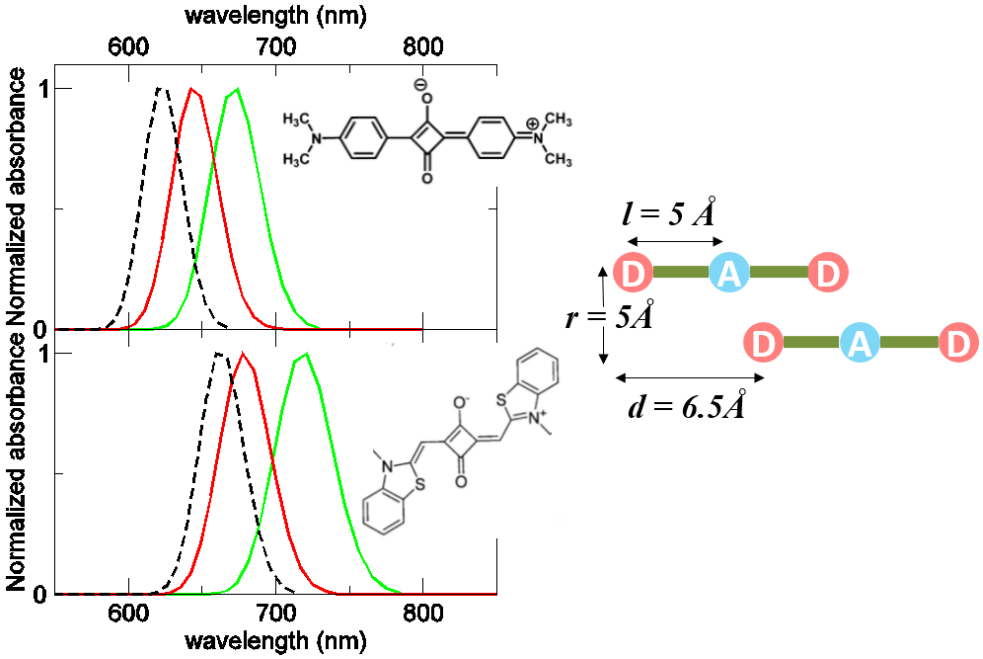

Figure 2.17: Absorption spectra of SQ dyes studied. Dashed lines refer to the monomer and continuous lines refer to dimers (intensity per molecule) in the geometrical arrangement shown on the right. Red lines refer to the ESM results and green lines show results obtained in the mean-field approximation

aggregates. In Fig. 2.18 ESM results for a brickwork arrangement in aggregates has been shown, fixing the parameters z and τ at 1.34 and 0.67 eV, respectively, for $2by2$ and $3by3$ structures.

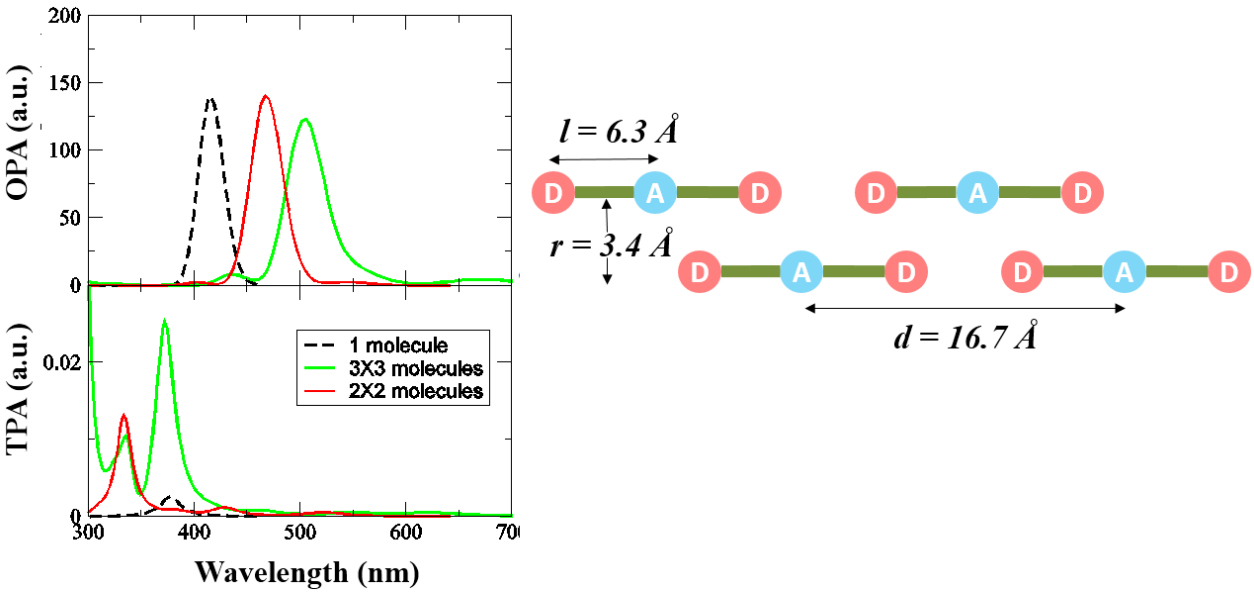

Figure 2.18: OPA and TPA calculated using ESM for a brickwork arrangement in aggregation. Red lines refer to 4 molecules formed by $2by2$ aggregation and green lines refer to 9 molecules formed by $3by3$ aggregation.

2.5 Conclusions

The elaborate analysis of experimental results on several families of quadrupolar dyes and their aggregates, supported by TDDFT calculations on dimers, laid out the possibility to reliably model and explain the properties of aggregates, accounting fully for the molecular polarizability and relaxing of the dipolar approximation. The aim of ESMs lie in this direction, thereby offering a flexible alternate pathway to Exciton Model in dealing with aggregations.

Quadrupolar dyes (D-A-D or A-D-A), are quite interesting for TPA applications and controlled aggregation phenomenon in smaller aggregates or ONPs are important for two-photon microscopy field of applications. Hence, it is quite important to understand the aggregation effects on the TPA spectra and fluorescence quantum yield (since the two-photon brilliance from microscopy point of view is defined as the

product of TPA intensity and fluorescence quantum yield). The results presented in this chapter shows, for one-dimensional aggregates, that the TPA intensity can be amplified remarkably if the dyes are set in an aligned geometry, or in a face to face geometry with increased lateral shift (the *ladder* geometry). On an interesting note along this line, the aligned geometry leads to brightly fluorescent aggregates, while for the *ladder* one a suppressed fluorescence is expected. Amplified TPA response as well as good fluorescence properties can be obtained in a 2-dimensional brickwork arrangement (shown here for $2by2$ and $3by3$) and the results are in agreement with experimental data. This kind of brickwork arrangement, however, needs more study in order to fully understand the structure-property relationship.

In this chapter, the frequent observation of "non-Fluorescent J-aggregates" has been addressed and it has been shown that it calls for explanation beyond the Exciton Model. Few recent studies have also ascribed this observation to intermolecular CT interactions [49], and this can be true for some systems; however, ESMs could rationalize this aspect even in the absence of CT interactions and predicts the reason as the molecular polarizability of squaraine dyes. For highly polarizable systems, not only does the Exciton model becomes non-applicable, but also the definition of H and J becomes ambiguous.

Bibliography

[1] J. R. Lakowicz, "Principles of fluorescence spectroscopy," (2006) Chap. Fluorescence Anisotropy, p. 291.

[2] B. Valeur, *Molecular Fluorescence: Principles and Applications* (2001).

[3] T. Renger, Photosynth Res **102**, 471 (2009).

[4] A. S. Davydov, Soviet Physics Uspekhi **7**, 145 (1964).

[5] V. M. Agranovich and M. D. Galanin, *Electronic Excitation Energy Transfer in Condensed Matter* (1982).

[6] T. Förster, Ann. Phys. **437**, 55 (1948).

[7] T. Förster, "Modern quantum chemistry," (1965) p. 93.

[8] K. Mukai, S. Abe, and H. Sumi, J. Phys. Chem. B **103**, 6096 (1999).

[9] K. F. Wong, B. Bagchi, and P. J. Rossky, J. Phys. Chem. A **108**, 5752 (2004).

[10] T. Hukka, T. Toivonen, E. Hennebicq, J.-L. Brédas, R. Janssen, and D. Beljonne, Adv. Mater. **18**, 1301 (2006).

[11] D. Beljonne, C. Curutchet, G. D. Scholes, and R. J. Silbey, J. Phys. Chem. B **113**, 6583 (2009).

[12] C. Sissa, A. K. Manna, F. Terenziani, A. Painelli, and S. K. Pati, Phys. Chem. Chem. Phys. **13**, 12734 (2011).

[13] F. Terenziani, G. D'Avino, and A. Painelli, ChemPhysChem **8**, 2433 (2007).

[14] G. D'Avino, F. Terenziani, and A. Painelli, J. Phys. Chem. B **110**, 25590 (2006).

[15] A. Painelli and F. Terenziani, J. Am. Chem. Soc. **125**, 5624 (2003).

[16] F. Terenziani and A. Painelli, Phys. Rev. B **68**, 165405 (2003).

[17] M. J. Frisch, G. W. Trucks, H. B. Schlegel, G. E. Scuseria, M. A. Robb, J. R. Ceseman, G. Scalmani, V. Barone, B. Mennucci, G. A. Petersson, H. Nakatsuji, M. Caricato, X. Li, H. P. Hratchian, A. F. Izmaylov, J. Bloino, G. Zheng, J. L. Sonnenberg, M. Hada, M. Ehara, K. Toyota, R. Fukuda, J. Hasegawa, M. Ishida, T. Nakajima, Y. Honda, O. Kitao, H. Nakai, T. Vreven, J. A. Montgomery, Jr., J. E. Peralta, F. Ogliaro, M. Bearpark, J. J. Heyd, E. Brothers, K. N. Kudin, V. N. Staroverov, R. Kobayashi, J. Normand, K. Raghavachari, A. Rendell, J. C. Burant, S. S. Iyengar, J. Tomasi, M. Cossi, N. Rega, J. M. Millam, M. Klene, J. E. Knox, J. B. Cross, V. Bakken, C. Adamo, J. Jaramillo, R. Gomperts, R. E. Stratmann, O. Yazyev, A. J. Austin, R. Cammi, C. Pomelli, J. W. Ochterski, R. L. Martin, K. Morokuma, V. G. Zakrzewski, G. A. Voth, P. Salvador, J. J. Dannenberg, S. Dapprich, A. D. Daniels, O. Farkas, J. B. Foresman, J. V. Ortiz, J. Cioslowski, and D. J. Fox, "Gaussian 09 Revision D.01," Gaussian Inc. Wallingford CT 2009.

[18] A. D. Becke, Phys. Rev. A **38**, 3098 (1988).

[19] P. J. Stephens, F. J. Devlin, C. F. Chabalowski, and M. J. Frisch, J. Phys. Chem. **98**, 11623 (1994).

[20] J.-D. Chai and M. Head-Gordon, Phys. Chem. Chem. Phys. **10**, 6615 (2008).

[21] J. Tomasi, B. Mennucci, and R. Cammi, Chem. Rev. **105**, 2999 (2005).

[22] T. Yanai, D. P. Tew, and N. C. Handy, Chem. Phys. Lett. **393**, 51 (2004).

[23] A. D'Aléo, A. Felouat, V. Heresanu, A. Ranguis, D. Chaudanson, A. Karapetyan, M. Giorgi, and F. Fages, J. Mater. Chem. C **2**, 5208 (2014).

[24] K. Aidas, C. Angeli, K. L. Bak, V. Bakken, R. Bast, L. Boman, O. Christiansen, R. Cimiraglia, S. Coriani, P. Dahle, E. K. Dalskov, U. Ekström, T. Enevoldsen, J. J. Eriksen, P. Ettenhuber, B. Fernández, L. Ferrighi, H. Fliegl, L. Frediani, K. Hald, A. Halkier, C. Hättig, H. Heiberg, T. Helgaker, A. C. Hennum, H. Hettema, E. Hjertenæs, S. Høst, I.-M. Høyvik, M. F. Iozzi, B. Jans´ik, H. J. Aa. Jensen, D. Jonsson, P. Jørgensen, J. Kauczor, S. Kirpekar, T. Kjærgaard, W. Klopper, S. Knecht, R. Kobayashi, H. Koch, J. Kongsted, A. Krapp, K. Kristensen, A. Ligabue, O. B. Lutnæs, J. I. Melo, K. V. Mikkelsen, R. H. Myhre, C. Neiss, C. B. Nielsen, P. Norman, J. Olsen, J. M. H. Olsen, A. Osted, M. J. Packer, F. Pawlowski, T. B. Pedersen, P. F. Provasi, S. Reine, Z. Rinkevicius, T. A. Ruden, K. Ruud, V. V. Rybkin, P. Sałek, C. C. M. Samson, A. S. de Merás, T. Saue, S. P. A. Sauer, B. Schimmelpfennig, K. Sneskov, A. H. Steindal, K. O. Sylvester-Hvid, P. R. Taylor, A. M. Teale, E. I. Tellgren, D. P. Tew, A. J. Thorvaldsen, L. Thøgersen, O. Vahtras, M. A. Watson, D. J. D. Wilson, M. Ziolkowski, and H. Ågren, WIREs Comput. Mol. Sci. **4**, 269 (2014).

[25] P. R. Monson and W. M. McClain, J. Chem. Phys. **53**, 29 (1970).

[26] Q. Shi, S. Kais, F. Remacle, and R. D. Levine, J. Chem. Phys. **114**, 9697 (2001).

[27] Y. Sajeev, M. Sindelka, and N. Moiseyev, J. Chem. Phys. **128**, 061101 (2008).

[28] A. Felouat, A. D'Aleo, and F. Fages, J. Org. Chem. **78**, 4446 (2013).

[29] K. Kamada, T. Namikawa, S. Senatore, C. Mattws, P.-F. Lenne, O. Maury, C. Andraud, M. Ponce-Vargas, B. LeGuennic, D. Jacquemin, P. Agbo, D. D. An, S. S. Gauny, X. Liu, R. J. Abergel, F. Fages, and A. D'Aléo, Chem. Eur. J **22**, 5219 (2016).

[30] F. Terenziani, A. Painelli, C. Katan, M. Charlot, and M. Blanchard-Desce, J. Am. Chem. Soc. **128**, 15755 (2006).

[31] G. S. He, L.-S. Tan, Q. Zng, and P. N. Prasad, Chem. Rev. **108**, 1245 (2008).

[32] F. Terenziani, C. Katan, M. Blanchard-Desce, E. Badeva, and S. Tretiak, Adv. Mater. **20**, 4641 (2008).

[33] J. M. Hales, J. Matichak, S. Barlow, S. Ohira, K. Yesudas, J.-L. Brédas, J. W. Perry, and S. R. Marder, Science **327**, 1485 (2010).

[34] C. Sissa, F. Terenziani, A. Painelli, R. B. K. Siram, and S. Patil, J. Phys. Chem. B **116**, 4959 (2012).

[35] G. Ponterini, D. Vanossi, Z. A. Krasnaya, A. S. Tatikolov, and F. Momicchioli, Phys. Chem. Chem. Phys. **13**, 9507 (2011).

[36] S. Sreejith, P. Carol, P. Chithra, and A. Ajayaghosh, J. Mater. Chem. **18**, 264 (2008).

[37] L. Beverina and P. Salice, Eur. J. Org. Chem. **2010**, 1207 (2010).

[38] Y. Zhang, B. Kim, S. Yao, M. V. Bondar, and K. D. Belfield, Langmuir **29**, 11005 (2013).

[39] H.-Y. Ahn, S. Yao, X. Wang, and K. D. Belfield, ACS Applied Materials & Interfaces **4**, 2847 (2012).

[40] J. Fu, L. A. Padilha, D. J. Hagan, E. W. V. Stryland, O. V. Przhonska, M. V. Bondar, Y. L. Slominsky, and A. D. Kachkovski, J. Opt. Soc. Am. B **24**, 67 (2007).

[41] S. Webster, J. Fu, L. A. Padilha, O. V. Przhonska, D. J. Hagan, E. W. V. Stryland, M. V. Bondar, Y. L. Slominsky, and A. D. Kachkovski, Chem. Phys. **348**, 143 (2008).

[42] D. Scherer, R. Dörfler, A. Feldner, T. Vogtmann, M. Schwoerer, U. Lawrentz, W. Grahn, and C. Lambert, Chem. Phys. **279**, 179 (2002).

[43] S. Ohira, I. Rudra, K. Schmidt, S. Barlow, S.-J. Chung, Q. Zhang, J. Matichak, S. Marder, and J.-L. Brédas, Chem. Eur. J. **14**, 11082 (2008).

[44] K. Srinivas, C. Prabhakar, C. L. Devi, K. Yesudas, K. Bhanuprakash, and V. J. Rao, J. Phys. Chem. A **111**, 3378 (2007).

[45] K. C. G, A. L. Puyad, and B. K, RSC Adv. **5**, 18813 (2015).

[46] J. Fabian, Dyes and Pigments **84**, 36 (2010).

[47] K. M. Shafeekh, S. Das, C. Sissa, and A. Painelli, J. Phys. Chem. B **117**, 8536 (2013).

[48] K. Liang, M. S. Farahat, J. Perlstein, K.-Y. Law, and D. G. Whitten, J. Am. Chem. Soc. **119**, 830 (1997).

[49] N. J. Hestand, C. Zheng, A. R. Penmetcha, B. Cona, J. A. Cody, F. C. Spano, and C. J. Collison, J. Phys. Chem. C **119**, 18964 (2015).

Chapter 3

Hyper-Rayleigh Scattering of Linear Aggregates of Dipolar Dyes: Amplified Response from Electrostatic Interactions[†]

3.1 Introduction

Donor-acceptor (DA) or "push-pull" chromophores are the simplest family of charge transfer (CT) dyes and have been investigated till date [1–8] for their promising non linear optical (NLO) responses, ensured by the presence of delocalized electrons and low-energy charge-transfer degrees of freedom. The polar nature of DA dyes makes them extremely responsive to the polarity of the environment, indeed the solvatochromism of DA dyes is well known and well understood [9], and DA dyes are quite extensively used as polarity sensors [9–12]. The standard theory for the solvatochromic response of DA dyes only accounts for their polarity and for its large variation upon photoexcitation towards a CT state, but fully disregards the molecular polarizability, neglecting the variation of the molecular polarity in response to the polarity of the local molecular environment. Essential state models (ESMs) were proposed for DA dyes 20 years back [13, 14] and were subsequently

[†] *Manuscript under preparation*

refined [15–18] as a comparatively simple yet powerful and accurate approach to fully account for the effects of molecular polarity and polarizability on spectral properties of DA dyes. Subtle spectroscopic phenomena, including the variation of the absorption and fluorescence bandshape with the solvent polarity [15–17], the progressive narrowing of fluorescence bands observed in time-resolved fluorescence experiments [19], the blue-shift of the TPA band with respect to the OPA band [20] *etc.*, were rationalized and quantitatively addressed in ESMs.

Due to their asymmetric structures, DA dyes are molecules of choice for second order (or β) NLO responses and have been quite extensively investigated in this respect [21–28]. A major issue hindering the successful development of materials for second order NLO based on DA dyes is the requirement that the asymmetry is maintained at the material level. Apart from a few notable exceptions, DA dyes organize themselves to minimize electrostatic interactions forming centrosymmetric structures. To overcome this problem different strategies have been proposed. The most popular strategy consists in loading a polymeric matrix with DA dye and then using an electric field to partly orient the molecules inside the matrix [29]. The results of this poling strategy however are not fully satisfactory, also in view of the limited temporal stability of poled samples. More sophisticated strategies imply the controlled growth of layer of DA dyes on surfaces via *e.g.* the Langmuir-Blodgett technique [30, 31], or the insertion of the dyes inside the preformed channels of specific materials [32–37]. But again the promise of DA dyes as building blocks for molecular materials for second order NLO response was not fulfilled.

When designing materials based on DA dyes most often additive behaviour was assumed [26, 29, 36], that for sure holds true for very dilute samples where intermolecular interactions are marginal. However DA dyes are polar and polarizable molecules and in dense samples quite impressive cooperative and collective effects can be driven by electrostatic intermolecular interactions, as extensively discussed in 2003 by Painelli and Terenziani [4, 38] with reference to static NLO responses. Specifically, depending on the relative orientation of the molecules, largely amplified or suppressed responses can be expected making supramolecular chemistry a powerful tool to affect the material properties. Important aggregation effects were also recognized in linear and non-linear spectral properties of dimers of DA dyes in controlled geometry [3, 21, 37, 39–43].

In this chapter, we will address a recent experimental work were p,p'-dimethylamino-nitrostilbene (DANS) molecules, a well known and widely used DA dye, were encapsulated inside single wall carbon nanotubes (SWCNT) of various diameters [36]. The electrostatic forces acting among the dyes favour a head-to-tail arrangement leading to a polar structure, important for second order NLO response. Frequency resolved Hyper-Rayleigh Scattering (HRS) spectra collected for solution samples allow to measure the β responses for the resulting structures and demonstrate a large amplification of the response that is ascribed to the presence of well ordered chains of dyes containing up to 69 molecules [36]. This large (and somewhat difficult to believe) number of aligned molecules is however estimated in the assumption of a purely additive behaviour of the β response with the number of dyes. This assumption is difficult to reconcile with the observation of a large red-shift (> 100 nm) in the linear absorption spectrum of DANS when going from a non-polar solvent (similar to the CNT environment) to the DANS encapsulated inside CNT (DANS@CNT). The absorption spectrum of DANS@CNT is indeed redshifted by ~ 50 nm with respect to that of DANS in the highly polar DMSO solvent. This simple observation points to large intermolecular interactions, that for sure affect in a complex way the NLO response of the material. Based on 2003 results from Painelli and Terenziani [4, 38], we can predict a wildly non-additive behaviour in these conditions with a large collective amplification of the β response. Accounting for this amplification of the response will definitely reduce the estimate of the number of aligned dye needed to reproduce the observed response. As we will demonstrate in the following sections, based on a combination of ESM and Density Functional Theory (DFT) results, the number of aligned molecules needed to reproduce the experimental behaviour of DANS@CNT is reduced by one order of magnitude if collective effects are accounted for, with respect to the estimate obtained in Ref. [36], obtained under the assumption of additive behaviour. In the process, we also quantitatively address some of experimental features left unaddressed in the original paper, giving us confidence in the proposed interpretation.

The work discussed in this chapter is important and had a much wider relevance that a reinterpretation of results of Ref. [36] is needed. Indeed, our work suggests to experimentalists that in order to obtain materials with huge β responses it is enough to align a modest number of DA dyes (2-10) and there is no need to go

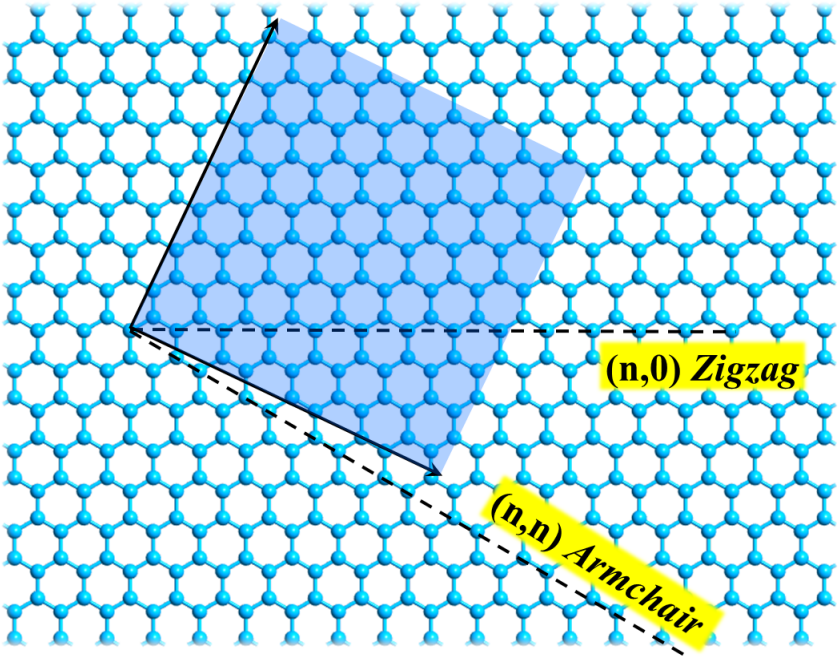

Figure 3.1: The (n, m) naming scheme in nanotubes and the figure shows how a graphene sheet should be rolled up to get the desired nanotube.

for large ordered arrays containing several tens of molecules, which would be much more difficult to obtain.

3.2 Brief Introduction to CNT and a Review of the Experiment

CNTs are an allotropic form of carbon discovered in the early years of 1950s, but they became a subject of extensive studies only in the early 1990s [44–46]. The structure of a SWCNT can be conceptualized by wrapping a one-atom-thick layer of graphene into a seamless cylinder. The way the graphene sheet is wrapped is defined by two indices (n, m); n and m indicate the number of unit vectors along two directions in the honeycomb crystal lattice of graphene (see Fig. 3.1). If $m = 0$, it indicates *zigzag* CNTs, if $n = m$, it indicates *armchair* CNTs and in general, $(n, 0)$ SWCNTs are semiconducting while (n, n) SWCNTs are metallic in nature. [45–48]

In Ref. [36], the encapsulation of DANS molecules in different SWCNT samples was convincingly demonstrated via a careful spectroscopic analysis, including Raman and fluorescence excitation maps of an extensive set of samples, including control experiments run on open and closed CNT samples. The data unambiguously demonstrate optimal encapsulation in CNT with a diameter $d \geq 1.1$ nm and marginal encapsulation for $1.02 < d < 1.08$ nm.

3.3 ESM: Bottom-up Modeling of DANS@CNT

ESMs, originally developed for solvated dyes, proved extremely useful to understand the role of intermolecular interactions in multichromophoric assemblies [3, 43, 49], aggregates [50, 51], films [31] or crystals [52]. In this respect, a bottom-up modeling strategy [2] was developed and successfully applied to different systems. The concept is very simple yet effective. In the first step, analysis of spectral properties of solvated dyes allows to build and reliably parametrize the molecular ESM model. The same model is then transferred to describe a material where several dyes interact together via electrostatic interaction, *i.e.* in the hypothesis of negligible overlap between the frontier orbitals of different molecules. In this hypothesis, the diabatic basis needed to describe the multichromophoric species is the direct product of the diabatic basis states for the isolated (or solvated) dye. The relevant Hamiltonian is the sum of the molecular Hamiltonian and intermolecular electrostatic interactions, that enter as diagonal energies on the diabatic states, and specifically affect the energies of states where more than a single species is in a zwitterionic state. Along these lines, in the following subsection, we will derive the molecular ESM for the DANS molecule, based on a careful analysis of its optical spectra. In the subsection to follow later, based on the molecular model, we will build the model for the linear aggregate.

3.3.1 Modeling DANS in solution

Experimental absorption and fluorescence spectra for DANS in different solvents are shown in Fig. 3.2 (upper panel, spectra were collected in the guest laboratory). With increasing solvent polarity from cyclohexane to DMSO both absorption and emission spectra show an important normal solvatochromic behaviour, with more

impressive effects in emission spectra (please notice that the fluorescence quantum yield of the system decreases in polar solvents, as expected based on its cubic dependence on the emission frequency, which makes it impossible to collect fluorescence spectra in the most polar solvent, DMSO). The observed solvatochromic behaviour suggests that DANS has a neutral ground state, but with a sizeable contribution from the zwitterionic state, making the molecule not just polar but strongly polarizable as well. More quantitative information is obtained by setting up a microscopic model.

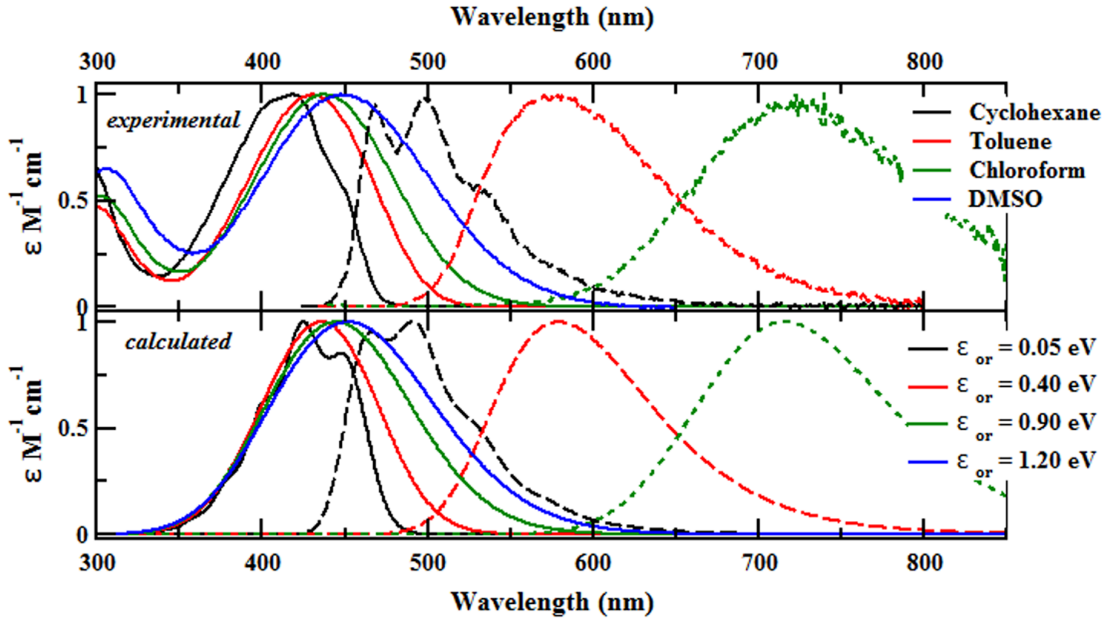

Figure 3.2: Upper panel: Normalized absorption (continuous lines) and fluorescence (dashed lines) spectra of DANS in different solvents. Lower panel: Calculated spectra using molecular model parameters in Table 3.1 and mimicking the solvent polarity effect by varying ϵ_{or} as in shown in the figure legend.

Table 3.1: ESM Parameters used for calculation of spectra (all values in eV)

z	τ	ϵ_v	ω_v	Γ
1.32	0.72	0.30	0.17	0.07

In the realm of ESM (Section 1.3.1.1), we consider only two electronic states, corresponding to the neutral and zwitterionic resonating structures of DANS, $|N\rangle =$

$|DA\rangle$ and $|Z\rangle = |D^+A^-\rangle$. As already discussed in **Chapter 1**, we also introduce the coupling to a molecular vibration q and to polar sovations, leading to the following Hamiltonian [15, 16, 53]:

$$\mathcal{H} = 2z\hat{\rho} - \tau\hat{\sigma} - \sqrt{2\epsilon_v}\omega_v\hat{q}\hat{\rho} + \frac{1}{2}\left(\omega_v^2\hat{q}^2 + \hat{p}^2\right) - F_{or}\hat{\mu} + \frac{\mu_0^2 F_{or}^2}{4\epsilon_{or}} \tag{3.1}$$

where $\hat{\rho} = |Z\rangle\langle Z|$, $\hat{\sigma} = |Z\rangle\langle N| + |N\rangle\langle Z|$, ω_v is the vibrational frequency of the effective molecular mode with coordinate q and momentum p, ϵ_v is the vibrational relaxation energy, measuring the strength of the vibrational coupling, F_{or} is the orientational component of the reaction field, $\hat{\mu} = \mu_0\hat{\rho}$ is the dipole moment operator and ϵ_{or} is the solvent relaxation energy, a parameter that increases with the solvent polarity [14].

The reaction field is associated with the very slow orientational motion of the solvent molecules around the solute. Accordingly, it is treated as a classical coordinate in the adiabatic approximation. Therefore the coupled electronic and vibrational Hamiltonian is solved on a grid of F_{or} values to get F_{or}-dependent eigenstates. The coupled electronic and vibrational Hamiltonian is solved instead in a non-adiabatic approach, where we define the non-diabatic basis as the direct product of the two electronic states and he M lowest eigenstates of the harmonic oscillator associated with q. The resulting Hamiltonian matrix is then numerically diagonalized to get numerically exact vibronic eigenstates. Of course M is chosen large enough as to reach convergence on relevant results ($M = 10$ is a typical value). Once the eigenstates are known, we use them to calculate transition energies and dipole moments as needed for the calculation of linear and non-linear spectra, as described in Section 3.3. The only additional parameter entering the equations being the intrinsic linewidth associated to each vibronic line, Γ. Once the non-adiabatic spectra are calculated on each point of the F_{or} grid, the complete spectra are finally obtained summing up results obtained for the different F_{or}, weighing each spectrum by the corresponding Boltzmann population. Of course populations are calculated based on the energy of the ground state as long as linear and non-linear absorption spectra or HRS spectra are concerned, while we use the energy of the fluorescent state to calculate the Boltzmann distribution relevant to fluorescence spectra [16, 53].

Along these lines, we were able to quantitatively reproduce the experimental absorption and fluorescence spectra and their evolution with solvent polarity, fixing

model parameters in Table 3.1. The agreement with the experiment (see Fig. 3.2) is impressive, particularly considering that only the 5 molecular parameters in Table 3.1 enter the calculation of the spectra, and that the solvent evolution is reproduced by only tuning ϵ_{or} as shown in the figure. Finally, the experimental maximum extincton coefficient ϵ =28,000 mol^{-1}cm^{-1} measured in $CHCl_3$ fixes μ_0 at 31 D.

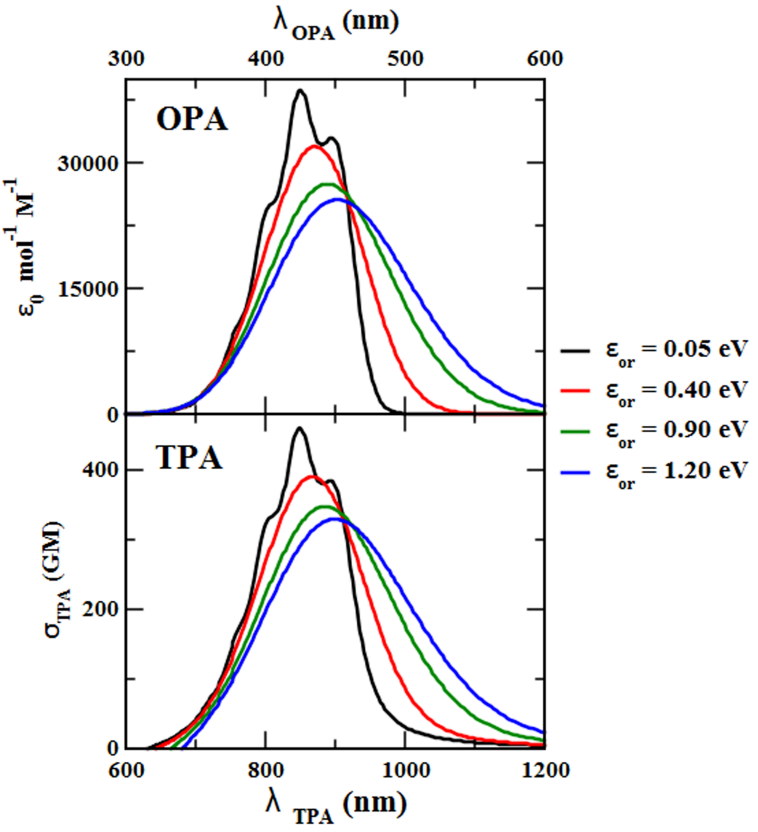

Figure 3.3: Calculated OPA and TPA spectra for DANS in different solvents, using the model parameters in Table 3.1.

With these parameters we are now in the position to calculate other spectral properties for DANS in solution. Fig. 3.3 shows calculated TPA spectra. These spectra quantitatively agree with experimental results in Ref. [54] in terms of spectral position and intensity.

HRS spectra in Fig. 3.4 are calculated with ϵ_{or}=0.9 eV as relevant to in $CHCl_3$ and to directly compare with experimental data and we have adopted the same definitions as in Ref. [36], showing the calibrated HRS signal S^{HRS}, an intensive

quantity, experimentally estimated as:

$$S^{HRS} = \frac{N_{solv}}{N_{DANS}} \left(\frac{S^{HRS}_{hybrid} - S^{HRS}_{solvent}}{S^{HRS}_{solvent}} \right) \beta^2_{solvent} \tag{3.2}$$

where S^{HRS} is given as $S^{HRS} = |\beta^2_{xxx}|$, where x is directed along the molecular D-A axis. The explicit expression for β_{xxx} can be found in Chapter 1.

Our model underestimates S^{HRS} by a factor of ~ 2, in line with the previously published results for different molecules [55]. As discussed in Ref. [55], the most probable reason behind this discrepancy may be ascribed to a systematic error in experimental results due to the calibration process for β.

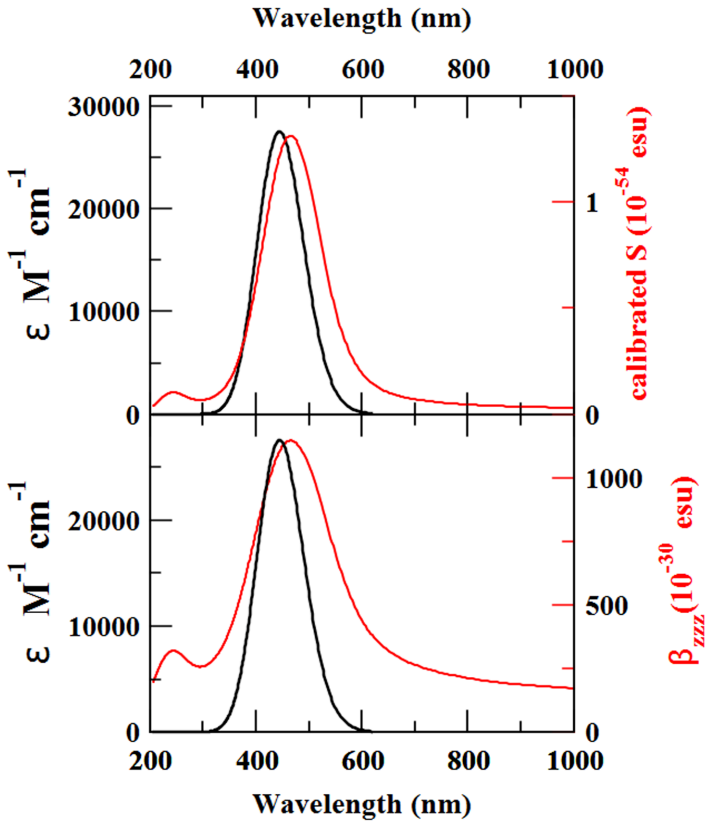

Figure 3.4: The black line in both panels shows the linear absorption spectrum calculated in $CHCl_3$ for model parameters in Table 3.1. The red lines refer to the HRS signal (scale on the right); upper panel shows the calibrated S signal,and the bottom panel shows its square root.

3.3.2 Linear Aggregates of DANS Molecules

We consider a linear chain of perfectly aligned DANS molecules, neglecting the interactions of DANS molecules and the CNT. Electrostatic intermolecular interactions are introduced only accounting for nearest neighbour interactions, so that, in the chosen diabatic electronic basis, a single parameter V enters the aggregate model, measuring the attractive interaction between two nearby dyes in the zwitterionic state. For the time being this parameter will be considered an adjustable parameter. In the next Section we will validate the estimate via quantum chemical calculations.

For each DANS molecule, the coupled electronic and vibrational Hamiltonian is defined by a basis whose dimensions are given by the number of electronic states (two for our model) multiplied by the number of states of the harmonic oscillator needed for convergence (M $\sim$10). Having neglected any intermolecular charge transfer, the number of states needed to describe a chain of N DANS molecules increases with $(2M)^N$. This makes the calculation extremely difficult for large N. However, if intermolecular interactions are large enough, we do expect delocalized excitation, and in this limit it is useful to combine the coordinates that define the coupled molecular vibrations on each site, q_i, into the corresponding linear combinations in the k-space. We are interested in optical spectroscopy, and hence we just introduce k=0 linear combination, defined as:

$$q = \frac{1}{\sqrt{N}} \sum_{i}^{N} q_i \tag{3.3}$$

This approximation makes for a huge reduction in the number of states in comparison with the complete basis, making it $2^N M$. In order to validate this approximation, we compared in Fig. 3.5 the absorption and HRS spectra for DANS dimer, calculated using both the full basis and the reduced basis. Results are shown for V = -1.35 eV, the value that we have used below to reproduce the experimental results for DANS@CNT. It turns out that the reduced basis approximation works very well already for a dimer, and it is expected to improve with increasing the chain length, as delocalization increases.

Apart from validating our approch that limits vibrational modes to the $k = 0$ mode, Fig.3.5 shows another interesting result. When moving from monomer to

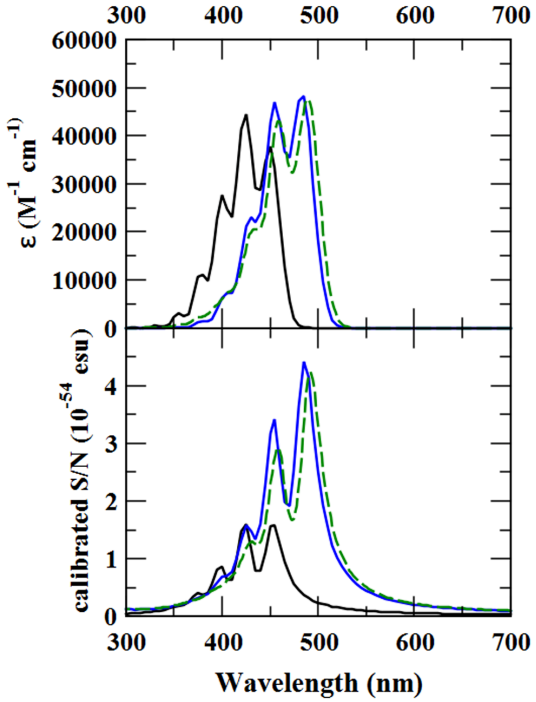

Figure 3.5: The absorption and HRS spectra calculated for an isolated DANS molecule (N=1) and a dimer (N=2), with molecular parameters in Table 3.1 and setting V = -1.35 eV for the dimer. The continuous black line refers to the monomer, the blue and green lines refer to the dimer, comparing results obtained with the reduced basis (blue) and with the complete model (green dashed).

dimer geometry, the linear absorption spectrum is red-shifted, as expected in view of the attractive intermolecular interactions, but its intensity, when reported on a per-molecule basis is marginally affected by aggregation. The calibrated S^{HRS} is by itself an intensive quantity, and in a disordered system it would be independent of the concentration or, equivalently, of the number of molecules in solution. However, as explained in detail in Ref. [36], for a linear array of *non-interacting* molecules S is expected to linearly increase with N. For this reason in Fig. 3.5 we report S^{HRS}/N, which in the hypothesis of additive behaviour should be independent of N. Results in Fig. 3.5 tell a different story, with S^{HRS}/N amplified by a factor > 2 with respect to what is expected for non-interacting aligned molecules. This result, in line with predictions in Ref. [38] obtained in the static limit, already suggests that the interpretation of experimental data in Ref. [36], relying on the hypothesis

of additive HRS response, is untenable.

While the reduced basis allows to address larger systems than the complete basis, the calculation becomes demanding for large N. However in the strong coupling regime we expect that the exciton delocalization leads to a reduction of the effective electron-vibration coupling, so that it should be possible to be progressively reducing with increasing N the number of vibrational states introduced in the calculation, without lowering the quality of the results. Fig. 3.6 shows results obtained for for linear DANS aggregates with V = -1.35 eV and increasing N. For each N two different results are compared corresponding to different number of vibrational states, showing that 8 phonon states are indeed enough to reach convergence on $N = 2$ and this number can be reduced to 4 for $N = 14$.

Results in Fig. 3.6 also tell us what happens upon increasing the aggregate size. As expected for attractive interactions, both the linear absorption and the HRS spectra shift to the red with increasing N. Moreover for both spectra the vibronic band-shape evolves with increasing N, confirming a decrease of the effective strength of electron-vibration coupling, a well-known effect owing to the exciton delocalization [56]. The extinction coefficient in Fig. 3.6 increases with N as a result of the narrowing of the absorption band, due to the reduced electron-vibration coupling effect, but the area below the absorption bands in Fig. 3.6, when properly calculated on the energy axis, stays almost constant increasing by $\sim 7\%$ from the monomer to N=14. The HRS signal instead deviates wildly from the addictive behaviour with S^{HRS}/N, that should be N independent in a linear chain of non-interacting chromophores, increasing by at least an order of magnitude when going from 1 to 12 molecules. Quite interestingly the spectral evolution with N of both absorption and HRS spectra is almost complete at N=12, suggesting that the exciton delocalizes over $\sim$ 12 molecules for the chosen $V = -1.35$ eV interactons.

The wildly superlinear dependence of S^{HRS} on the dimension of the aggregates immediately suggests that the analysis of experimental data in Ref. [36], based on the hypothesis of a linear dependence, leads to a largely overestimated number of aligned molecules in the sample. Even though Fig. 3.6 is quite informative, it cannot be directly compared with experimental results. In fact, the experimental spectra for DANS@CNT are quite broad and featureless due to the large inhomogeneous broadening owing to the presence of different CNT species. We will consider here

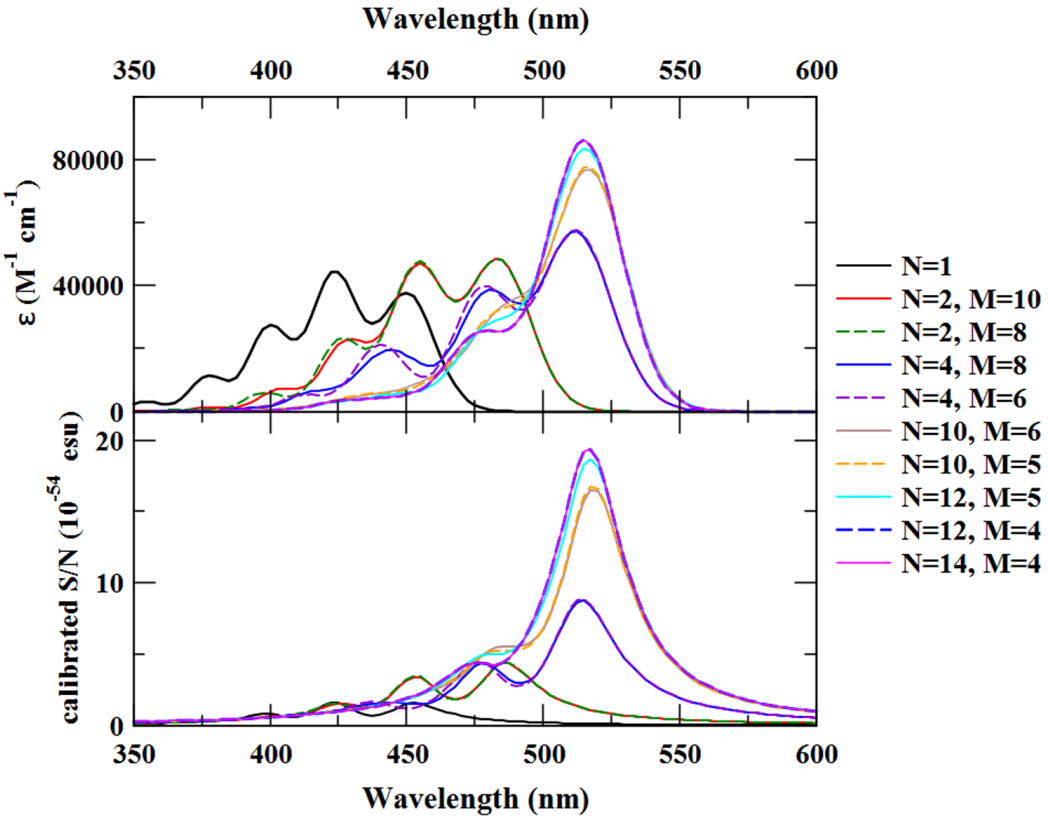

Figure 3.6: The extinction coefficient (top panel) and S^{HRS}/N (bottom panel) calculated for a linear aggregates with N aligned molecules. Results are reported for different N and varying the number of vibrational states introduced in the calculation (M) as shown in the legend.

the simplest model for inhomogeneous broadening, as a mixture of large aggregates of N molecules, each aggregate being characterized by a specific interaction V, distributed as a Gaussian centered at V_m and having a width characterized by σ_V. These two parameters are then fixed to reproduce the position and the shape of the linear absorption and HRS spectra, choosing N to reproduce the observed amplification (by a factor ∼35) of the S^{HRS} while moving from chloroform solutions to DANS@CNT [36]. We obtained the best results in Fig. 3.7 for an aggregate of 7 molecules (having V_m = -1.35 eV and σ = 0.27 and 0.30 eV for the two samples, DANS@oARC and DANS@oHiPco discussed in Ref. [36]).

Fig. 3.7 compares well with experimental data, with the linear absorption band centered at ∼500 nm and the HRS peak displaced to ∼520 nm. The red-shift

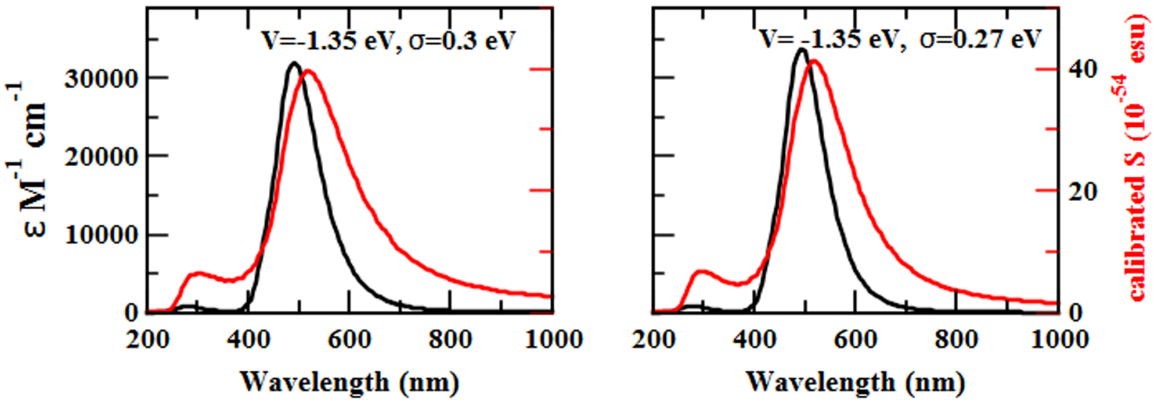

Figure 3.7: Extinction coefficient (black) and S^{HRS} (red), for 7 aligned molecules having V_m = -1.35 eV. Left panel results are obtained assuming a Gaussian distribution around V_m with σ = 0.3 eV and the right panel results are obtained for σ = 0.27 eV. To enable the comparison with experimental data in Ref. [36] the ratios of the scales for calibrated S in this figure and in Fig. 3.4, relevant to the solvated dye, are fixed to the same value.

of 20 nm of the HRS signal with respect to the linear absorption was correctly ascribed in Ref. [36] to inhomogeneous broadening, but the authors were not able to reproduce it, and were forced to introduce *ad hoc* a rigid shift of the spectra. On the contrary, this shift is quite naturally and quantitavely reproduced in our calculation, giving further confidence on the proposed model and to our estimate that $\sim$ 7 aligned molecules are responsible for the observed amplification of the HRS signal of DANS@CNT.

3.4 Validating the ESM model for DANS Aggregates

The bottom-up modeling of DANS aggregates proposed above is fairly convincing as it leads to a coherent and very accurate description of spectral properties of solvated DANS as well as of DANS@CNT. Molecular model parameters are validated extensively against experiment, indeed they reproduce linear and two-photon absorption as well as fluorescence spectra of DANS dissolved in different solvents, as well as HRS spectra of DANS in $CHCl_3$. However, the adopted value for the intermolecular interaction $V \sim$ -1.35 eV need to be validated. In the following we

will discuss an extensive series of DFT calculations towards the validation of the intermolecular interaction model.

3.4.1 Computational Details

First-principles calculations using spin-unrestricted and restricted DFT are carried out, with BeckeLeeYangParr (BLYP) GGA [57, 58] exchange-correlation functional along with Grimme′s DFT-D2 dispersion correction, as implemented in the QUICKSTEP [59] module of the CP2K package[60]. Norm-conserving Goedecker-Teter-Hutter (GTH) [61–63] pseudopotentials have been used, which have been optimized in the CP2K package for using along with the BLYP functional. CP2K uses a hybrid Gaussian and plane-wave method for the electronic representation of the structure. We have expanded Kohn-Sham valence orbitals using double-ζ valence polarized basis sets that are optimized for the GTH pseudopotentials (DZVP-MOLOPT-GTH). Together with the NN50 smoothing method, a 480 Ry density cutoff for the auxiliary basis set of plane waves has been used. The generalized gradient approximation (GGA) [57] in the PerdewBurkeErnzerhof (PBE) form and double zeta polarized (DZP) basis set have been chosen for the spin-polarized DFT calculations. Gas phase geometry optimizations of the composite systems (DANS@CNT)have been performed using BFGS method, and systems are optimized until the force on each atom is <0.0001 Hartree/Bohr. The coordinates of the CNT are kept frozen (CNTs are built using nanotube builder integrated inside VMD [64]), while the DANS molecules are made to relax to their equilibrium geometries.

3.4.2 Geometry Analysis

To model the experimental system reported in Ref. [36], we have chosen various CNTs, of differing chirality and diameters, to encapsulate a linear arrangement of DANS molecules. The choice of CNT is guided by the experimental observation that the optimized diameter reported in experiment is $d \geq 1.02$ nm, otherwise the DANS molecules are not encapsulated. In our list of CNTs, we have only one, *i.e.*, CNT(10,0) which has diameter below that of the threshold limit. To have information about the aggregate structure we put two DANS molecule inside each

nanotube, and in order to ensure the interaction between the the $DANS_2$@CNT composite system with the adjacent supercell is negligible, a lateral separation of 10 Å in x and y direction is maintained. The optimized geometry of each $DANS_2$@CNT composite system is shown in Fig. 3.8.

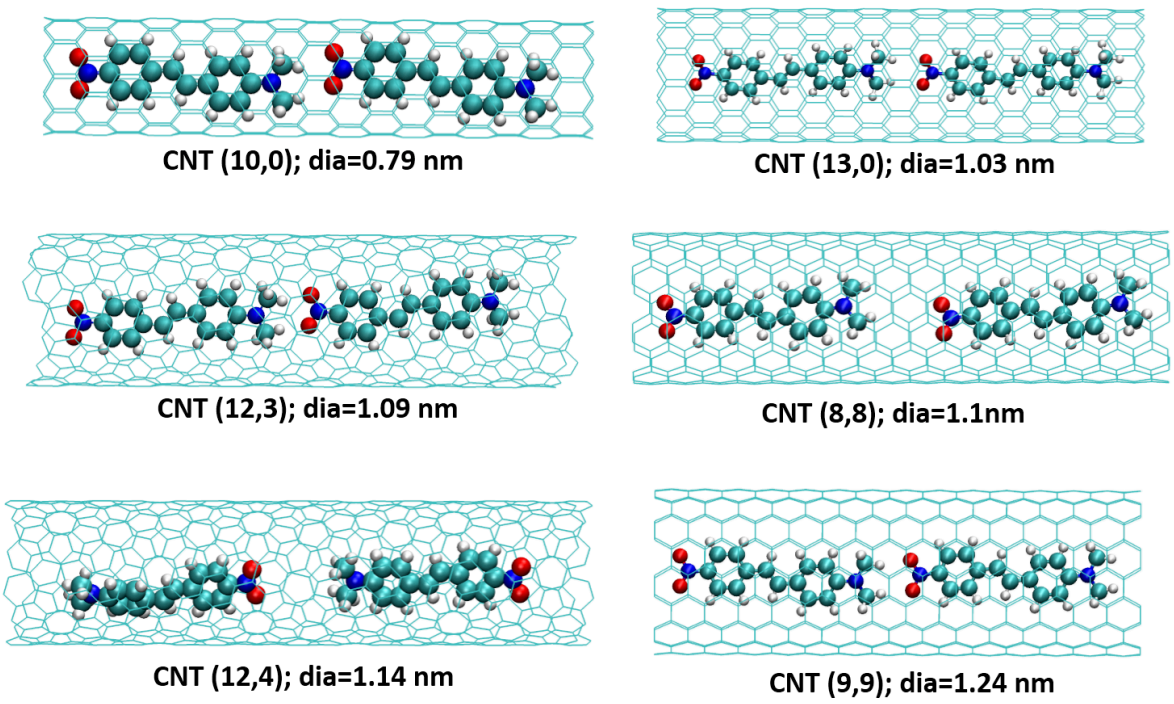

Figure 3.8: Optimized geometries of the DANS dimer inside CNTs of different chirality and diameter (dia in figure). [Colour code: Cyan = Carbon, Red = Oxygen, Blue = Nitrogen, Grey = Hydrogen]

In case of CNT(8,8), the monomers are non-coplanar, unlike in the other CNTs. Whereas, in case of CNT(12,4) one of the DANS molecules is planar in conformation, while the other takes a twisted form after optimization. In Table 3.2, for each investigated structure we collect geometrical information showing the intramolecular N-N distance, (*i.e.*, the distance between nitro N and dimethyl amino N in the same molecule) roughly corresponding to the D-A length in the ESM; and intermolecular N-N distance, *i.e.* the distance between nitro N and dimethyl amino N in adjacent molecules. Results are ordered in terms of increasing CNT-diameter. We notice that for some CNT the two DANS molecules have a slightly inequivalent

structure and for this reason two different values of the intramolecular N-N distances are given. A fairly wide variation of the intermolecular distances is observed for different CNTs, ranging from 4.7 to 8.5 Å, suggesting a sizable dispersion of intermolecular interactions.

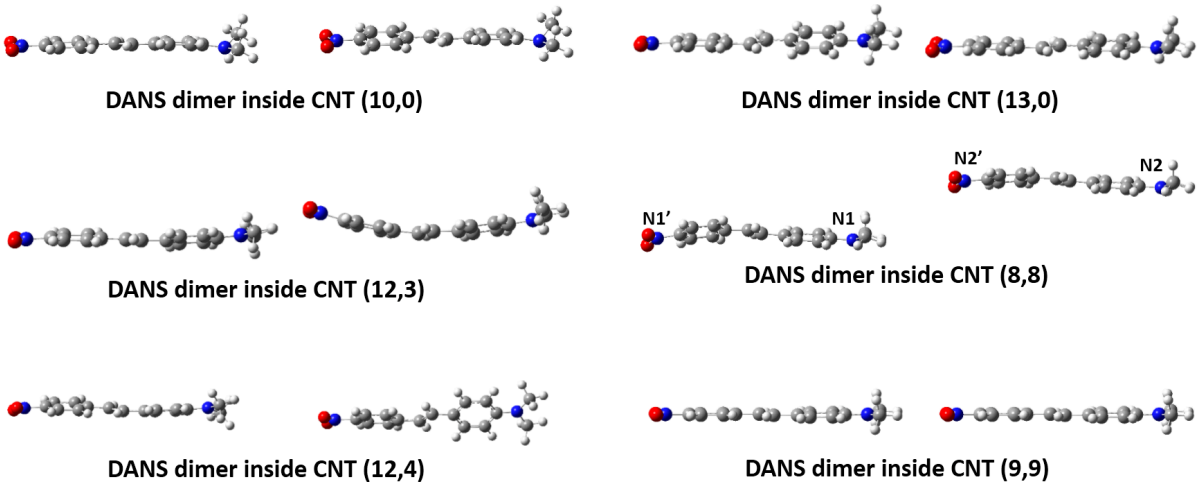

Figure 3.9: Optimized geometries of only the DANS dimer as inside CNTs of different chirality and diameter, the same as in Fig. 3.8 but with the CNT structure removed for clarity. [Colour code: Grey = Carbon, Red = Oxygen, Blue = Nitrogen, White = Hydrogen]

Table 3.2: Intra and Intermolecular N-N distances, for the $DANS_2$@CNT in Fig. 3.9, CNT diameters and interactions calculated in the extended dipole approximation (V_{ed})

CNT Type	Diameter (nm)	Intra N-N (Å)	Inter N-N (Å)	V_{ed} (eV)
CNT(10,0)	0.79	12.36 12.35	4.72	-1.85
CNT(13,0)	1.03	12.34	5.41	-1.52
CNT(12,3)	1.09	12.20 12.30	4.71	-1.85
CNT(8,8)	1.10	12.31 12.27	8.01	-0.82
CNT(12,4)	1.14	12.77 12.26	8.54	-0.75
CNT(9,9)	1.24	12.30	4.72	-2.14

The geometrical parameters in Table 3.2 allows a first estimate of V, the electrostatic interaction between two nearby molecules in the zwitterionic state, as

entering the ESM for the DANS aggregate. D site being located on the N atom of the dimethyl amino group and the A site on the N atom of the nitro group, the DANS dimer can be described in the ESM according to Fig. 3.10. l is set as the molecular length *i.e.* intramolecular N-N distance and d is the the intermolecular N-N distance. The interactions between two zwitterions are then easily calculated in the extended dipole approximation [65, 66] as the sum of two (equal) repulsive interactions (1 and 2 in the figure) *minus* two attractive interactions (3 and 4) as:

$$V_{pd} = \frac{e^2}{4\pi\epsilon_0}\left(\frac{2}{l+d} - \frac{1}{d} + \frac{1}{2l+d}\right) \tag{3.4}$$

Results are reported in the fifth column of Table 3.2. When two inequivalent molecules are present we take the molecular length l as the average of the two values. Calculated results show a wide variability for the different CNT, in line with the large variability of the intermolecular distances. The obtained values are of course negative, corresponding to attractive intermolecular interactions and lie between -0.75 eV and -2.14 eV, suggesting that the effective average value $V = -1.35$ eV, extracted above (from the analysis of spectroscopic data) is a reasonable choice.

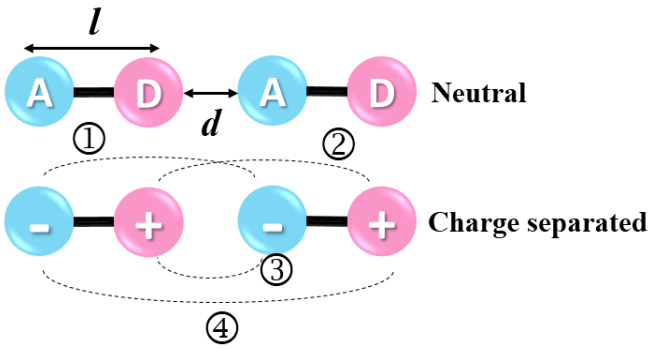

Figure 3.10: Interaction terms for intermolecular interactions in the extended dipole approximation.

3.4.3 Intermolecular Interactions: A More Detailed Picture

The extended dipole approximation for intermolecular interactions, though successful, is based on an oversimplified description of the charge distribution on the

zwitterionic DANS molecule. A more accurate estimation can be obtained based on a strategy first proposed in Ref. [52]. Specifically, if the charge distribution is known in the zwitterionic and neutral molecule in terms of atomic charges, V can be estimated as $V = V_Z - V_N$ where V_Z (V_N) is the electrostatic interaction between two zwitterionic (neutral) nolecules, calculated as sum of the interactions between atomic charges. The atomic charges in the neutral structure can be easily evaluated from a gas phase calculation, but to estimate the charges on the zwitterionic structure we must force DANS to be in a zwitterionic state. As in Ref. [52], we apply an electric field to the molecule to favour charge separation, but, at variance with Ref. [52] where we were working on a radical DA species, DANS is a closed shell system, and this makes the calculation complex.

For a DA dye we expect that the ground state dipole moment μ changes fairly abruptly from a low value typical of the neutral state to a large value, typical of the zwitterionic state. Indeed for the radical species investigated in Ref. [52], the two plateau in the $\mu(E)$ curve allowed to recognize clearly the neutral and zwitterionc regimes. Result for DANS as shown in Fig. 3.11 are somewhat not the obvious ones. In this figure we report results obtained for a DANS molecule (specifically in the geometry calculated inside the CNT(13,0), but similar results are obtained for other geometries as well), under an applied electric field directed along the axis joining the two N atoms in the molecule. The figure shows the dependence of the ground state dipole moment (more precisely of its component along the applied field) μ_x vs the field.

Quite irrespective of the level of theory the obtained μ_x does not show any sign of two distinct plateau corresponding to the two neutral and zwitterionic states. Following Geskin *et al.* [67], we have carried out several calculations using BS-UHF (Broken-Shell Unrestricted Hartree-Fock), PO-UHF (permuted-orbital unrestricted Hartree-Fock, occupied and unoccupied orbitals permuted for one spin), Restricted Hartree-Fock (RHF), long range coulomb attenuated functional (CAMB3LYP), CIS (keyword requesting a calculation on excited states using single-excitation Configuration Interaction), ROHF (Restricted Open-shell Hartree-Fock, for open-shell ground state), along with the semi-emperical ZINDO/S methods for singlet DANS molecule(13,0). However, we failed to get an expected one-step nature for one-electron transfer with the application of external electric field. Fig. 3.11 shows the

results for a selected model, at a few of these levels of theory.

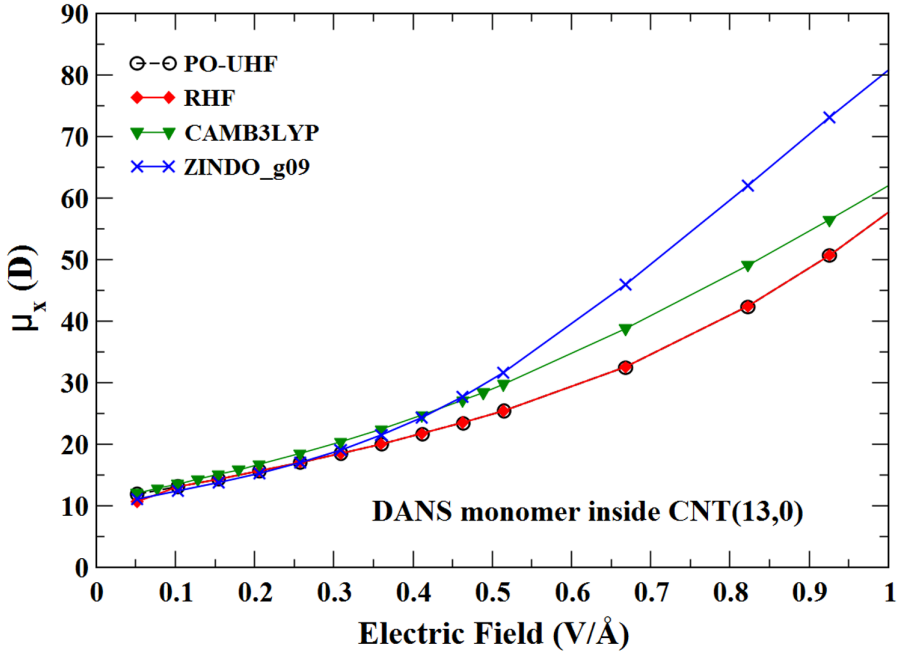

Figure 3.11: The molecular dipole moment evolution with an applied electric field directed along the x-direction that joins the two N atoms inside the DANS. Only the component of the dipole along the field direction is shown. Results obtained for the singlet states of DANS in the geometry calculated inside CNT(13,0) are shown for different levels of theory.

The reason for this strange result is that the zwitterionic state has a biradical character that is hard to capture. Therefore we chose a different strategy and repeated the calculation, in precisely the same geometry, for a triplet ground state. As it can be seen in the right panel of Fig. 3.12 (using CAM-B3LYP functional), at large value of electric field the ground state switches from a singlet to a triplet state. We assume that this switching corresponds to the switching from a globally neutral closed shell ground state (DA) to biradicaloid zwitterionic (D^+A^-) ground state. The two plateaus, relevant to the two states, can therefore be reconstructed from the $\mu_x(E)$ dependence calculated for the singlet and triplet states, as shown in the right panel of Fig. 3.12.

Thus, having identified the neutral and zwitterionic states, we calculated the corresponding ESP charges (those that best mimic electrostatic potential). Fig. 3.13 shows the charges calculate for the DANS in the N state, arbitrarily set as the singlet

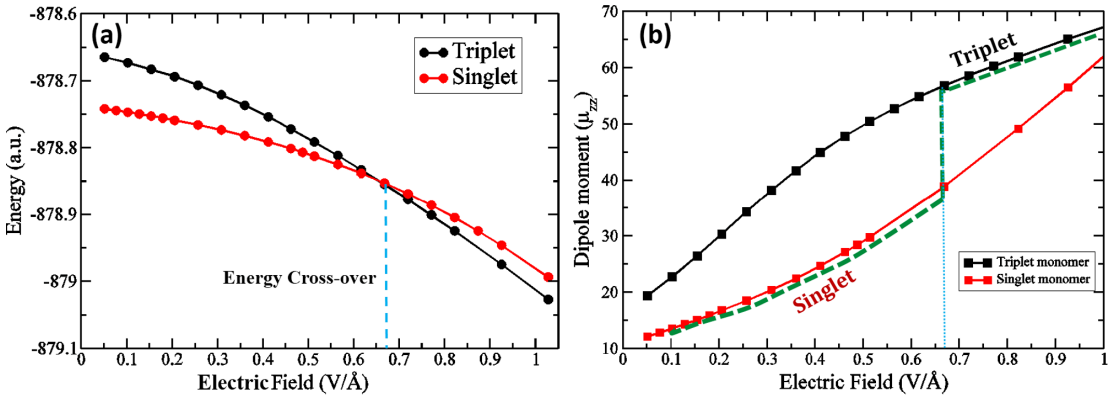

Figure 3.12: (a) Energy for singlet and triplet ground states of a DANS molecule (geometry inside CNT(13,0)) plotted as a function of an applied electric field E, and (b) applied field dependence of the dipole moment μ_x calculated for the singlet and triplet states. The green dashed line in (b) indicates the two-plateau curve reconstructon of the μ_x *vs.* E.

state, calculated in the absence of field ($E = 0$), and for the Z state, set as the triplet state calculated at field strength $E = 0.66V/\mathring{A}$). Results in the figure refer to the geometry of DANS inside CNT(13,0). In the N state, cumulative charge of the donor fragment is +0.128 and on the acceptor is -0.13, while for the Z state the sum of charges in donor fragment is +0.875 and on the acceptor is -0.875, showing approximately one electron is transferred in the Z state. The results are marginally affected by the geometry and by the specific choice of the electric fields used to identify the N and Z states.

Based on the ESP atomic charges calculated for DANS forced in the N and Z state, we can estimate corresponding intermolecular interactions as follows:

$$V_{N/Z} = \Sigma_{i,j} \frac{\rho^i_{N/Z} \rho^j_{N/Z}}{r_{ij}} \tag{3.5}$$

where, i and j count the atomic sites in each one of the two DANS molecules within the dimer, r_{ij} stands for the interatomic distances, $\rho^i_{N/Z}$ is the ESP charge calculated for atom i for the N/I state. Results are collected in Table 3.3. While the results are marginally affected by the adopted geometry, we recalculated ESP charges accounting for the specific geometry of each $DANS_2$@CNT.

The agreement between the extended dipole estimate of the interaction with the

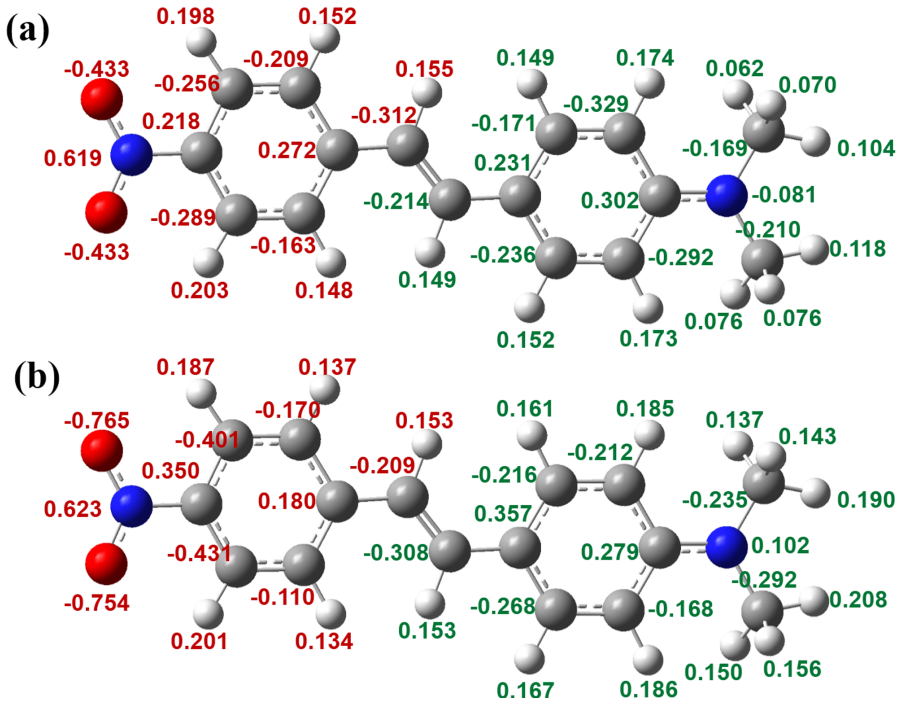

Figure 3.13: ESP atomic charges calculated for DANS inside CNT(13,0) in the (a) N (in singlet state) and (b) Z state ($E = 0.66$ V/Å, triplet state). Numbers in red indicate acceptor fragment and green for donor fragment.

Table 3.3: Intermolecular interactions calculated for the zwitterionic and neutral dimer, and their difference V_{eff}, corresponding to the DFT estimate of the V interaction, for the sake of comparison, the last column shows the extended dipole estimate of V

CNT Type	Diameter (nm)	V_Z (eV)	V_N (eV)	V_{eff} (eV)	V_{ed} (eV)
CNT(10,0)	0.79	-2.52	-0.092	-2.43	-1.85
CNT(13,0)	1.03	-1.62	-0.099	-1.52	-1.52
CNT(12,3)	1.09	-1.96	-0.132	-1.83	-1.85
CNT(8,8)	1.10	-0.80	-0.035	-0.76	-0.82
CNT(12,4)	1.14	-0.76	-0.038	-0.74	-0.75
CNT(9,9)	1.24	-2.04	-0.136	-1.90	-2.14

estimate based on ESP charges is extremely good and fully supports the value of the average $V \sim 1.35$ eV as estimated from the analysis of experimental results.

3.5 Conclusions

A bottom-up modeling strategy was successfully adopted to rationalize the observed amplification of HRS signals in DANS@CNT solutions, as reported in Ref. [36]. The proposed approach starts from a detailed analysis of spectroscopic properties of DANS in solution. The developed ESM is able to reproduce based on a handful of molecular model parameters linear, two-photon absorption spectra and fluorescence spectra of DANS in different solvents, as well as the HRS spectra collected in chloroform. The same model is then used to build a model for linear DANS aggregates. The aggregate model requires an estimate of the intermolecular interaction among zwitterionic DANS molecule that is set to $V = -1.35$ eV in order to reproduce the observed position of the linear absorption spectrum, to account for the disorder, we impose a gaussian distribution around the average V and this *ad hoc* choice of the intermolecular interactions is nicely validated by DFT results. The proposed model quantitatively reproduces observed features in terms of band positions, bandshapes and intensities accounting for linear DANS aggregates containing 7 molecules. This is in striking contrast with the interpretation of experimental data given in the original paper Ref. [36], where, under the assumption of additive HRS response, the authors concluded that 69 molecules are aligned inside the CNT. Additive HRS response is however only expected for non-interacting dyes, while important intermolecular interactions are demonstrated experimentally by the huge red-shift of the linear absoprtion band when going from solution to the aggregate. As originally discussed in Ref. [4, 38] a huge amplification of the β response is expected for aggregates of aligned DA dyes with a neutral ground state, accordingly huge HRS responses can be obtained upon aligning a reasonably small number of dyes. We feel this is an important result, as it may suggest experimentalists the possibility to achieve large β responses in systems where just a few (2-3) dyes are aligned, a much more easy task, with respect to the alignment of tens of molecules.

Bibliography

[1] N. J. Tao, Nat. Nanotechnol. **1**, 173 (2006).

[2] F. Terenziani, G. D'Avino, and A. Painelli, ChemPhysChem **8**, 2433 (2007).

[3] C. Katan, F. Terenziani, O. Mongin, M. H. V. Werts, L. Porrs, T. Pons, J. Mertz, S. Tretiak, and M. Blanchard-Desce, J. Phys. Chem. A **109**, 3024 (2005).

[4] A. Painelli and F. Terenziani, J. Am. Chem. Soc. **125**, 5624 (2003).

[5] M. Maus, W. Rettig, D. Bonafoux, and R. Lapouyade, J. Phys. Chem. A **103**, 3388 (1999).

[6] E. Vogel, Nat. Nanotechnol. **2**, 25 (2007).

[7] L. R. Dalton, P. A. Sullivan, and D. H. Bale, Chem. Rev. **110**, 25 (2010).

[8] M. J. Cho, D. H. Choi, P. A. Sullivan, A. J. Akelaitis, and L. R. Dalton, Progress in Polymer Science **33**, 1013 (2008).

[9] C. Reichardt, Chem. Rev. **94**, 2319 (1994).

[10] F. Bureˇ s, O. r. Pytela, M. Kivala, and F. c. Diederich, J. Phys. Org. Chem. **24**, 274 (2011).

[11] C. Dehu, F. Meyers, E. Hendrickx, K. Clays, A. Persoons, S. R. Marder, and J. L. Bredas, J. Am. Chem. Soc. **117**, 10127 (1995).

[12] A. Marini, S. Macchi, S. Jurinovich, D. Catalano, and B. Mennucci, J. Phys. Chem. A **115**, 10035 (2011).

[13] A. Painelli, Chem. Phys. Lett. **285**, 352 (1998).

[14] A. Painelli, Chem. Phys. **245**, 185 (1999).

[15] F. Terenziani, A. Painelli, and D. Comoretto, J. Phys. Chem. A **104**, 11049 (2000).

[16] B. Boldrini, E. Cavalli, A. Painelli, and F. Terenziani, J. Phys. Chem. A **106**, 6286 (2002).

[17] F. Terenziani, A. Painelli, A. Girlando, and R. M. Metzger, J. Phys. Chem. B **108**, 10743 (2004).

[18] L. Grisanti, G. D'Avino, A. Painelli, J. Guasch, I. Ratera, and J. Veciana, J. Phys. Chem. B **113**, 4718 (2009).

[19] F. Terenziani and A. Painelli, Chem. Phys. **295**, 35 (2003).

[20] A. Painelli, L. D. Freo, and F. Terenziani, Chem. Phys. Lett. **346**, 470 (2001).

[21] Y. Liao, K. A. Firestone, S. Bhattacharjee, J. Luo, M. Haller, S. Hau, C. A. Anderson, D. Lao, B. E. Eichinger, B. H. Robinson, P. J. Reid, A. K.-Y. Jen, and L. R. Dalton, J. Phys. Chem. B **110**, 5434 (2006).

[22] D. R. Kanis, M. A. Ratner, and T. J. Marks, Chem. Rev. **94**, 195 (1994).

[23] S. Di Bella, M. A. Ratner, and T. J. Marks, J. Am. Chem. Soc. **114**, 5842 (1992).

[24] F. Castet, A. Pic, and B. Champagne, Dyes and Pigm **110**, 256 (2014), 1st International Caparica Conference on Chromogenic and Emissive Materials.

[25] A. K.-Y. Jen, Y. Liu, L. Zheng, S. Liu, K. J. Drost, Y. Zhang, and L. R. Dalton, Adv. Mat. **11**, 452 (1999).

[26] L. R. Dalton, A. W. Harper, R. Ghosn, W. H. Steier, M. Ziari, H. Fetterman, Y. Shi, R. Mustacich, A.-Y. Jen, and K. J. Shea, Chem. Mater. **7**, 1060 (1995).

[27] C. Zhang, A. S. Ren, F. Wang, J. Zhu, L. R. Dalton, J. N. Woodford, and C. H. Wang, Chem. Mater. **11**, 1966 (1999).

[28] L. Dalton, in *Polymers for Photonics Applications I* (Springer Berlin Heidelberg, 2002) pp. 1–86.

[29] L. R. Dalton, P. A. Sullivan, and D. H. Bale, Chem. Rev. **110**, 25 (2009).

[30] T. Xu, A. Morris, G. J. Szulczewski, R. R. Amaresh, Y. Gao, S. C. Street, L. D. Kispert, R. M. Metzger, and F. Terenziani, J. Phys. Chem. B **106**, 10743 (2002).

[31] A. Girlando, C. Sissa, F. Terenziani, A. Painelli, A. Chwialkowska, and G. J. Ashwell, ChemPhysChem **8**, 2195 (2007).

[32] M. Alvaro, H. Garc´ia, S. Garc´ia, F. Márquez, and J. C. Scaiano, J. Phys. Chem. B **101**, 3043 (1997).

[33] H. S. Kim, S. M. Lee, K. Ha, C. Jung, Y.-J. Lee, Y. S. Chun, D. Kim, B. K. Rhee, and K. B. Yoon, J. Am. Chem. Soc. **126**, 673 (2004).

[34] T. K. Shim, M. H. Lee, D. Kim, H. S. Kim, and K. B. Yoon, J. Fluoresc. **22**, 1475 (2012).

[35] K. Yanagi, K. Iakoubovskii, H. Matsui, H. Matsuzaki, H. Okamoto, Y. Miyata, Y. Maniwa, S. Kazaoui, N. Minami, and H. Kataura, J. Am. Chem. Soc. **129**, 4992 (2007).

[36] S. Cambré, J. Campo, C. Beirnaert, C. Verlackt, P. Cool, and W. Wenseleers, Nat. Nanotechnol. **10**, 248 (2015).

[37] J. Yu, Y. Cui, C. Wu, Y. Yang, Z. Wang, M. O'Keeffe, B. Chen, and G. Qian, Angew. Chem. Int. Ed. **51**, 10542 (2012).

[38] F. Terenziani and A. Painelli, Phys. Rev. B **68**, 165405 (2003).

[39] M. A. Smirnov, A. S. Mukhtarov, N. V. Ivanova, T. A. Vakhonina, V. V. Semashko, and M. Y. Balakina, Journal of Physics: Conference Series **560**, 012015 (2014).

[40] A. Datta and S. K. Pati, Chem. Soc. Rev. **35**, 1305 (2006).

[41] P. C. Ray and J. Leszczynski, Chem. Phys. Lett. **419**, 578 (2006).

[42] D. R. Kanis, M. A. Ratner, and T. J. Marks, Chem. Rev. **94**, 195 (1994).

[43] V. Parthasarathy, R. Pandey, F. Terenziani, P. K. Das, and M. Blanchard-Desce, Phys. Chem. Chem. Phys. **16**, 9096 (2014).

[44] M. M. J. Treacy, T. W. Ebbesen, and J. M. Gibson, Nature **381**, 678 (1996).

[45] S. Iijima, Nature **354**, 56 (1991).

[46] M. D. G. D. P. Eklund, *Science of Fullerenes and Carbon Nanotubes, Their Properties and Applications, Edn.1* (Academic Press, New York, 1996).

[47] J. M. Marulanda, *Electronic Properties of Carbon Nanotubes* (InTech, 2011).

[48] T. W. Odom, J.-L. Huang, and C. M. Lieber, Annals of the New York Academy of Sciences **960**, 203 (2002).

[49] C. Sissa, F. Terenziani, A. Painelli, A. Abbotto, L. Bellotto, C. Marinzi, E. Garbin, C. Ferrante, and R. Bozio, J. Phys. Chem. B **114**, 3076 (2010).

[50] S. Sanyal, A. Painelli, S. K. Pati, F. Terenziani, and C. Sissa, Phys. Chem. Chem. Phys. **18**, 28198 (2016).

[51] G. D'Avino, F. Terenziani, and A. Painelli, J. Phys. Chem. B **110**, 25590 (2006).

[52] G. D'Avino, L. Grisanti, J. Guasch, I. Ratera, J. Veciana, and A. Painelli, J. Am. Chem. Soc. **130**, 12064 (2008).

[53] A. Painelli and F. Terenziani, J. Phys. Chem. A **104**, 11041 (2000).

[54] G. Wicks, A. Rebane, and M. Drobizhev, Proc. SPIE **8983**, 89830R (2014).

[55] J. Campo, A. Painelli, F. Terenziani, T. Van Regemorter, D. Beljonne, E. Goovaerts, and W. Wenseleers, J. Am. Chem. Soc. **132**, 16467 (2010).

[56] F. C. Spano, Acc. Chem. Res. **43**, 429 (2010).

[57] A. D. Becke, Phys. Rev. A **38**, 3098 (1988).

[58] C. Lee, W. Yang, and R. G. Parr, Phys. Rev. B **37**, 785 (1988).

[59] J. VandeVondele, M. Krack, F. Mohamed, M. Parrinello, T. Chassaing, and J. Hutter, Comput. Phys. Commun. **167**, 103 (2005).

[60] J. Hutter, M. Iannuzzi, F. Schiffmann, and J. VandeVondele, WIREs Comput Mol Sci **4**, 15 (2014).

[61] M. Krack, Theor Chem Acc **114**, 145 (2005).

[62] C. Hartwigsen, S. Goedecker, and J. Hutter, Phys. Rev. B **58**, 3641 (1998).

[63] S. Goedecker, M. Teter, and J. Hutter, Phys. Rev. B **54**, 1703 (1996).

[64] W. Humphrey, A. Dalke, and K. Schulten, Journal of Molecular Graphics **14**, 33 (1996).

[65] C. Sissa, F. Terenziani, A. Painelli, A. Manna, and S. Pati, Chem. Phys. **404**, 9 (2012), electronic Processes in Organic Systems.

[66] C. Sissa, A. K. Manna, F. Terenziani, A. Painelli, and S. K. Pati, Phys. Chem. Chem. Phys. **13**, 12734 (2011).

[67] V. Geskin, R. Stadler, and J. Cornil, Phys. Rev. B **80**, 085411 (2009).

Chapter 4

Study of the Charge-Transfer and Locally-Excited States' Manifold in a Biphenyl-Based Push-Pull Chromophore†

4.1 Introduction

Molecules having an elongated π-conjugation are very interesting building blocks for molecular functional materials due to the presence of a large number of delocalized electrons, which favours long distance electron transfer. Thus, they have received huge attention as potential candidates in emerging research studies, for example, as molecular rectifiers [1], in molecular electronics [2], photovoltaics [3–5] or light-emitting systems [6].

Biphenyl systems are molecules composed of two adjacent benzene rings as individual π systems and are ideal model systems for investigating electronic transport

†Works reported in this chapter are in collaboration with experimentalists, Prof. M. Blanchard-Desce from University of Bordeaux who synthesized the molecule, Dr. M. Di Donato of LENS, Florence, who collected non-linear time-resolved spectra , and Dr. Elisa Campioli and Prof. Francesca Terenziani working with the linear spectroscopic characterization. *Manuscript under preparation*

properties [7–11]. Various "push-push" and "push-pull" systems have been synthesized by functionalizing biphenyl cores [7, 12], which find applications in two-photon absorption studies, non-linear optical property studies among others. The extent of π overlap in the two benzene rings and thus the overall extent of electron delocalization over the entire π system dictates the electronic interaction through the synthon. This varies with the torsional angle between the planes of the two phenyl rings. Particularly, a large conjugation is expected for a biphenyl system with both phenyl rings in the same plane. On the other hand, delocalization is disrupted in compounds where the two rings are perpendicular to each other. The electron cloud density over the phenyl rings is altered by different substituents influencing the expected torsional angles, as well as thermal motion which leads to variation in the torsional angles of simple biphenyl systems formed by a C-C single bond link between the two phenyl rings.

Photophysical properties of biphenyl-based fluorescent dyes are sensitive to local steric factors [7]. Fluorescence phenomena that involve energy transfer, partial charge transfer or pure electron transfer, excimer/exciplex formation and *J*- or *H*-aggregations are affected by the relative distance/orientation of fluorophores, the conformation of individual fluorophores and their transfer mobility. Biphenyl-based fluorophores are not only well-known versatile reporters for steric environments at mesoscopic and microscopic scales, but are also expected to be a motifs of novel functional molecules because certain steric restrictions or well-ordered arrangement of fluorophores may activate unprecedented photophysical properties [8].

In this chapter, we have worked with a biphenyl "push-pull" chromophore, having an extended π-conjugated system. We have analyzed the locally-excited (LE) and charge transfer (CT) state interplay in this chromphore using ZINDO calculations.

4.2 Computational Details

All the quantum chemical calculations for **CVA07** in gasphase and solvents have been carried out using Density Functional Theory (DFT) and Time Dependent DFT (TDDFT) as implemented in the Gaussian 09 package [13]. Long-range

Coulomb attenuated functional CAM-B3LYP [14] has been used for the optimization of the molecule and the spectral properties of the excited state. The optimized ground state (S_0) geometries have been confirmed to be in local minimum energy structures by analyzing the vibrational frequencies in the ground state. We have used 6-31+g(d) basis set for all the calculations and to mimic dichloromethane (DCM), cyclohexane and toluene solvents, polarizable continuum model (PCM)[15] as implemented in Gaussian 09 package. To look into the excited state geometry in gasphase for **CVA07**, optimization of the first charge transfer (CT) state and the first local excited state (LE) were carried out using the above mentioned level of theory. We tried to look into the optimized geometry of the excited state even in solvent, but due to computational limitations and heavy nature of the calculations, it could not be achieved. Since we are interested to the calculation of high energy excited states, a task that becomes too expensive in TDDFT, we have resorted to the semi-empirical ZINDO calculations, as implemented in G09, to look into the nature of the transitions.

4.3 System Under Study

The chromophore studied here, hereafter referred to as **CVA07**, is a dipolar chromophore (D-A) where the amine donor group and the cyano acceptor group are connected through a substituted biphenyl moiety (Fig. 4.1). In particular, the 2-2$'$ and 6-6$'$ positions of the biphenyl are substituted by methyl groups and the steric hindrance of these methyl groups exerts a strong twist of the two phenyl rings, their planes being almost perpendicular to one another in the ground state. The twisted biphenyl structure strongly reduces the conjugation between the donor and acceptor side of the molecule, so that we expect the charge-transfer (CT) transition to be only weakly allowed in absorption.

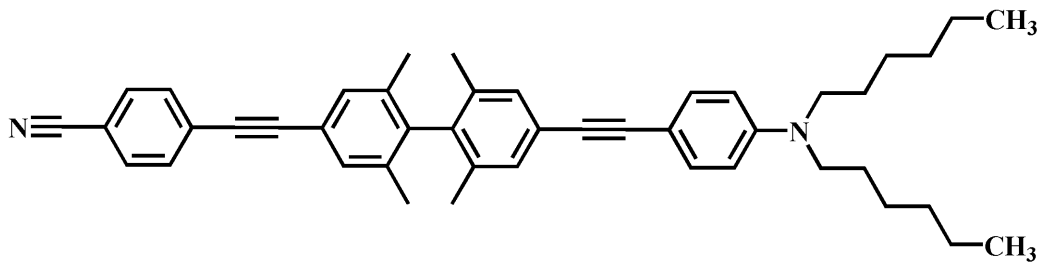

Figure 4.1: The substituted biphenyl core chromophore (CVA07) under study.

4.4 Results and Discussions

4.4.1 Experimental Results

The absorption and emission spectra of **CVA07** were measured in solvents of different polarity, namely cyclohexane, toluene, diethyl ether, tetrahydrofuran (THF), 2-methyltetrahydrofuran (2-MeTHF) and dichloromethane (DCM), and we have tabulated the spectral properties in Table 4.1. Fig. 4.2 shows the relevant spectral curves.

Table 4.1: Main spectral properties of CVA07 in solvents of different polarity.

Solvent	λ_{abs} (nm)	λ_{em} (nm)	ϵ_{max} ($M^{-1}cm^{-1}$)	Φ	τ^a (ns)	k_r $10^8 s^{-1}$	k_{nr} $10^8 s^{-1}$
Cyclohexane	327	367	73000	0.650	0.70	9.28	5.00
Toluene	329	409	-	0.470	4.08	1.15	1.30
Diethyl ether	326	484	-	0.150	11.7	0.13	0.72
2-Me THF	327	560	-	0.056	9.32	0.06	1.01
THF	328	592	64000	0.024	6.00	0.04	1.63
DCM	331	625	-	0.005	2.06 (95%) 9.39 (5%)	0.01	3.68

[a]measured at the frequency of the maximum of the fluorescence band.

The absorption spectrum is centered at ∼325 nm and is composed by a few partly overlapping bands. When increasing the solvent polarity, no appreciable shift of the bands is observed, while the bands broaden in particular when going from the completely apolar solvent cyclohexane to any of the other solvents. The oscillator strength associated to the absorption band amounts to 2.2, corresponding

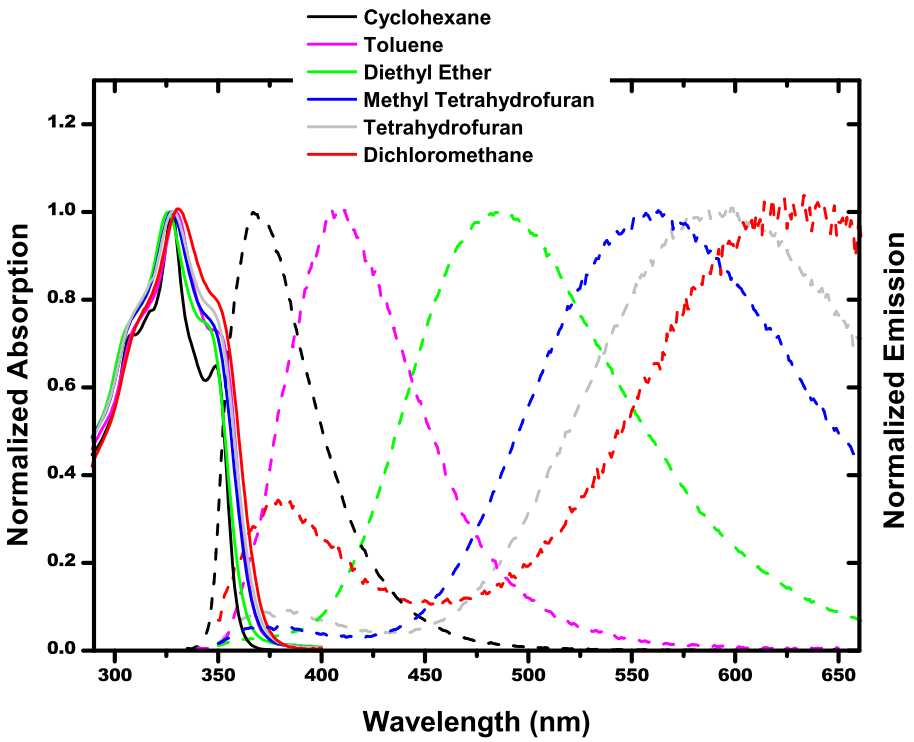

Figure 4.2: Absorption and emission spectra of CVA07 in solvents of different polarity. Solid line indicates absorption and dashed line indicates emission.

to a transition dipole moment of about 7.2 D. Such an intense transition cannot be associated to the charge transfer from the donor to the acceptor moiety, since the CT transition is almost hindered by the twisted structure. We then assign this group of partly overlapping bands to transitions to locally-excited (LE) states.

A very interesting behavior was observed for emission. In the apolar solvent cyclohexane, a strong emission is detected, having a quantum yield of 0.65 and located in the blue region of the visible spectrum, partly overlapped with the absorption band. When the solvent polarity is increased, the emission band progressively shifts to the red and loses intensity, the quantum yield becoming <1% in DCM. More polar solvents (such as CH_3CN and DMSO) were tested, but no fluorescence could be detected. Moreover, in medium-high polarity solvents a dual emission is observed, with the main band located at longer wavelengths in a position depending on the solvent polarity, and another, less intense band in the same position as the emission

band recorded in cyclohexane.

This behavior can be interpreted by assigning the emission in cyclohexane as emerging from an LE state. The residual emission in the same spectral position observed in polar solvents is assigned to the same LE state, while the solvatochromic emission band observed is clearly associated to a CT transition. Since fluorescence emission typically stems from the lowest-energy excited state, this behavior suggests that the lowest-energy excited state has an LE nature in apolar solvents, while in polar solvents the relaxed CT state is stabilized, becoming lower in energy than the LE state. The residual emission still observed from the LE state in polar solvents can be ascribed to a small population still residing on the LE state and is justified by the very different radiative emission rates associated to the LE and CT states (Table 4.1).

Using the Weisskopf-Wigner equation [16, 17] for the radiative decay rate, we can estimate the transition dipole moment associated to the emission and we obtain values of ∼12 D in cyclohexane, ∼5 D in toluene, decreasing down to ∼1 D in DCM. These values are in agreement with the interpretation of the emission arising from a strongly allowed LE state in the apolar solvent, while corresponding to an almost forbidden CT transition in polar solvents. Toluene seems to be an intermediate case, where the excited-state population could be distributed on both types of states, suggesting that the relaxed LE and CT states are almost degenerate in this solvent.

This LE/CT interplay is interesting. In particular, while in the apolar solvent absorption and emission involve the same LE state, in polar solvents excitation still populates the LE state(s), while the emission data suggest that the population relaxes (almost completely) towards a lower-energy CT state. This relaxation should be solvent-driven, since solvation is responsible for the stabilization of the CT excited state.

In order to investigate better the nature of the excited states and the evolution from the LE to the CT state, transient absorption measurements were performed (in collaboration with LENS in Florence) in solvents of different polarity and characterized by different relaxation times (Fig. 4.3). The pump pulse was centered at 330 nm, while the probe pulse is broadband, covering the region from 350 to 700 nm.

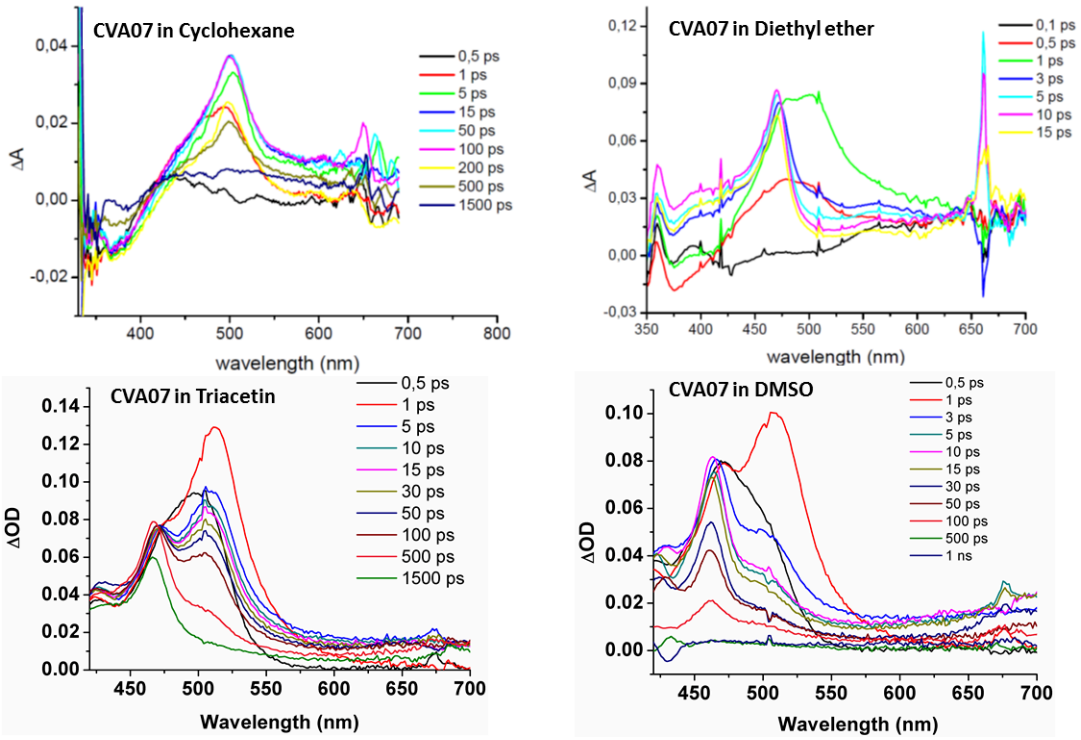

Figure 4.3: Transient pump-probe spectra measured in cyclohexane, diethyl ether, triacetin and in DMSO.

The positive band dominating the differential absorption spectra is due to excited-state absorption (ESA) from the state reached via pumping at 330 nm towards higher-energy excited state(s). In the apolar solvent cyclohexane, no evolution of this band is observed apart from its progressive decrease in intensity due to the de-population of the excited state itself, on a timescale shorter than 1 ns. This is in agreement with the estimated fluorescence lifetime (Table 4.1). More interesting fact is the time evolution of the pump-probe spectra in polar solvents. In all investigated polar solvents (diethyl ether, triacetin, DMSO), two excited-state absorption bands are observed in the transient spectra, located at about 520 nm and 460 nm. The relative intensity of the two bands changes with time delay, *i.e.*, for short pump-probe delays, the 520 nm feature dominates, while for increasing time delays a band at 460 nm appears and progressively acquires intensity at the expense of the other. The kinetic of this evolution is clearly governed by the solvent. In fact while the qualitative evolution is very similar in all the polar solvents, the associated times are different and compare very well with the average solvation

times reported in the literature for the three solvents, namely 1.7 ps for diethyl ether, 3.1 ps for DMSO, 80 ps for triacetin.

The two features in the transient absorption spectra can safely be ascribed to an excited-state absorption from the LE state and to an excited-state absorption from the CT state; the first one (at 520 nm) decreases and the second one (at 460 nm) increases on the typical solvation timescale. The pump pulse populates the LE state, but solvation (its typical times depending on the specific solvent) stabilizes the CT state to lower energy, so that the population moves from the LE to the CT state. Accordingly, the excited-state absorption feature shows the gradual decrease of the transition from the LE state and the gradual increase of the transition from the CT state.

Having assigned the ESA features, we were somewhat surprised by the fact that these two features do not change their spectral positions during time. This is particularly surprising from the point of view of the feature associated to the CT state, since the energy of the CT state is very sensitive to solvation (as has been demonstrated by the strong emission solvatochromism). Transient data thus clearly suggests that the state reached upon absorption from the CT state has the same solvatochromic behavior as the initial state, *i.e.*, has a CT nature too. Analogously, the excited-state reached upon absorption from the LE state should have a LE character too.

To prove this interpretation, we performed theoretical calculations to retrieve the energies of a large number of excited states in order to study their nature.

4.4.2 Theoretical Results

To model the **CVA07** molecule for theoretical calculations, we have substituted the long chain alkyl group in the amino moiety with methyl groups, with the assumption that this has marginal spectroscopic effects. The optimized structure of the molecule in gasphase is shown in Fig. 4.4 and we can see the biphenyl moiety is twisted along the C-C bond by around 90°. This hinders the conjugation of the π cloud across the twisted bridge. The ground state system was also optimized in different solvents, cyclohexane, toluene and dichloromethane (DCM) obtaining similar results.

To look into the transition energies of **CVA07** in different solvents, namely

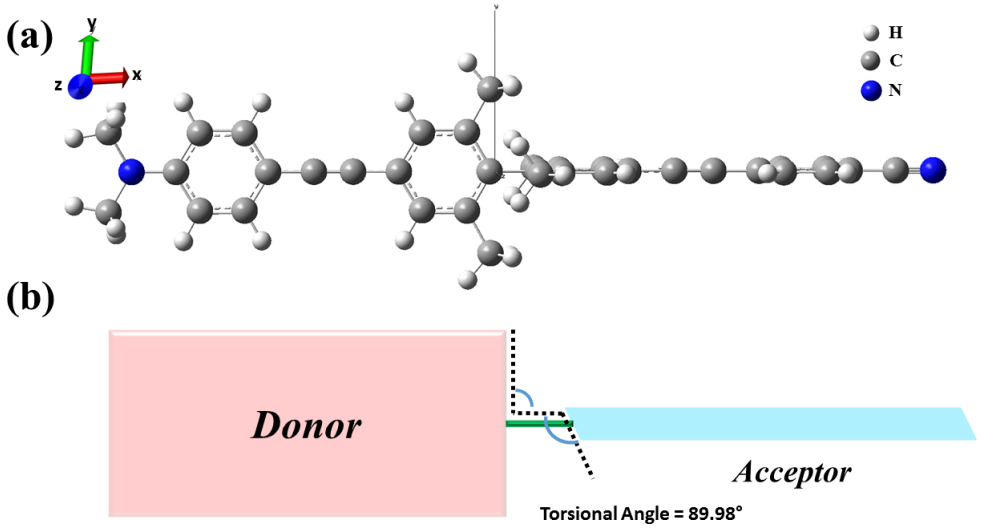

Figure 4.4: (a) Optimized structure of CVA07 in gasphase, and (b) perpendicular planes in the molecule with a torsional angle of ∼90°.

cyclohexane, toluene, DCM and in gasphase, we carried out TDDFT calculations on the monomer and Table 4.2 summarizes the first few low-energy transitions. Several flavours of PCM models are available and we have used state-specific approximation [18], which is a more accurate and physically sound approach to take into account the variations of the polarization of the solvent following the electronic density rearrangements of the solute [19].

Results in Table 4.2 are consistent with the experimental results, showing no appreciable change in absorption band position while moving from low to highly polar solvents. The first transition (S0→S1), irrespective of the polarity of the solvent is an LE transition with an almost equal weight of two localized excitations on the donor fragment (H→L+1) and on the acceptor fragment (H-1→L). The large solvatochromic shifts in the experimental fluorescence spectra showed that the relaxed excited state is polar, *i.e.*, it should be a charge separated state (CS). The calculated CT state is found at a higher energy, corresponding to S3 in gasphase and cyclohexane and S4 in toluene and DCM. The CT state corresponds to H→L transition, displacing charge from D to the A site. The energy of the CT state is marginally affected by the solvent polarity, indeed because of the negligible polarity of the molecule in the ground state. Moving ahead, emission spectra calculations with TDDFT could not be completed on account of computational limitations owing

Table 4.2: TDDFT Results for CVA07 in Gasphase and different solvents.

CVA07 in	Transitions	Transition Energy (nm/eV)	Oscillator Strength	Nature of Transitions (MO Contributions)
Gasphase	S0 → S1	308 / 4.02 (LE)	3.03	H-1→L (38%)
				H→L+1 (52%)
	S0 → S2	293 / 4.23	0.01	H-1→L (53%)
				H→L+1 (37%)
	S0 → S3	273 / 4.53 (CT)	0.00	H→L (87%)
Cyclohexane	S0 → S1	315 / 3.93 (LE)	3.26	H-1→L (35%)
				H→L+1 (55%)
	S0 → S2	302 / 4.10	0.03	H-1→L (56%)
				H→L+1 (35%)
	S0 → S3	274 / 4.52 (CT)	0.00	H→L (88%)
Toluene	S0 → S1	316 / 3.92 (LE)	3.28	H-1→L (35%)
				H→L+1 (56%)
	S0 → S2	303 / 4.09	0.04	H-1→L (57%)
				H→L+1 (34%)
	S0 → S3	274 / 4.52	0.06	H→L+7 (70%)
	S0 → S4	274 / 4.52 (CT)	0.00	H→L (88%)
DCM	S0 → S1	322 / 3.34 (LE)	3.24	H-1→L (25%)
				H→L+1 (65%)
	S0 → S2	312 / 3.97	0.17	H→L+6 (66%)
				H→L+1 (25%)
	S0 → S3	278 / 4.46	0.09	H→L+6 (67%)
	S0 → S4	273 / 4.55 (CT)	0.00	H→L (89%)

to the number of atoms in the molecule.

To identify the nature of the transitions occurring from the first LE and the first CT states, it is important to analyze the transition dipole moments between the excited states. Though these can be achieved with Dalton package using TDDFT formalism, we needed to reach much higher energy states and the size of the molecule proved a hindrance. To handle this problem, we have carried out semi-empirical

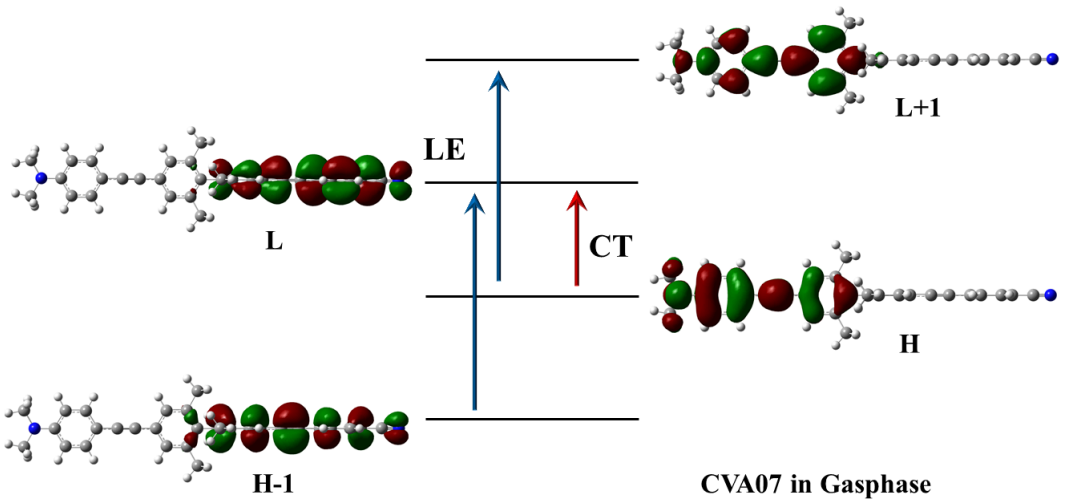

Figure 4.5: Frontier Molecular Orbitals of CVA07 in gasphase and the LE/CT transitions. Blue arrow indicates LE transition and red arrow indicates CT transition.

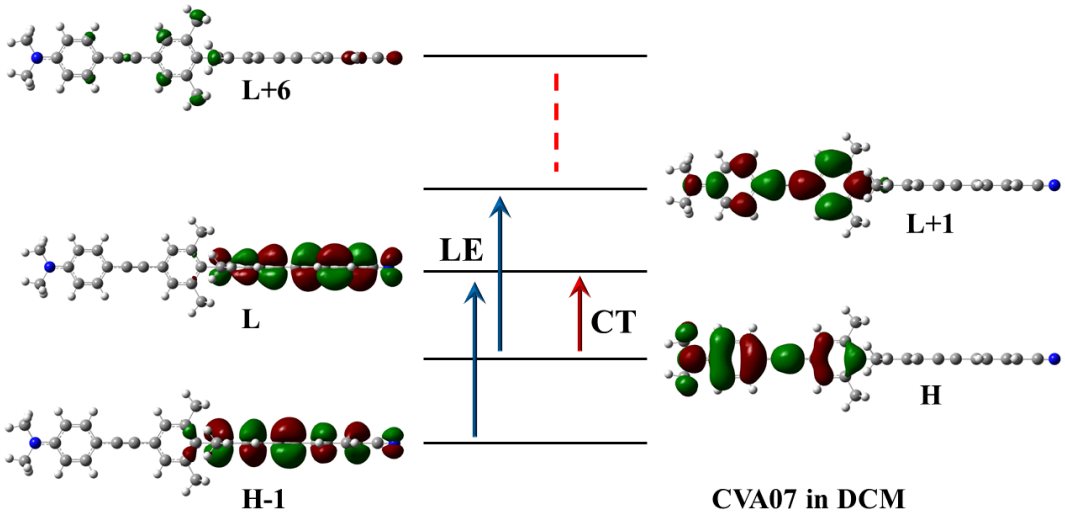

Figure 4.6: Frontier Molecular Orbitals of CVA07 in DCM solvent and the LE/CT transitions. Blue arrow indicates LE transition and red arrow indicates CT transition.

ZINDO/S calculations in gasphase, implemented in Gaussian09 package, to calculate the transition dipole moments between excited states and due to the nature of the calculations we could reach up to 7 eV of transition energy. In Table 4.3, we have summarized the lowest-lying first few transitions of **CVA07** in gasphase, using ZINDO/S calculations. In comparison to the experimental data, there is an

underestimation of the first strongly allowed transition energy in gasphase by ∼0.3 eV.

Table 4.3: ZINDO Results for CVA07 showing the first few low energy transitions.

Transitions	Transition Energy (nm/eV)	Oscillator Strength	Nature of Transitions (MO Contributions)
S0 → S1	357 / 3.47 (LE)	1.91	H-1→L (33%)
			H→L+1 (43%)
S0 → S2	352 / 3.53	0.00	H-8→L (56%)
S0 → S3	344 / 3.60	0.00	H-5→L+1 (59%)
S0 → S4	342 / 3.62	0.01	H-1→L (39%)
			H→L+1 (33%)
S0 → S5	307 / 4.04	0.05	H→L+6 (69%)
S0 → S6	302 / 4.11	0.01	H→L+5 (37%)
S0 → S7	299 / 4.14	0.00	H-1→L+4 (45%)
S0 → S8	291 / 4.26	0.00	H-9→L (34%)
			H-1→L+2 (41%)
S0 → S9	285 / 4.34 (CT)	0.00	H→L+14 (37%)
			H→L+17 (23%)
S0 → S10	280 / 4.43	0.00	H-1→L+11 (57%)

The LE and CT states (as labelled in Table 4.3) have been identified by analyzing the nature of each molecular orbital (see Fig. 4.7) taking part in each transition and having a sizeable contribution. Thus, we could identify the LE transition to be the lowest-energy one at 3.47 eV (357 nm, S0→S1) and the CT transition occurs at a higher energy of 4.34 eV (285 nm, S0→S9). Having identified the first LE and CT state as S1 and S9, respectively, we looked at the transition dipole moments ($\mu_{ti,i=x,y,z}$) from these states to the higher energy states. Since, from Fig. 4.4, we can see the molecular axis of the **CVA07** lies along x-axis of the cartesian coordinate system, and the donor and acceptor fragments lie along this axis, it is justified to look into the x-component of μ_t. In Tables 4.4 and 4.5, we have tabulated the transition energies from the first LE (S1 state) and first CT (S9 state) to the higher states based on sizeable μ_{tx} values. The FMO's taking part in these transitions have also been checked to verify the nature of each transition.

The excited state to excited state transitions, from S1 and S9 to higher, involves

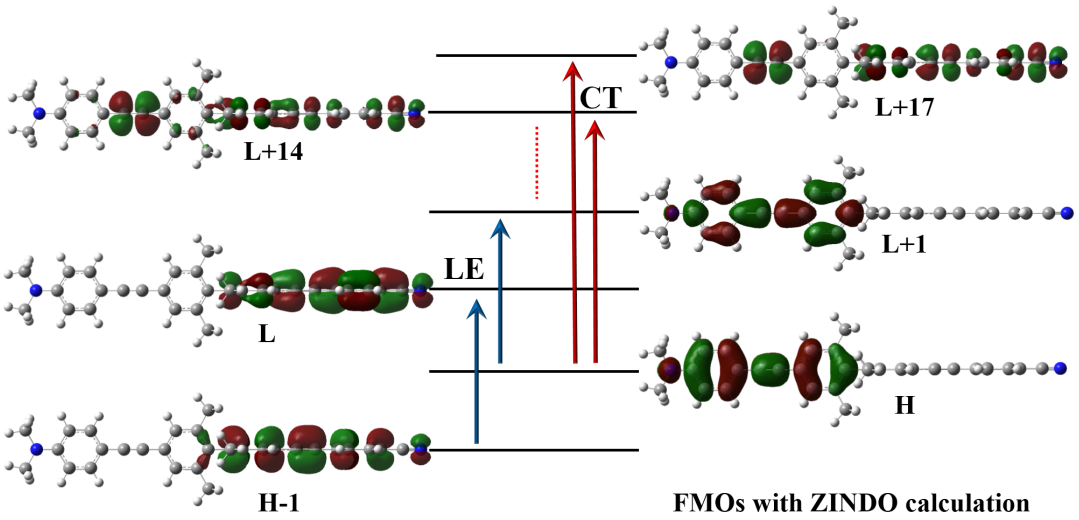

Figure 4.7: Frontier Molecular Orbitals of CVA07 obtained with ZINDO calculations showing the LE/CT transitions. Blue arrow indicates LE transition and red arrow indicates CT transition.

Table 4.4: Transitions from S1 to higher energy Sn (n>1) and the transition dipole moments.

Lowest LE State (LE_1)	Higher LE State (LE_n)	μ_{tx} (a.u.)	ΔE/eV (nm)
S1	S4	0.3062	0.27 (∼4500)
	S12	1.0317	1.23 (∼1000)
	S14	0.8502	
	S22	-3.0683	
	S24	1.8033	1.99 (∼620)
	S26	3.0691	
	S32	-0.9658	2.30 (∼540)
	S33	-0.6430	
	S40	0.8957	2.64 (∼470)
	S41	-0.6838	
	S57	0.3845	
	S60	-0.3162	3.02 (∼410)
	S66	0.2124	
	S69	0.3696	

states which are mutually exclusive to each set of transitions. In other words, from Tables 4.4 and 4.5, we can see that the set of excited states that can be reached

Table 4.5: Transitions from S9 to higher energy Sn (n>9) and the transition dipole moments.

Lowest CT State (CT_1)	Higher CT State (CT_n)	μ_{tx} (a.u.)	ΔE/eV (nm)
S9	S13	-1.1938	0.39 (∼3180)
	S30	0.2932	1.30 (∼950)
	S31	-0.5346	
	S37	0.7922	1.54 (∼805)
	S52	-0.3681	
	S53	0.2252	1.97(∼630)
	S55	-0.3640	
	S67	0.7169	2.33 (∼530)
	S71	0.1052	

from S1 (the LE state) is different with respect to those that can be reached by S9 (the CT state). This agrees reasonably well with the assumption from experimental data that two families of excited states (LE and CT) are probable and they do not cross their paths. Fig. 4.8 sums up our findings showing the transitions achievable from each state for **CVA07**.

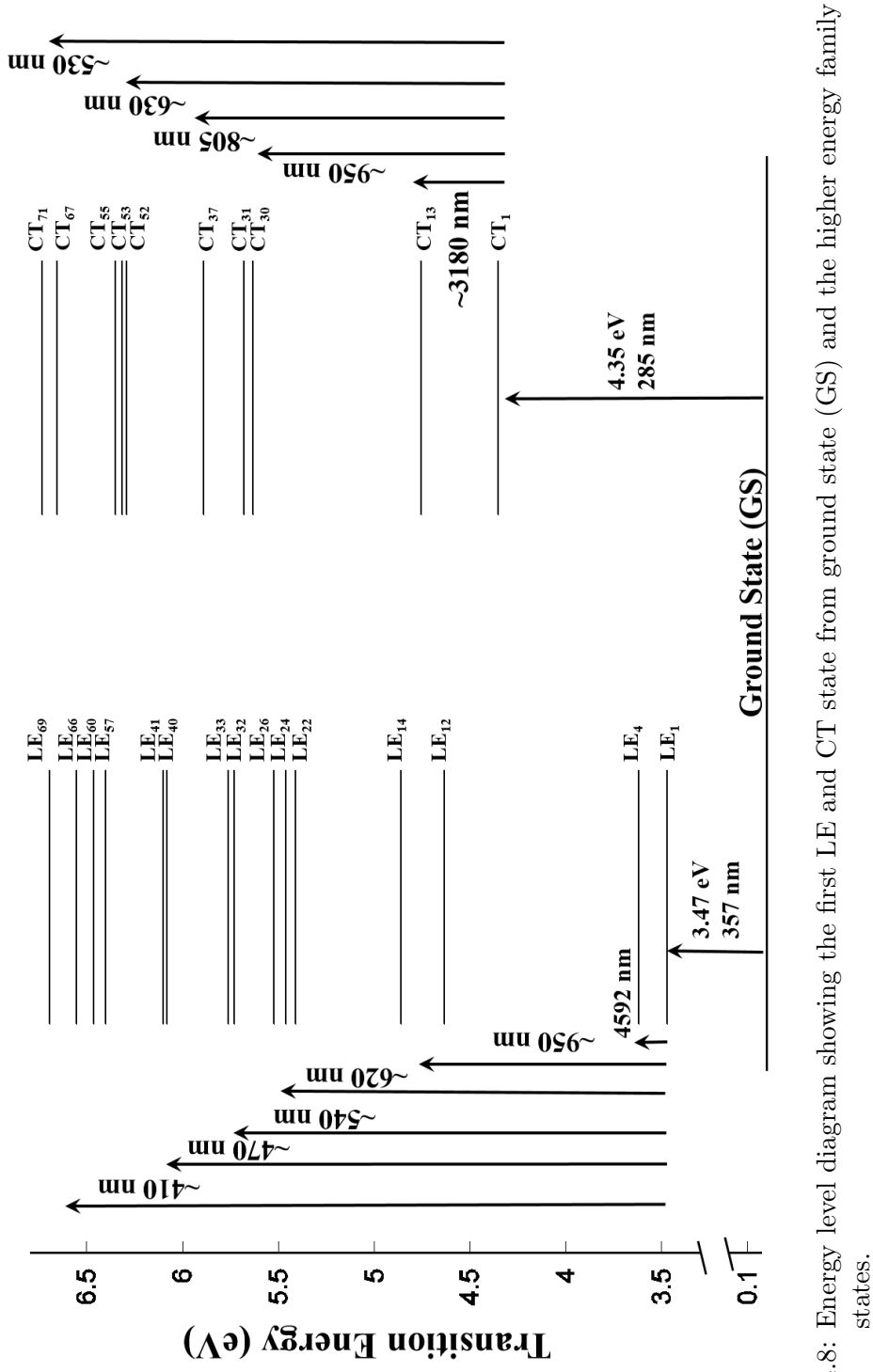

Figure 4.8: Energy level diagram showing the first LE and CT state from ground state (GS) and the higher energy family of states.

4.5 Conclusions

In summary, we have recognized with the help of experimental spectral analysis and theoretical calculations, the LE and the CT lowest-energy states in **CVA07**. The calculated transition dipole moments relevant to all the transitions starting from either of the two have been analyzed and we found that, when starting from the LE state, transitions have non-negligible transition dipole moments only when directed to other LE states. On the other hand, when transitions originate from the CT state, the allowed transitions only lead to other higher-energy CT states. We have therefore recognized two different manifolds of states, having LE or CT nature, not interconverted via optical excitation. However, a spontaneous evolution from LE to the lowest-energy CT state is allowed in polar solvents and is driven by the solvent relaxation itself.

Bibliography

[1] A. Aviram and M. A. Ratner, Chem. Phys. Lett. **29**, 277 (1974).

[2] H. Klauk, *Organic Electronics: Materials, Manufacturing, and Applications* (Wiley-VCH, Weinheim 2006, 2006).

[3] B. Kippelen and J.-L. Brédas, Energy Environ. Sci. **2**, 251 (2009).

[4] F. De Angelis, ACSEnergyLett **1**, 646 (2016).

[5] S. Günes, H. Neugebauer, and N. S. Sariciftci, Chem. Rev. **107**, 1324 (2007).

[6] A. P. Kulkarni, C. J. Tonzola, A. Babel, and S. A. Jenekhe, Chem. Mater. **16**, 4556 (2004).

[7] D. Vonlanthen, J. Rotzler, M. Neuburger, and M. Mayor, Eur. J. Org. Chem. **2010**, 120 (2010).

[8] S. Sasaki, G. P. C. Drummen, and G.-i. Konishi, J. Mater. Chem. C **4**, 2731 (2016).

[9] L. Venkataraman, J. E. Klare, C. Nuckolls, M. S. Hybertsen, and M. L. Steigerwald, Nature **442**, 904 (2006).

[10] I. Minkov, F. Gel'mukhanov, H. Ågren, R. Friedlein, C. Suess, and W. R. Salaneck, J. Phys. Chem. A **109**, 1330 (2005).

[11] M. Maus, W. Rettig, D. Bonafoux, and R. Lapouyade, J. Phys. Chem. A **103**, 3388 (1999).

[12] L. Ventelon, L. Porres, M. H. Blanchard-Desce, Y. Morel, P. L. Baldeck, P. Feneyrou, M. Silly, and P.-A. Chollet, Proc. SPIE **4797**, 15 (2003).

[13] M. J. Frisch, G. W. Trucks, H. B. Schlegel, G. E. Scuseria, M. A. Robb, J. R. Ceseman, G. Scalmani, V. Barone, B. Mennucci, G. A. Petersson, H. Nakatsuji, M. Caricato, X. Li, H. P. Hratchian, A. F. Izmaylov, J. Bloino, G. Zheng, J. L. Sonnenberg, M. Hada, M. Ehara, K. Toyota, R. Fukuda, J. Hasegawa, M. Ishida, T. Nakajima, Y. Honda, O. Kitao, H. Nakai, T. Vreven, J. A. Montgomery, Jr., J. E. Peralta, F. Ogliaro, M. Bearpark, J. J. Heyd, E. Brothers, K. N. Kudin, V. N. Staroverov, R. Kobayashi, J. Normand, K. Raghavachari, A. Rendell, J. C. Burant, S. S. Iyengar, J. Tomasi, M. Cossi, N. Rega, J. M. Millam, M. Klene, J. E. Knox, J. B. Cross, V. Bakken, C. Adamo, J. Jaramillo, R. Gomperts, R. E. Stratmann, O. Yazyev, A. J. Austin, R. Cammi, C. Pomelli, J. W. Ochterski, R. L. Martin, K. Morokuma, V. G. Zakrzewski, G. A. Voth, P. Salvador, J. J. Dannenberg, S. Dapprich, A. D. Daniels, O. Farkas, J. B. Foresman, J. V. Ortiz, J. Cioslowski, and D. J. Fox, "Gaussian 09 Revision D.01," Gaussian Inc. Wallingford CT 2009.

[14] T. Yanai, D. P. Tew, and N. C. Handy, Chem. Phys. Lett. **393**, 51 (2004).

[15] J. Tomasi, B. Mennucci, and R. Cammi, Chem. Rev. **105**, 2999 (2005).

[16] S. L. Adler, Phys. Rev. D **67**, 025007 (2003).

[17] W. Garczyński and K. Urbanowski, *Derivation of the Weisskopf-Wigner Formula from the Królikowski-Rzewuski Equation for Distinguished Component of a State Vector*, Preprint - Instytut Fizyki Teoretycznej Uniwersytetu Wrocławskiego (IFT UW, 1977).

[18] R. Improta, V. Barone, and F. Santoro, Angew. Chem. Int. Ed. **46**, 405 (2007).

[19] D. Jacquemin, A. Planchat, C. Adamo, and B. Mennucci, J. Chem. Theory Comput. **8**, 2359 (2012).

Chapter 5

Finite Size DMRG Study of a Squaraine Dye for calculation of their Optoelectronic Properties

5.1 Introduction

A significant amount of effort has been put into the development of organic molecules and semiconducting quantum dots, having large two-photon absorption (TPA) cross-section, for their application in the field of fluorescence sensing, bio-imaging [1], two-photon imaging [2], photovoltaic cells [3–5], photodynamic therapy [6] amongst many others [7–11]. The organic molecules, which possess the capacity to tailor their linear and non-linear optical responses on account of molecular modification, are important for the applications mentioned. Squaraines dyes have a strong acceptor group squaraic acid (diketocyclobutenediol), placed mid-way in a vinylene chain. These chromophores exhibit large TPA cross-sections, reported upto 33,000 GM [12] owing to the presence of a large ground-to-first excited state transition dipole moment, near-parallel orientation of their ground-to-first excited

and between-excited states transition dipole moments, and the sharply rising low-energy side of their linear absorption that makes room for significant intermediate-state resonance enhancement of the TPA [13–18]. Squaraines fall into Class II donor-acceptor-donor or DAD dyes where the localization of the positive charge on the nitrogen atom and the negative charge on the oxygen atom of the central group were confirmed by quantum chemical calculations way back in the beginning of this millenium [18]. The introduction of the terminal donor to a DA chromophore leads to a blue-shift in the one-photon absorption (OPA) band in these dyes, and the TPA peak is strongly blue-shifted relative to twice the OPA, which allows imaging at lower excitation wavelengths, improving resolution and facilitating co-excitation with spectrally unique fluorophores. The difference in the TPA cross-sections of DAD with respect to DA dyes can be explained on the basis of intermediate state resonance enhancement (ISRE), which calls for the narrowing of the OPA main transition band and increase in density of final states [19, 20].

A squaraine dye, named as SD#2243 [13, 18–20] (hereafter referred in this chapter as SQ2) is a widely studied dye and synthesized at the Institute of Organic Chemistry, Kiev, Ukraine and has the IUPAC nomenclature 1,3-Bis-[(1,3-dihydro-1-butyl-3,3-dimetyl-2Hbenzo[e]indol-2-ylidene)methyl]squaraine (Fig. 5.1). Since their first synthesis, squaraine dyes have been of great interest not only for experimentalists, but also for theoreticians. The experimental techniques used for the measurement of SQ2 have been (1) Z-scan, (2) femtosecond pump-probe, (3) steady-state excitation anisotropy measurements, and (4) linear absorption spectral measurements [18]. SD#2243 is a symmetrical squaraine molecule which shows a strong OPA peak at the characteristic long wavelength region of squaraines at 668 nm [13], while the strong TPA transition is observed at 375 nm having a very high TPA cross-section ($\sigma_{TPA} = 8660$ GM). From the aspect of theoretical studies, researchers have carried out extensive works using semi-emperical computational methods like Austin Model 1 (AM1) for geometries and ZINDO for electronic transition energies [13, 18], PPP models without assumptions, Essential State Model studies [10, 14, 21] to Time Dependent Density Functional Theory (TDDFT) [22]. Various studies have been done to address the electronic structure of symmetric and asymmetric squaraine dyes [23–25], but many failures of TDDFT have been noted in offering unreliable description of the excitation spectrum of various squaraine

dyes, which can be attributed to the biradical character of low-lying excitations in squaraines [22].

In this chapter, we have undertaken the studies of optoelectronic properties of SQ2 molecule using symmetrized Density Matrix Renormalization Group (DMRG) theory [26–28] within Pariser-Parr-Pople (PPP) Hamiltonian with Ohno parameterization scheme[29–31], which takes into account long-range Coulomb interactions. The low-lying excited states and NLO response of conjugated networks are basically associated with delocalized electrons. The PPP model for interacting electrons has thus provided a unified, convinient and *ab*-initio approach for describing excited states. We have modeled the system by susbtituting the butyl chains in SD#2243 with ethyl group and keeping all other sites same. Many previous works have been done with DMRG to study TPA in expanded porphyrins [32], porphyrins [33], stilbene and azobenzene systems [34], and has been shown that for biphenyl DA chromophore TPA value can be conformationally tuned [35]. We have carried out a systematic analysis of the linear and non-linear properties of SQ2 dye and several ground state and excited state properties. We will proceed with a brief introduction to the methodology in the next section, followed by results and discussions.

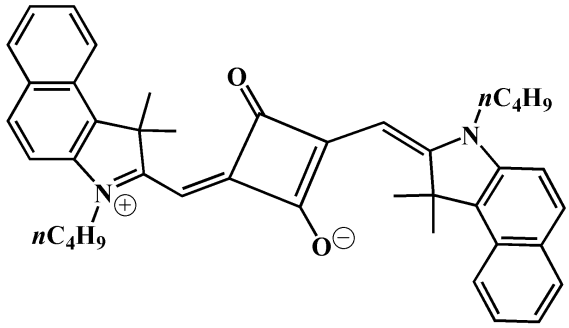

Figure 5.1: The squaraine dye under study SD#2243.

5.2 Methodology

We have assumed here single p_z electron for each of the conjugated carbon sites (2 p_z electrons in pyrolitic nitrogen). We have considered the following PPP Hamiltonian. The total number of π electrons and z-component of the total magnetic spin

are the good quantum numbers, as they commute with the PPP Hamiltonian[36].

$$\begin{aligned}\mathcal{H} = &\sum_{\langle i,j\rangle\sigma} t_{ij}\left(a^{\dagger}_{i\sigma}a_{j\sigma} + a^{\dagger}_{j\sigma}a_{i\sigma}\right) + \sum_{i}\epsilon_i n_i \\ &+ \frac{1}{2}\sum_{i} U_i n_i\left(n_i - 1\right) + \sum_{i,j} V_{ij}\left(n_i - z_i\right)\left(n_j - z_j\right)\end{aligned} \tag{5.1}$$

The t_{ij} term in the Hamiltonian stands for the resonance or hopping/transfer integrals between bonded sites i and j, ϵ_i refers to the orbital or site energy of the p_z orbital on the ith atom (N and C), while U_is are the Hubbard repulsion terms at site i. $a^{\dagger}_{i\sigma}$ and $a_{i\sigma}$ are the creation and annihilation operators, respectively, of an electron of spin σ at the ith atom, n_i is the number operator and z_i is the chemical potential of ith site. V_{ij} is the nearest neighbour interaction given by the Ohno parameterization (discussed in Section 1.3.6.3), and the value interpolates between U_i for $r_{ij} = 0$ and e^2/r_{ij} when $r_{ij} \to \infty$. In this work, we have set t_{ij} = -2.40 eV for all bonded sites C-C and C-N. The site energy ϵ_i is taken as 0.0 eV for all other C atoms, except the site (site 10) having two methyl groups which has +2.0 eV, for the pyrrole nitrogen as -1.0 eV (N is attached to ethyl group and as a result the effective value is taken for N), while for the carbonyl C (-C=0) of the squaraic acid moiety has ϵ_i = -1.0 eV. The site energies (ϵ_i) have been assigned on the basis of Mulliken charge density obtained from Gaussian09 for SQ2 moiety. We have taken the Hubbard U for the C atoms as 11.26 eV, while for N atoms is 14.53 eV. The pyrrolic N atom has double occupancy ($z_i = 2$), while all the C atoms have single occupancy ($z_i = 1$). To calculate the r_{ij} for intersite electron-electron interaction potentials, we have optimised the geometry of SQ2 using Gaussian09 [37] suite of programs within Density Functional Theory (DFT), at CAMB3LYP/6-31+g(d) level of theory.

In DMRG method (as has also been discussed in Chapter 1), we typically start with a four site system, with each atom having one orbital that participates in conjugation. From an exact solution of the small system, density matrix is obtained for one-half of the system.

Then two additional sites are added between the two half-blocks and the Hamiltonian is constructed based on the direct product of the eigenvectors of the density matrix and Fock states of two new sites and the process is repeated till the final size

of the system is obtained. To span the Fock space of the system, in every DMRG iteration, a small number of eigenvectors (m) of the density matrix with largest eigenvalues is chosen. Here we have a total of 32 sites (see Fig. 5.2), which means the density matrix is obtained for 16 sites.

After this, we carry out finite size DMRG runs, which involves sweeping over the sites, where the system block is increased in size with the decrease of the environment block and the process is repeated by interchanging environment and system block. With the use of Finite system DMRG, the accuracy of the results is enhanced. Fig. 5.2 shows the building up of the molecule, starting from a 4 site system. For our calculations, we have kept $m = 340$. The system possesses an inversion symmetry (i). In this technique, the system evolves from the external C atoms of SQ2, and the introduction of the new sites in the middle is more accurate compared to the procedure that builds the system starting from the middle. The reason for this can be attributed to the fact that we have to rebuild the central bonds each time and the repeated renormalization of the operators at the new site reduces the accuracy of the procedure. In addition, the inside-out procedure does not introduce interactions between the new sites and thus the density matrix of the half-blocks cannot be good representatives of the density matrix of the half-block of the actual system [38].

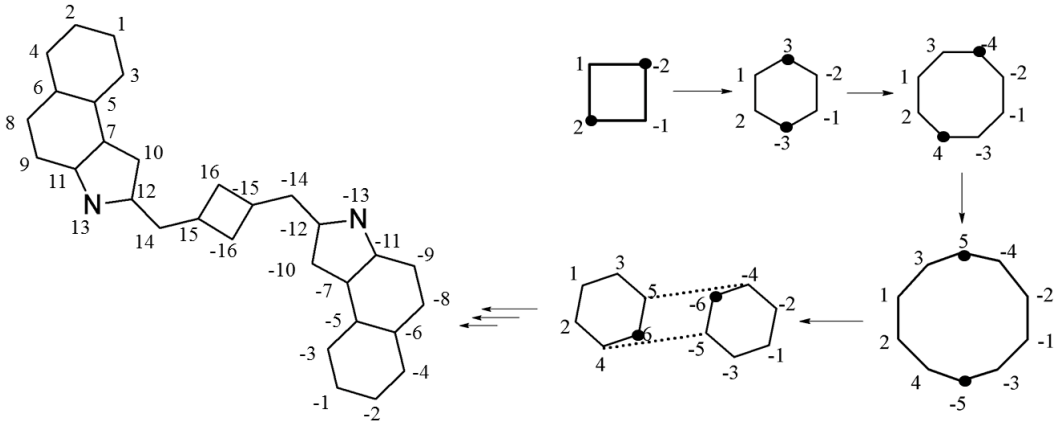

Figure 5.2: Schematic diagram showing the building-up of SQ2 from a 4 site system. Black circles indicate new additional sites added in each iteration of Infinite DMRG. Positive site number refers to one block or Left block, while negative numbers refer to another block or Right block.

Further, we calculated the eigenvalues and eigenvectors for 500 low-lying excited

states. The eigenvectors are used to calculate the bond orders, charge densities and spin densities for the ground state. Since, with this m value, the energy difference between total Sz=0 and total Sz=1 is very small, we have carried out the calculations for lowest energy states in both the spin states, Sz=0 and Sz=1.

5.3 Results and Discussions

We have a 32 site system here (Fig 5.2) and we have taken one π-electron on each C atom, while the pyrrole nitrogen in the 13th site (and the corresponding site in the right block) has double occupancy, as mentioned already, since it contributes a lone pair to the π-electron system. This makes the total number of electrons in the system as 34. Since the molecule is symmetric and has an inversion centre i, we have calculated the properties like bond order, charge density and spin density for half of the molecule. DMRG results shown here are for an isolated molecule in the lowest energy state geometry. We have calculated the spin gap energy of two spin spaces Sz=0 and Sz=1, and Sz=1 has lower energy compared to Sz=0 by 0.00006 eV (within m value of 340; energy of Sz=0 is -84.30568 eV and energy of Sz=1 is -84.30574 eV), making the ground state of SQ2 having a triplet spin multiplicity. The close proximity of singlet and triplet states in ground states ($\Delta E = 6x10^{-5}$ eV) are in line with the large biradicaloid character of squaraine ground state, as discussed by Yesudas [24]. Results with different models have been summarized in Table 5.1. Although spin triplet state is slightly lower in energy than spin singlet state, such result can be rationalized if we check the spin parity (see Fig. 5.3) for one-half of the molecule, considering antiferromagnetic spin configuration (which is the case here, according to spin-spin correlations). Pyrrole nitrogen atom site has two π electrons (lone pair) holding a key factor, as mentioned before, and all the sites otherwise have paired-up spins, except for the carbonyl (-C=O) C atom at site 16 which is left with an extra unpaired electron.

Similarly, for the other-half of SQ2, one unpaired spin remains at site -16, thereby the spin multiplicity becomes $2S + 1 = 3$. This can be ascribed due to pyrrole N atom, whose two p_z electrons take part in the conjugation, and thereby an unpaired electron remains for one-half of the molecule. The triplet consists of three subspaces with spin components +1, 0 and 1 along the direction of the total

Table 5.1: Ground state energy for Sz=0 and Sz=1 using Hubbard, Hückel and PPP Models.

Hubbard Model		Huckel Model		PPP Model	
$E_{Sz=0}$ (eV)	$E_{Sz=1}$ (eV)	$E_{Sz=0}$ (eV)	$E_{Sz=1}$ (eV)	$E_{Sz=0}$ (eV)	$E_{Sz=1}$ (eV)
-37.51647	-37.51659	-101.39858	-105.75545	-84.30568	-84.30574

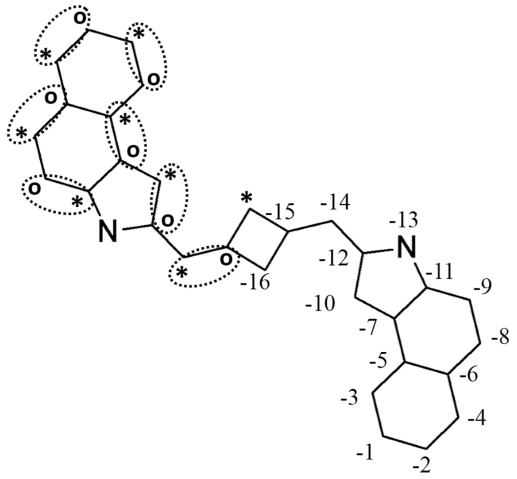

Figure 5.3: Schematic diagram showing the spin pairing for one-half of SQ2. $*$ indicates spin-up and black open circle (**o**) indicates spin-down. The dashed circle shows the spin pairing.

spin angular momentum, which is 1.

5.3.1 Ground State Bond Orders and Charge Density Analysis

To understand the structure of the ground state, we have calculated bond orders and charge density values for half the molecule in each of the lowest energy state in two spin manifold (states). In Fig. 5.4, we have shown the charge densities at each site and the bond orders for individual bonds. Since lowest energy states in Sz=0 and Sz=1 differ only by spin moment value, charge densities and bond orders remain the same up to the fifth decimal places pointing to the biradicaloid nature of the SQ2 ground state (see Fig. 5.4).

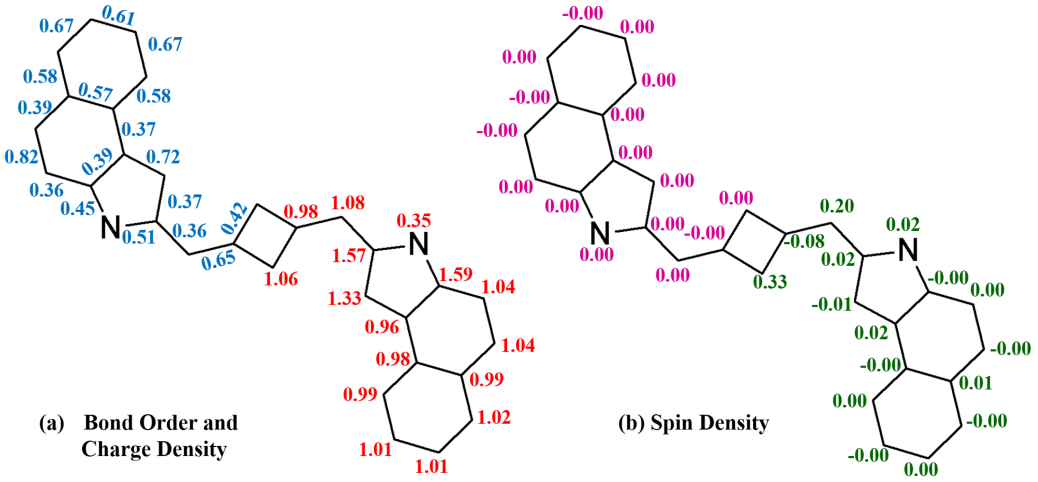

Figure 5.4: Panel (a) shows the charge density at each site (red numbers) and bond orders for each bond (blue numbers) for both Sz=0 and Sz=1. Panel (b) shows the spin density at each site, upper half of the molecule (in magenta colour) shows for Sz=0 and lower half of the molecule (in green colour) shows for Sz=1.

In each of lowest energy states, the charge density on the C at i=10 is higher, due to the +I effect of the two methyl groups attached to the C atom, while the charge density of the pyrrole N (at i=13) is low. The charge density in all the other carbon atoms is 1.00±0.04, except C in sites 11 and 12, nearest neighbours of the N, where the charge density is comparatively higher. We can also see a pattern of alternating double and single bonds in the benzene rings, with bonds like $C_1 - C_3$, $C_2 - C_4$, $C_5 - C_6$, $C_8 - C_9$ having a double bond character (BO $>$ 0.6), while, $C_5 - C_7$, $C_6 - C_8$, $C_7 - C_{11}$, $C_9 - C_{11}$, $C_{10} - C_{12}$, $C_{12} - C_{14}$ bonds have single bond character. From the BO values of $C_{11} - N_{13}$ and $C_{12} - N_{13}$ in the pyrrole ring, they are in between the double and single bond order, and possibly we can say, there is a delocalized double bond character, where the two π electrons on N atom take part in conjugation, while $C_7 - N_{10}$ has a double bond character. In the central square moiety, $C_{15} - C_{16}$, where 16th site has the carbonyl group, has a predominantly single bond character, indicating that the ground state of SQ2 has a keto form, instead of the tautomeric enol form.

Since the energy values for the lowest energy states of Sz=0 and Sz=1 spin manifold are too close, we are currently doing DMRG caculations with larger max values. Thereafter, we will do spectroscopic calculations to find optical gaps, one

and two photon spectra, absorption coefficients and the TPA cross sections.

5.4 Conclusions

Summarizing, we have employed the symmetrized finite size DMRG method of calculations for studying the low lying energy spectra and linear and nonlinear optical properties of a well-studied squaraine dye SD#2243 within the framework PPP model to describe its interacting π-electrons. We also have calculated the charge densities in each site and the bond orders in the lowest energy states of Sz=0 and Sz=1 spin manifold. Further, we are calculating keeping higher DMRG states to analyse and to find the true ground state and thereafter calculating linear and nonlinear optical spectra, the OPA and TPA coeffcients and their cross sections and figure of merit for this molecule.

Bibliography

[1] K. Podgorski, E. Terpetschnig, O. P. Klochko, O. Obukhova, and K. Haas, PLoS ONE **7(12)**, e51980 (2012).

[2] S. Sreejith, P. Carol, P. Chithra, and A. Ajayaghosh, J. Mater. Chem. **18**, 264 (2008).

[3] G. Chen, H. Sasabe, Y. Sasaki, H. Katagiri, X.-F. Wang, T. Sano, Z. Hong, Y. Yang, and J. Kido, Chem. Mater. **26**, 1356 (2014).

[4] G. Chen, H. Sasabe, T. Igarashi, Z. Hong, and J. Kido, J. Mater. Chem. A **3**, 14517 (2015).

[5] F. M. Jradi, X. Kang, D. O'Neil, G. Pajares, Y. A. Getmanenko, P. Szymanski, T. C. Parker, M. A. El-Sayed, and S. R. Marder, Chem. Mater. **27**, 2480 (2015).

[6] D. Ramaiah, I. Eckert, K. T. Arun, L. Weidenfeller, and B. Epe, Photochem. Photobiol. **76**, 672 (2002).

[7] S. R. Marder, Chem. Commun. , 130 (2006).

[8] M. Rumi and J. W. Perry, Adv. Opt. Photon. **2**, 451 (2010).

[9] B. Strehmel and V. Strehmel, "Two-photon physical, organic, and polymer chemistry: Theory, techniques, chromophore design, and applications," in *Advances in Photochemistry* (John Wiley & Sons, Inc., 2005) pp. 111–354.

[10] K. M. Shafeekh, S. Das, C. Sissa, and A. Painelli, J. Phys. Chem. B **117**, 8536 (2013).

[11] G. Xia and H. Wang, Journal of Photochemistry and Photobiology C: Photochemistry Reviews **31**, 84 (2017).

[12] S.-J. Chung, S. Zheng, T. Odani, L. Beverina, J. Fu, L. A. Padilha, A. Biesso, J. M. Hales, X. Zhan, K. Schmidt, A. Ye, E. Zojer, S. Barlow, D. J. Hagan, E. W. Van Stryland, Y. Yi, Z. Shuai, G. A. Pagani, J.-L. Brdas, J. W. Perry, and S. R. Marder, J. Am. Chem. Soc. **128**, 14444 (2006).

[13] J. Fu, L. A. Padilha, D. J. Hagan, E. W. V. Stryland, O. V. Przhonska, M. V. Bondar, Y. L. Slominsky, and A. D. Kachkovski, J. Opt. Soc. Am. B **24**, 67 (2007).

[14] F. Terenziani, A. Painelli, C. Katan, M. Charlot, and M. Blanchard-Desce, J. Am. Chem. Soc. **128**, 15755 (2006).

[15] M. Albota, D. Beljonne, J.-L. Brédas, J. E. Ehrlich, J.-Y. Fu, A. A. Heikal, S. E. Hess, T. Kogej, M. D. Levin, S. R. Marder, D. McCord-Maughon, J. W. Perry, H. Röckel, M. Rumi, G. Subramaniam, W. W. Webb, X.-L. Wu, and C. Xu, Science **281**, 1653 (1998).

[16] B. Patrick, M. V. George, P. V. Kamat, S. Das, and K. G. Thomas, J. Chem. Soc., Faraday Trans. **88**, 671 (1992).

[17] D. Scherer, R. Dörfler, A. Feldner, T. Vogtmann, M. Schwoerer, U. Lawrentz, W. Grahn, and C. Lambert, Chem. Phys. **279**, 179 (2002).

[18] R. A. Negres, O. V. Przhonska, D. J. Hagan, E. W. V. Stryland, M. V. Bondar, Y. L. Slominsky, and A. D. Kachkovski, IEEE Journal of Selected Topics in Quantum Electronics **7**, 849 (2001).

[19] O. V. Przhonska, S. Webster, L. A. Padilha, H. Hu, A. D. Kachkovski, D. J. Hagan, and E. W. Van Stryland, "Two-photon absorption in near-ir conjugated molecules: Design strategy and structure–property relations," in *Advanced Fluorescence Reporters in Chemistry and Biology I: Fundamentals and Molecular Design*, edited by A. P. Demchenko (Springer Berlin Heidelberg, Berlin, Heidelberg, 2010) pp. 105–147.

[20] S. Webster, J. Fu, L. A. Padilha, O. V. Przhonska, D. J. Hagan, E. W. Van Stryland, M. Bondar, Y. L. Slominsky, and A. D. Kachkovski, Chem. Phys. **348**, 143 (2008).

[21] S. Sanyal, A. Painelli, S. K. Pati, F. Terenziani, and C. Sissa, Phys. Chem. Chem. Phys. **18**, 28198 (2016).

[22] A. Dreuw and M. Head-Gordon, J. Am. Chem. Soc. **126**, 4007 (2004).

[23] F. Meyers, C.-T. Chen, S. R. Marder, J.-L. Brédas, and F. Meyers, Chem. Eur. J. **3**, 530 (1997).

[24] C. Prabhakar, K. Yesudas, G. Krishna Chaitanya, S. Sitha, K. Bhanuprakash, and V. J. Rao, J. Phys. Chem. A **109**, 8604 (2005).

[25] K. Yesudas, G. K. Chaitanya, C. Prabhakar, K. Bhanuprakash, and V. J. Rao, J. Phys. Chem. A **110**, 11717 (2006).

[26] S. R. White, Phys. Rev. Lett. **69**, 2863 (1992).

[27] S. R. White, Phys. Rev. B **48**, 10345 (1993).

[28] S. K. Pati, S. Ramasesha, Z. Shuai, and J. L. Brédas, Phys. Rev. B **59**, 14827 (1999).

[29] R. Pariser and R. Parr, J. Chem. Phys. **21**, 466 (1953).

[30] J. A. Pople, J. Chem. Soc. Faraday Trans. **49**, 1375 (1953).

[31] K. Ohno, Theoret. Chim. Acta **2**, 219 (1964).

[32] S. Thomas, Y. A. Pati, and S. Ramasesha, J. Phys. Chem. A **117**, 7804 (2013).

[33] M. Kumar, Y. A. Pati, and S. Ramasesha, J. Chem. Phys. **136**, 014112 (2012).

[34] P. C. Jha, Y. A. Pati, and S. Ramasesha, Molecular Physics **103**, 1859 (2005).

[35] S. K. Pati, T. J. Marks, and M. A. Ratner, J. Am. Chem. Soc. **123**, 7287 (2001).

[36] Z. G. Soos and S. Ramasesha, J. Chem. Phys. **90**, 1067 (1989).

[37] M. J. Frisch, G. W. Trucks, H. B. Schlegel, G. E. Scuseria, M. A. Robb, J. R. Ceseman, G. Scalmani, V. Barone, B. Mennucci, G. A. Petersson, H. Nakatsuji, M. Caricato, X. Li, H. P. Hratchian, A. F. Izmaylov, J. Bloino, G. Zheng, J. L. Sonnenberg, M. Hada, M. Ehara, K. Toyota, R. Fukuda, J. Hasegawa, M. Ishida, T. Nakajima, Y. Honda, O. Kitao, H. Nakai, T. Vreven, J. A. Montgomery, Jr., J. E. Peralta, F. Ogliaro, M. Bearpark, J. J. Heyd, E. Brothers, K. N. Kudin, V. N. Staroverov, R. Kobayashi, J. Normand, K. Raghavachari, A. Rendell, J. C. Burant, S. S. Iyengar, J. Tomasi, M. Cossi, N. Rega, J. M. Millam, M. Klene, J. E. Knox, J. B. Cross, V. Bakken, C. Adamo, J. Jaramillo, R. Gomperts, R. E. Stratmann, O. Yazyev, A. J. Austin, R. Cammi, C. Pomelli, J. W. Ochterski, R. L. Martin, K. Morokuma, V. G. Zakrzewski, G. A. Voth, P. Salvador, J. J. Dannenberg, S. Dapprich, A. D. Daniels, O. Farkas, J. B. Foresman, J. V. Ortiz, J. Cioslowski, and D. J. Fox, "Gaussian 09 Revision D.01," Gaussian Inc. Wallingford CT 2009.

[38] Y. Anusooya, S. K. Pati, and S. Ramasesha, J. Chem. Phys. **106**, 10230 (1997).

Chapter 6

Summary And Perspectives

An extensive modeling effort has been presented to extract the main physics governing linear and non-linear optical spectra of organic dyes and of their aggregates, focusing attention on two class of chromophores, namely dipolar and quadrupolar dyes. We have combined the Essential State Models and first principles calculations to address isolated chromophores and further moving on to the aggregation properties of dyes for their applications in the vast area of non-linear optical research.

In case of the quadrupolar chromophores studied, namely curcumin and squaraine, we have validated the essential state models, a family of parametric Hamiltonians, developed in the host laboratory over the past two decades, against TDDFT calculations for the monomer and dimer systems of a curcuminoid dye. As previously documented in the literature, TDDFT offers unreliable results for Squaraine dyes, due to the biradicaloid nature of its ground state. However, validation of ESM curcumin-analogues has enabled us to address the large aggregates of these extended π systems to understand their properties, accounting fully for the polarizability of these molecules and relaxing the point dipole approximation. Different geometries of one-dimensional aggregates have been taken into account, and we have successfully demonstrated that the intriguing observation of "non-fluorescent J-aggregation" calls for explanations beyond Exciton Model. Another important point that we came across is, for highly polarizable molecular systems, like squaraine dyes, the

usual definition of *H*- and *J*-aggregation is misleading and that large-aggregation effects are expected in TPA spectra.

We also studied two interesting molecules. We have modeled a well-studied squaraine dye using symmetrized Finite Size DMRG method of calculations within the framework Pariser-Parr-Pople model, with the aim of studying its optoelectronic properties. Preliminary results confirm the presence very closely spaced ground state energies for Sz=0 and Sz=1 spin manifold, which goes in line with the earlier proposed biradicaloid character in ground state of squaraines, and our spin density and charge density calculations for Sz=0 and Sz=1. Further studies are needed to analyze the linear and non-linear spectral properties using DMRG. In an other study, in close collaboration with experimentalists, a dipolar chromophore based on a biphenyl core was studied. An extensive ZINDO analysis of higly excited states in this dye confirmed the hypothesis, introduced to rationalize experimental data, of the presence of two families of excited states, local-excited states and charge transfer states that are non-interconvertible via optical excitations.

In the class of dipolar chromophores, we have studied the collective amplification in second order NLO response (or β) of a well known CT dye, DANS, in an aligned geometry. A bottom-up modeling strategy is exploited with the definition of a reliable ESM for the DANS molecules, based on an extensive analysis of its solution spectra. This information is then used to build models for interacting dyes in the aggregate, exploiting DFT studies to estimate intermolecular electrostatic interactions. Large cooperative and collective effects are proved in the aggregate, leading to a superlinear dependence of the β-response on the number of aligned molecules inside the aggregate aligned with a neutral ground state, considering the fact that these dyes do interact with each other. This leads to a large renormalization on the estimate of the number of aligned dyes in the experimental system (from ~ 70 to ~ 7). The more general and more important result however is, the suggestion offered to experimentalists that to achieve large second order NLO response it is enough to align just a few dyes, without the need to arrange a large number of them in a ordered way.

Appendix A

Appendix A

A.1 TDDFT Results and FMOs

As discussed in Chapter 2, the intermolecular distance in case of the equivalent BFC dimer configuration (P-P) and the inequivalent dimer (T-P) structures were increased by 1 Å in each step to estimate the energies of the four exciton states. Here we present the detailed results for the Time Dependent Density Functional Theory (TDDFT) calculations, and their Frontier Molecular Orbital (FMO) plots, done at each increment. The calculations have been carried out at the same level of theory, as discussed in Section 2.2.

A.1.1 For P-P dimer

1. P-P at 4.74 Å in Gasphase

Table A.1: TDDFT Calculations for BFC P-P dimers at 4.74 Å

Transitions	Transition Energy(eV)	Oscillator Strength	Nature of Transitions
S0→S1 (C_1)	3.13 eV	0.0000	H-1→L+1 (38%) $c_a - c_b$ CT H→L (51%) $c_a - c_b$ CT
S0→S2 (C_2)	3.36 eV	3.9797	H-1→L (42%) $c_a + c_b$ CT H→L+1 (46%) $c_a + c_b$ CT
S0→S3	3.89 eV	0.0062	H-1→L (42%) $c_a + c_b$ CT H→L+1 (33%) $c_a + c_b$ CT
S0→S4	3.90 eV	0.0015	H-1→L+1 (46%) $c_a - c_b$ CT H→L (31%) $c_a - c_b$ CT
S0→S5 (E_1)	4.01 eV	0.1308	H-3→L+1 (38%) $e_a - e_b$ CT H-2→L (45%) $e_a - e_b$ CT
S0→S6 (E_2)	4.12 eV	0.0000	H-3→L (44%) $e_a + e_b$ CT H-2→L+1 (46%) $e_a + e_b$ CT

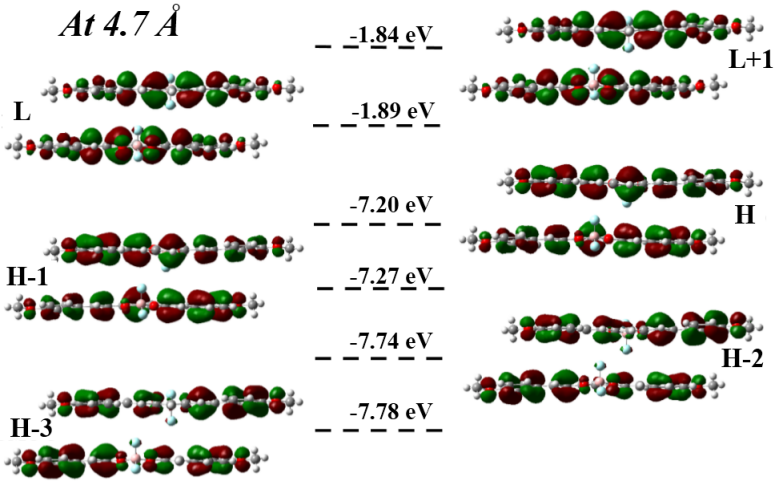

Figure A.1: FMO plots of TDDFT results for P-P curcumin dimer at distance 4.74 Å

2. P-P at 5.74 Å in Gasphase

Table A.2: TDDFT Calculations for BFC P-P dimers at 5.74 Å

Transitions	Transition Energy(eV)	Oscillator Strength	Nature of Transitions
S0→S1 (C_1)	3.17 eV	0.0001	H-1→L+1 (41%) $c_a - c_b$ CT H→L (43%) $c_a - c_b$ CT
S0→S2 (C_2)	3.35 eV	4.0191	H-1→L (44%) $c_a + c_b$ CT H→L+1 (45%) $c_a + c_b$ CT
S0→S3 (E_1)	4.04 eV	0.1431	H-3→L+1 (39%) $e_a - e_b$ CT H-2→L (42%) $e_a - e_b$ CT
S0→S4	4.11 eV	0.0001	H-1→L (23%) $c_a + c_b$ CT H→L (36%) $c_a - c_b$ CT
S0→S5 (E_2)	4.11 eV	0.0000	H-3→L (40%) $e_a + e_b$ CT H-2→L+1 (42%) $e_a + e_b$ CT
S0→S6	4.12 eV	0.0001	H-1→L+1 (39%) $c_a - c_b$ CT H→L+1 (23%) $c_a + c_b$ CT

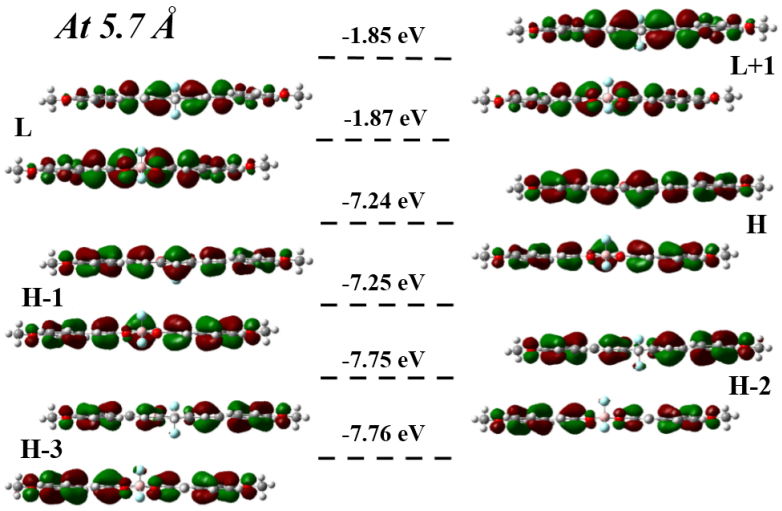

Figure A.2: FMO plots of TDDFT results for P-P curcumin dimer at distance 5.74 Å

3. P-P at 7.74 Å in Gasphase

Table A.3: TDDFT Calculations for BFC P-P dimers at 7.74 Å

Transitions	Transition Energy(eV)	Oscillator Strength	Nature of Transitions
S0→S1 (C_1)	3.21 eV	0.0002	H-1→L (46%) c_a H→L+1 (44%) c_b
S0→S2 (C_2)	3.33 eV	4.0717	H-1→L (44%) c_a H→L+1 (46%) c_b
S0→S3 (E_1)	4.06 eV	0.1537	H-3→L (46%) e_a H-2→L+1 (43%) e_b
S0→S4 (E_2)	4.10 eV	0.0000	H-3→L (43%) e_a H-2→L+1 (47%) e_b
S0→S5	4.39 eV	0.0000	H→L (98%) CT
S0→S6	4.40 eV	0.0000	H-1→L+1 (98%) CT

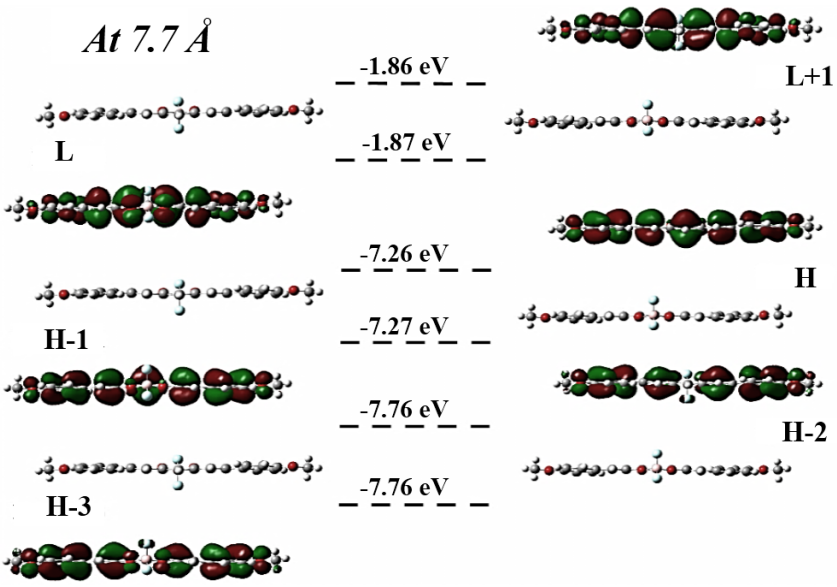

Figure A.3: FMO plots of TDDFT results for P-P curcumin dimer at distance 7.74 Å

A.1.2 For T-P dimer

1. T-P at 3.3 Å in Gasphase

Table A.4: TDDFT Calculations for BFC T-P dimers at 3.3 Å

Transitions	Transition Energy(eV)	Oscillator Strength	Nature of Transitions	TPA Energy(eV)	σ_2 (GM)
S0→S1 (C_1)	2.91 eV	0.0113	H→L (81%) $c_a - c_b$ CT	2.91	23.5
S0→S2 (C_2)	3.39 eV	3.6025	H→L+1 (62%) $c_a + c_b$ CT	3.39	0.813
S0→S3	3.56 eV	0.2806	H-1→L (66%) $c_a + c_b$ CT	3.56	3.20
S0→S4	3.78 eV	0.0114	H-1→L+1 (73%) $c_a - c_b$ CT	3.78	9.84
S0→S5 (E_1)	3.91 eV	0.0950	H-2→L (57%) $e_a - e_b$ CT	3.91	10.1
S0→S6 (E_2)	4.12 eV	0.0071	H-3→L (49%) $e_a + e_b$ CT H-2→L+1 (38%) $e_a + e_b$ CT	4.12	2530

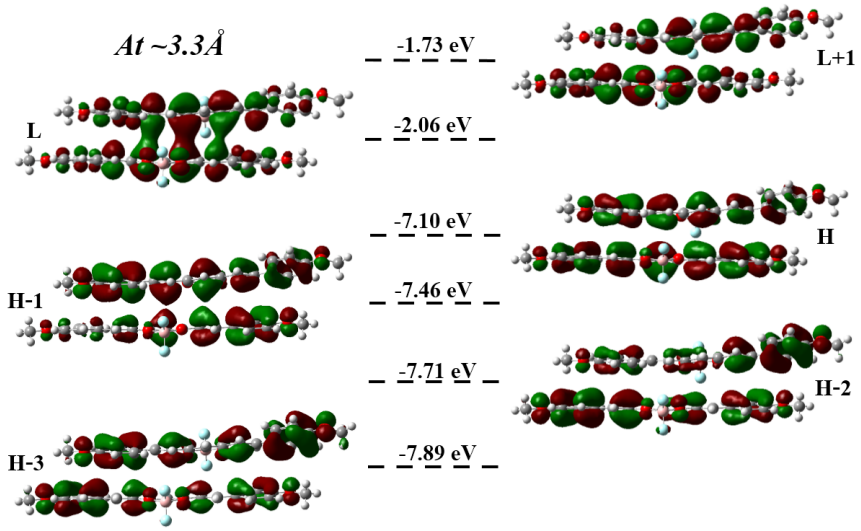

Figure A.4: FMO plots of TDDFT results for T-P curcumin dimer at distance 3.3 Å

2. T-P at 4.3 Å in Gasphase

Table A.5: TDDFT Calculations for BFC T-P dimers at 4.3 Å

Transitions	Transition Energy(eV)	Oscillator Strength	Nature of Transitions
S0→S1 (C_1)	3.15 eV	0.0554	H-1→L (17%) c_a H→L (30%) CT H→L+1 (29%) c_b
S0→S2 (C_2)	3.40 eV	3.8751	H-1→L (49%) c_a H→L+1 (38%) c_b
S0→S3	3.83 eV	0.0031	H→L (62%) CT H→L+1 (19%) c_b
S0→S4	3.99 eV	0.0397	H-1→L+1 (53%) CT
S0→S5 (E_1)	4.04 eV	0.1073	H-3→L+1 (21%) H-2→L (19%) CT H-2→L+1 (18%) e_b H-1→L+1 (19%) CT
S0→S6 (E_2)	4.13 eV	0.0091	H-3→L (49%) e_a H-2→L+1 (38%) e_b

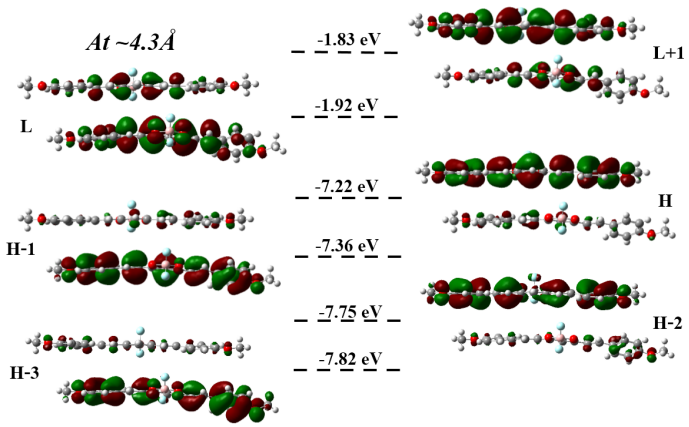

Figure A.5: FMO plots of TDDFT results for T-P curcumin dimer at distance 4.3 Å

3. T-P at 5.3 Å in Gasphase

Table A.6: TDDFT Calculations for BFC T-P dimers at 5.3 Å

Transitions	Transition Energy(eV)	Oscillator Strength	Nature of Transitions
S0→S1 (C_1)	3.20 eV	0.1023	H-1→L (30%) c_a H→L+1 (56%) c_b
S0→S2 (C_2)	3.39 eV	3.8651	H-1→L (58%) c_a H→L+1 (32%) c_b
S0→S3	4.04 eV	0.0107	H→L (86%) CT
S0→S4 (E_1)	4.05 eV	0.1431	H-3→L (29%) e_a H-2→L+1 (51%) e_b
S0→S5 (E_2)	4.13 eV	0.0122	H-3→L (57%) e_a H-2→L+1 (33%) e_b
S0→S6	4.22 eV	0.0001	H-1→L+1 (91%) CT

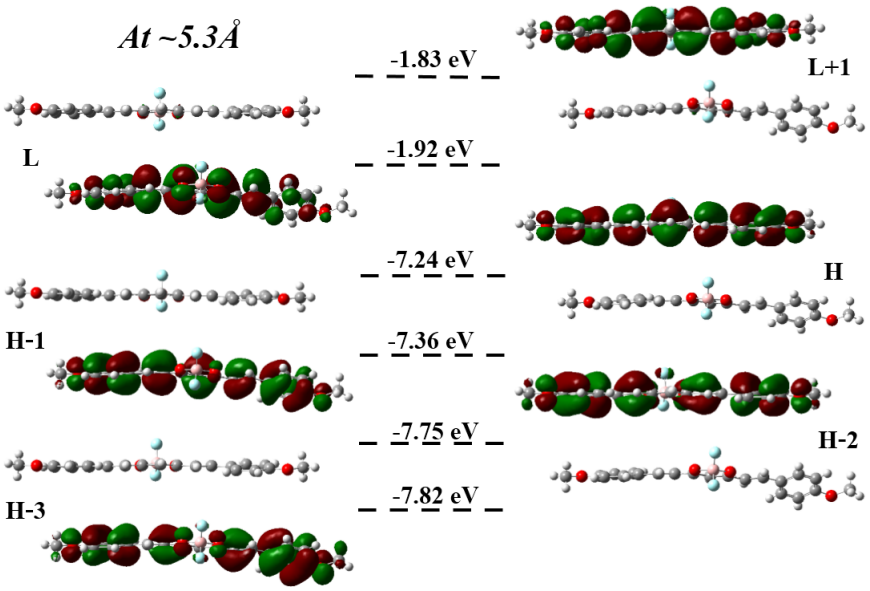

Figure A.6: FMO plots of TDDFT results for T-P curcumin dimer at distance 5.3 Å

4. T-P at 6.3 Å in Gasphase

Table A.7: TDDFT Calculations for BFC T-P dimers at 6.3 Å

Transitions	Transition Energy(eV)	Oscillator Strength	Nature of Transitions
S0→S1 (C_1)	3.22 eV	0.1606	H-1→L (28%) c_a H→L+1 (62%) c_b
S0→S2 (C_2)	3.38 eV	3.8305	H-1→L (62%) c_a H→L+1 (28%) c_b
S0→S3 (E_1)	4.07 eV	0.1543	H-3→L (25%) e_a H-2→L+1 (63%) e_b
S0→S4 (E_2)	4.12 eV	0.0181	H-3→L (64%) e_a H-2→L+1 (26%) e_b
S0→S5	4.21 eV	0.0000	H→L (97%) CT
S0→S6	4.38 eV	0.0000	H-1→L+1 (95%) CT

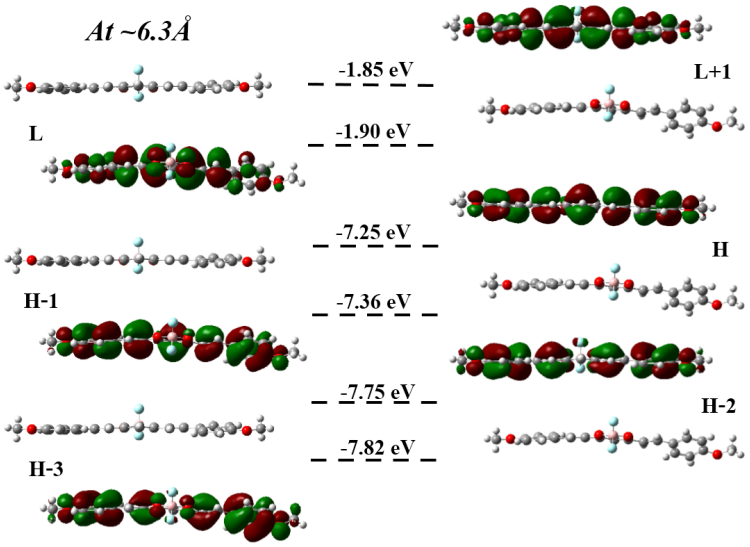

Figure A.7: FMO plots of TDDFT results for T-P curcumin dimer at distance 6.3 Å

5. T-P at 7.3 Å in Gasphase

Table A.8: TDDFT Calculations for BFC T-P dimers at 7.3 Å

Transitions	Transition Energy(eV)	Oscillator Strength	Nature of Transitions
S0→S1 (C_1)	3.24 eV	0.2352	H-1→L (25%) c_a H→L+1 (66%) c_b
S0→S2 (C_2)	3.37 eV	3.7767	H-1→L (65%) c_a H→L+1 (25%) c_b
S0→S3 (E_1)	4.07 eV	0.1501	H-3→L (19%) e_a H-2→L+1 (70%) e_b
S0→S4 (E_2)	4.12 eV	0.0266	H-3→L (71%) e_a H-2→L+1 (19%) e_b
S0→S5	4.33 eV	0.0000	H→L (98%) CT
S0→S6	4.50 eV	0.0000	H-1→L+1 (96%) CT

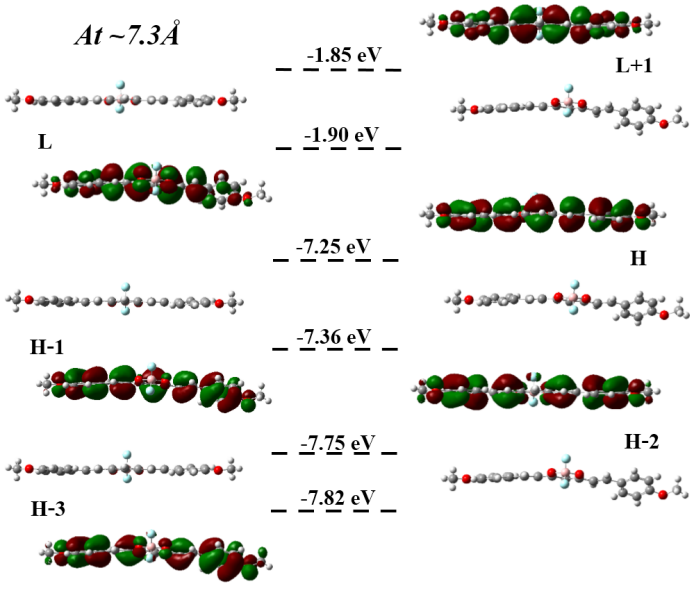

Figure A.8: FMO plots of TDDFT results for T-P curcumin dimer at distance 7.3 Å

6. T-P at 8.3 Å in Gasphase

Table A.9: TDDFT Calculations for BFC T-P dimers at 8.3 Å

Transitions	Transition Energy(eV)	Oscillator Strength	Nature of Transitions
S0→S1 (C_1)	3.25 eV	0.3276	H-1→L (21%) c_a H→L+1 (69%) c_b
S0→S2 (C_2)	3.36 eV	3.7032	H-1→L (69%) c_a H→L+1 (21%) c_b
S0→S3 (E_1)	4.08 eV	0.1422	H-3→L (13%) e_a H-2→L+1 (76%) e_b
S0→S4 (E_2)	4.11 eV	0.0374	H-3→L (76%) e_a H-2→L+1 (13%) e_b
S0→S5	4.43 eV	0.0000	H→L (98%) CT
S0→S6	4.59 eV	0.0417	H-1→L+1 (82%)

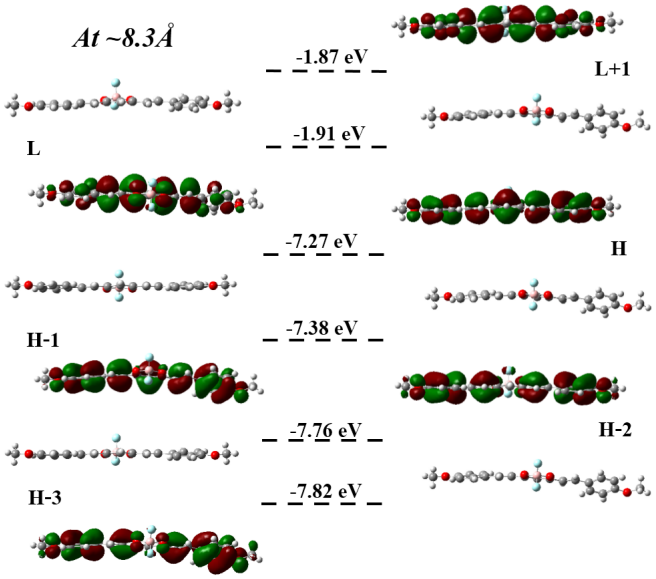

Figure A.9: FMO plots of TDDFT results for T-P curcumin dimer at distance 8.3 Å

List of Publications

Publications Related to the Thesis:

1. *Aggregates of quadrupolar dyes for two-photon absorption: the role of intermolecular interactions*
   Somananda Sanyal, Anna Painelli, Swapan K. Pati, Francesca Terenziani and Cristina Sissa,
   Phys. Chem. Chem. Phys., **18**, 28198 (2016).

2. *Addressing the manifold of charge-transfer and locally-excited states in biphenyl-based push-pull chromophore*
   Elisa Campioli, **Somananda Sanyal**, Mariangela Di Donato, Mireille Blanchard-Desce, Anna Painelli, Francesca Terenziani,
   (Manuscript under preparation).

3. *Superlinear amplification of the non-linear optical response of asymmetric dyes aligned inside carbon nanotubes*
   Somananda Sanyal, Cristina Sissa, Francesca Terenziani, Swapan K. Pati and Anna Painelli,
   (Manuscript under preparation).

Other Publications by Author:

4. *Effect of Imide Functionalization on the Electronic, Optical, and Charge Transport Properties of Coronene: A Theoretical Study*

Somananda Sanyal, Arun K. Manna and Swapan K. Pati,
J. Phys. Chem. C, **117**, 825 (2013).

5. *BN-decorated graphene nanoflakes with tunable opto-electronic and charge transport properties*
Somananda Sanyal, Arun K. Manna and Swapan K. Pati,
J. Mater. Chem. C, **2**, 2918 (2014).

6. *Functional corannulene: diverse structures, enhanced charge transport, and tunable optoelectronic properties*
Somananda Sanyal, Arun K. Manna and Swapan K. Pati,
ChemPhysChem, **15**, 885 (2014).